UC Berkeley

UC Berkeley Electronic Theses and Dissertations

Title

Atomistic Simulations of Screw Dislocations in Titanium

Permalink

https://escholarship.org/uc/item/15z3j8k8

Author

Poschmann, Max Nicholas

Publication Date

2018

Peer reviewed|Thesis/dissertation

Atomistic Simulations of Screw Dislocations in Titanium

by

Max Nicholas Poschmann

A dissertation submitted in partial satisfaction of the
requirements for the degree of
Doctor of Philosophy

in

Engineering - Materials Science and Engineering

in the

Graduate Division
of the
University of California, Berkeley.

Committee in charge:
Professor Daryl C. Chrzan, Co-Chair
Professor Mark Asta, Co-Chair
Professor Kristin Persson
Professor Peter Hosemann

Summer 2018

Atomistic Simulations of Screw Dislocations in Titanium

Abstract

Atomistic Simulations of Screw Dislocations in Titanium

by

Max Nicholas Poschmann

Doctor of Philosophy in Engineering – Materials Science and Engineering

University of California, Berkeley

Professor Daryl C. Chrzan, Co-Chair

Professor Mark Asta, Co-Chair

This dissertation contains a variety of atomistic calculations concerning screw dislocations in pure or nearly-pure titanium alloys. Many aspects of these dislocations are considered. First, the core structures of $\langle a \rangle$-type screw dislocations in pure titanium at zero temperature and no applied stress are calculated. The parameters required to converge calculations of the cores structures are identified. The energy differences between core structures were found to be small, which suggests that at practical temperatures there will be occupation of more than one core structure configuration. Next, the effects of applied stresses with zero resolved shear stress on these dislocations are considered. The results suggest that non-Schmid stresses alter the critical resolved shear stress by inducing changes in the equilibrium core structure. This corroborates earlier conjecture that the non-Schmid slip behavior of screw dislocations in α-titanium alloys is due to non-planar core structure. Chapter 5 describes a new parameter based on elasticity theory for dislocation core identification and classification. This parameter is applied to the study of dislocation core structures in an empirical potential, examining the dependence of the core orientation on temperature and applied non-Schmid stresses. It is found that increasing the temperature leads to a larger variation in the core orientations. It is also found that applied stress on the $[1\bar{1}00]$ axis normal to the dislocation line direction leads to a transition from the prismatic core structure to the pyramidal core structure. This transition appears to shift to lower pressure at higher temperature, suggesting that entropy of the core structures is important. It is demonstrated that temperature/non-Schmid stress conditions that permit easier access to the prismatic core orientation lead to higher strain rates for the same applied shear stress. In Chapter 6 I introduce a novel interstitial shuffling mechanism to explain how dilute concentrations of interstitial impurities can promote increased planarity of dislocation slip. This invites design of titanium alloys with increased tolerance to variations in interstitial impurity content. Finally, in Chapter 7 nucleation of the β to α phase transition in pure titanium is examined through a combination of elasticity theory and molecular dynamics simulation. Screw dislocations in the β phase act as heterogeneous nucleation sites and increase the α phase growth rate, but also restrict the orientation of the α nuclei to certain directions along which the strain field of the dislocation aligns with the strain required to complete the Burgers transformation path.

I have learned two ways to tie my shoes.
One way is only good for lying down.
The other way is good for walking.

<div style="text-align: right">

Valentine Michael Smith
Stranger in a Strange Land
Robert A. Heinlein

</div>

Contents

Acknowledgements

Chapter 1:

Introduction

I recently read – in the introductory paragraph of a popular science news article now lost to the depths of the internet – a statement to the effect of "materials scientists live in fear of defects." While there are many engineers and technicians who hope not to find unexpected defects in their products, generalizing this statement to all materials scientists in all circumstances is simply not correct. My experience with materials science has been one of seeking defects, not avoiding them. Whether it is myself or one of my computational coworkers carefully introducing vacancies, dislocations or twin boundaries into an atomistic supercell, a microscopist scanning their sample for dislocation slip traces, or a nuclear engineer irradiating their sample until it is riddled with voids, the science of materials revolves around identifying defects and studying their behavior. We do this because defects are where the engineering opportunities are to be found. They give us leverage over material behavior, allowing us to significantly change properties such as strength, toughness, conductivity, and photoluminescence by making small changes to the composition or processing of the material.

Defects also have surprising depth, which is another reason that materials scientists spend so much time pursuing and studying them. In this dissertation I will focus on one class of methods – atomistic simulations – to study one type of defect – screw dislocations – in one class of alloys – pure and commercially-pure titanium. This work uses the techniques of density functional theory and the modified embedded atom method, considers the role of the dislocation core structure and how they are influenced by stress and temperature, examines the interactions between screw dislocations and interstitial solutes (of which oxygen is the most important), and studies the effect of screw dislocations in high-temperature β-titanium in selecting the orientations of α-titanium grains that form during cooling. Still, this does not exhaust the potential of this one defect type in one alloy class to surprise us and to present new engineering possibilities.

1.1 Atomistic Simulations...

Atomistic simulations are the broad class of simulations in which the basic building block of the system being simulated is the atom. In continuum simulations, on the other hand, the system is assumed to be homogeneous throughout space and to reflect some bulk material properties. Finite element method simulations hold a middle ground, with space subdivided into regions large enough to contain many atoms, within each of which the material properties are assumed to be constant. While these more coarse-grained simulation methods offer clear advantages in terms of speed and scale, atomistic simulations are capable of much greater precision and allow us to study the structure and behavior of defects on their true length

scale. In this sense, atomistic simulations are much more physically satisfying than the competing methods. Since the Nobel Prize-winning work of Jean Baptiste Perrin more than a centuray ago, there has been no doubt of the theory that matter is composed of atoms. Thus it follows that to precisely model how materials deform one ought to consider the displacement of individual atoms.

This statement leads to an important question: what *is* the displacement of an individual atom, and how can one simulate it? To implement atomistic simulations, rules that define (1) the energy of the system and the forces that atoms will be subject to, and (2) how these will cause the atoms to move. And these rules have to be defined in terms of the information that is available in an atomistic simulation: what species of atoms there are, and where they are. Many forms of both types of rules exist. For type (1), of greatest importance to this dissertation are Density Functional Theory (DFT) and a simplification derived from DFT, the Embedded Atom Method (EAM). Both of these will be discussed in more detail later in the text, but can generally be summarized by the second Hohenburg-Kohn theorem[1]: the energy of a system is entirely determined by the electron density, and finding the minimum in energy with respect to variation in the electron density thus yields the ground state of the system. Therefore in performing atomistic simulations, one is to a large extent interested in electrons and the laws of quantum mechanics that govern their behavior.

The set of rules of type (2) also includes numerous options, including all the flavors of optimization that can be applied to find the equilibrium state of a system (for example Steepest Descent (SD), Conjugate Gradient (CG), and the various modern inertial optimization algorithms such as quick-min[2] and FIRE[3]), as well as time-evolution methods such as Molecular Dynamics (MD). Again, these methods will be discussed in more detail later. For the moment, I would like to reiterate the distinction between the types of rules (1) and (2) for atomistic simulations, as they are all-too-often conflated with one another. Type (1) determines how the energies and forces are calculated, i.e. through DFT, or by EAM, or by some pair potential. Type (2) determines what is done with those energies and forces, i.e. are they fed into a CG algorithm, or used to integrate the equations of motion in MD. One is not restricted in pairing between these types (though some pairs might be better suited to one another), for example CG optimization may be performed on energies and forces arising from DFT or from EAM, and MD can be integrated using forces generated by EAM or by DFT (this case is often called *ab initio*-MD, and is not employed here).

1.2 ...of Screw Dislocations...

Since Griffith[4] showed that the energy required to break a plane of perfect interatomic bonds in a perfect crystal is far greater than that needed to plastically deform a material it has been known that plasticity is carried by defects. These defects contain broken bonds, and in propagation through material produce strain by moving these broken bonds from one region to another. While there are numerous defects that can propagate plastic strain – for example twin boundaries that often dominate metals deformed at high strain-rates at low temperatures, or grain boundaries that slide past one another at very high temperatures – the most common and relevant in metals at normal working temperatures are dislocations. Dislocations are line defects that can be defined (at least in a local sense) by two quantities:

their Burgers vector[5] (which defines the magnitude and direction of plastic strain carried by the dislocation), and their line direction (which is simply along which vector the dislocation is oriented). Dislocations are typically grouped into three categories: edge, screw, and mixed. Edge dislocations have their Burgers vector perpendicular to their line direction, and thus represent the termination of a plane of atoms within the crystal. Screw dislocations (those of greatest interest in this dissertation) have parallel Burgers and line vectors, and can be best pictured by considering the threads on a screw or the ramp of a parking garage: if one completes a revolution about the screw axis, one has increased (or decreased) their altitude by a Burgers vector. The mixed type captures all other options, as their Burgers vectors lie somewhere between perpendicular and parallel to the line direction.

In the above description, I called dislocations "line defects". However, this is not an entirely accurate or helpful picture. In fact, considering that atoms occupy some volume in space a purely one-dimensional description is impossible. The defect *is* the disturbance of the position of atoms, and therefore it also must occupy some volume. The atoms that are part of this volume are in the dislocation core. Possible definitions of this core region are discussed in later chapters of this dissertation. For now, it is enough to say that the importance of dislocation core structure in controlling dislocation motion is well known in bcc[6], fcc[7], and hcp[8–11] metals. Because the core structure of dislocations is closely related to their dynamics[12], gaining a better understanding of these cores through atomistic modeling is of significant value to predicting the mechanical properties of alloys.

Dislocation core spreading and the resulting effects on slip were first introduced by Peierls[13] and expanded on by Nabarro[14]. According to their model, for a given burgers vector, line direction, and material there is a plane in which the dislocation will spread and have a minimal barrier to slip. For a dislocation with edge character this plane will always be the plane that contains both the burgers vector and line direction, but for a pure screw dislocation these directions are parallel and thus there are many possible glide planes. As illustrated by Clouet et al.[10] the difference in energies of screw dislocation cores spread on different planes can be very small, and yet still have significant implications for plasticity. Cross slip involves large dislocation segments – magnifying these differences. Clearly then accurately predicting slip behavior requires sufficient precision to both find the ground state core configuration and the energetic difference between that configuration and other nearby configurations. Further, the effects of stress and temperature on the core structure, as well as the time evolution and correlation of core structures, are important but not well-understood for hcp metals. All of these topics are considered in this dissertation.

1.3 ...in Titanium

The class of high-purity hexagonal close packed (hcp) titanium alloys known as commercial purity (CP) titanium (ASTM grades 1-4) possess a number of desirable properties that have made them popular in aerospace applications such as airframe skin and components, as well as for naval applications. These desirable properties include high strength, low density, high melting point, formability, and excellent resistance to corrosion due to passivation by a surface oxide layer. Despite these many attractive properties and the abundance of titanium in the crust of the Earth (it is the 4th most common metal[15]) the uses of titanium are

limited by high costs. This puts titanium in an interesting position: it is both a commonly-used material with clear and established technological applications, and a material that is probably under-utilized and whose uses could be expanded if production costs are reduced.

Much of the expense of titanium production is wrapped up in processing of the ore to remove excess oxygen. Oxygen alters the mechanical properties of titanium alloys significantly and in ways that are not desirable for most applications. In the concentration range typical for CP-Ti alloys (approximately 0.1 to 0.4 wt% oxygen) increasing oxygen content increases yield strength and flow stress, but significantly decreases other desirable properties[16] such as ductility and particularly toughness. For this reason, one of the focuses of this work is on the interactions between oxygen interstitials and screw dislocations in titanium.

Beyond the good technological and economic reasons for working on titanium, it is also a scientifically stimulating subject. Hexagonal metals have a surprising amount of character, and behave significantly differently from each other. While crystallographically speaking the same dislocations and twins are possible in all hcp metals, the distribution of defects found varies widely from one to another. For example, the ordering of twin boundary energies differs from one hcp metal to the next[17]. Another example is the structure of dislocation cores: titanium, zirconium, and magnesium all display different ground state core structures for the same screw dislocation core. The lower symmetry of hcp metals and the variation of c/a ratios allows for a good deal of variety, and thus it becomes easy to immerse oneself in just one hexagonal metal.

1.4 Dissertation outline

In the next chapter I will describe the methods and concepts used that are common to multiple of the subsequent sections. Some of these (such as DFT, EAM, and MD) have already been briefly discussed, but much greater detail will be provided in Chapter 2. Other techniques that will be described include the Nudged Elastic Band (NEB) method.

In Chapter 3 the structure and properties of $\langle a \rangle$-type screw dislocation cores in pure titanium will be discussed. This begins with calculation of the ground state core structure and other nearby local minima at zero temperature and stress. Next, in Chapter 4 the effects of applied stress on the core structure will be investigated, and the role of these effects in observed non-Schmid-Law behavior examined.

Chapter 5 explores the time-evolution of dislocation core structures at temperatures in the range 100 K to 500 K and under a range of applied stresses. This section includes the development and implementation of a new method applicable to (but not limited to) rapidly and automatically determining dislocation core orientation, which allows for determination of the core structure for many thousands of sections of dislocation line. These calculations are used to present the first atomistic observations of the locking-unlocking mechanism based on the dislocation core structure for dislocations.

In Chapter 6 the interactions between $\langle a \rangle$-type screw dislocations and interstitial solutes (primarily oxygen, but with some additional comments on the next-most-important solutes nitrogen and carbon) are studied. This investigation leads to a new proposed slip-plane softening mechanism, which I refer to as the Interstitial Shuffling Mechanism (ISM). This mechanism provides a new explanation for the existence of planar slip in titanium alloys with

high oxygen but low aluminum concentrations, and knowledge of it provides a new potential pathway to designing tougher and less expensive titanium alloys.

In Chapter 7 a detour into high-temperature β (bcc) titanium is taken. The role of screw dislocations in the β phase in nucleating α titanium during cooling is examined, and it is shown that these dislocations are important nucleation sites as well as powerful selectors of which orientation variants of α titanium grow. This section also provides a good example of the importance of using long dislocation line segments in certain atomistic simulations, which is rarely done. It is also a good case for the recently-developed Polyhedral Template Matching[18] algorithm for phase identification, as the orientation-mapping abilities of PTM prove very useful.

Finally, this dissertation will wrap up in Chapter 8 with a brief summary followed by some thoughts on future work stemming from the presented ideas.

Chapter 2:

Methods

In this chapter I will outline the various methods that are used in the later chapters. In particular, methods that are used in multiple of the following chapters are the focus of the following sections, while certain methods used only once will be described in the relevant chapters. Here, the goal is to provide the context necessary to understand the calculations performed throughout this dissertation rather than a complete derivation or instruction manual for the following techniques.

2.1 Density Functional Theory

There is a sense in which all the mysteries of condensed-matter physics have been resolved for some time now. In the explosion of modern physics that occurred between Einstein's 1905 papers that introduced relativity[19] and quantum mechanics[20] and Feynman's 1949 work in unifying these ideas[21], the laws needed to understand physics on the atomic scale were discovered and written down. In theory, one can solve virtually all the practical problems of materials that one can think of. In practice, however, the situation is entirely different. The laws of quantum mechanics do not lend themselves to exact solutions for systems more complicated than a hydrogen atom, and the resources required to numerically compute the solutions to more complicated problems naively would be immense. Thus in the period following Feynman much of the work in condensed-matter physics has been focused on finding effective approximations that can be employed to simplify problems and methods to solve these problems efficiently. In this time, no development has been more significant than the invention of Density Functional Theory (DFT).

DFT got its start in the work of Hohenburg and Kohn in 1964[1], in which they provided the first two crucial building blocks for the theory. These are:

1. the potential energy of any system of interacting particles in an external potential is a unique functional of the ground-state particle density, and

2. it is possible to define a universal functional for the energy of the system of interacting particles in terms of the particle density, minimization of which would yield the ground-state energy and particle density.

These statements offer some tantalizing possibilities. For many material systems of interest it is reasonable to make use of the Born-Oppenheimer approximation[22] that the atomic nuclei are effectively stationary. This permits us to consider the entire system to be one of identical interacting particles (electrons) in an external potential that results from the Coulombic interactions of the electrons and nuclei. Therefore realization of the second theorem would

yield a method for calculating the ground-state energy and electron density of any atomic configuration one can design.

In 1965, Kohn and Sham[23] provided a method for realizing this possibility. Their groundbreaking *ansatz* was that the correct ground-state particle density of an interacting particle system of interest can be found exactly by considering an auxiliary system of non-interacting particles. Doing so relies on the unproven assumption that the non-interacting particle ground state density represents the ground-state density of the interacting many-particle system. Nonetheless, this was the crucial simplification required to make DFT calculations tractable. The Kohn-Sham energy functional is:

$$E_{Kohn-Sham}[n] = \int V_{ext}(\boldsymbol{r})n(\boldsymbol{r})d\boldsymbol{r} + \frac{1}{2}\int\int\frac{n(\boldsymbol{r})n(\boldsymbol{r}')}{|\boldsymbol{r}-\boldsymbol{r}'|}d\boldsymbol{r}d\boldsymbol{r}' + T_s[n] + E_{xc}[n] + E_{II} \quad (2.1)$$

where $V_{ext}(\boldsymbol{r})$ is the external potential, $n(\boldsymbol{r})$ is the non-interacting particle density, $T_s[n]$ is the kinetic energy of the non-interacting particles, $E_{xc}[n]$ is what is called the exchange-correlation functional, which in a sense absorbs all the physics of the interacting particle system that would otherwise be missing from the non-interacting system, and E_{II} is the energy of Coulombic interaction between the nuclei. The second term in this functional captures the Hartree energy, the Coulombic repulsion between non-interacting electrons.

Most of the terms in the Kohn-Sham functional are straightforward to compute, given an electron density. The one question mark in Equation 2.1 is the exchange-correlation functional $E_{xc}[n]$. This term represents the energy due to electron-electron interactions that is not captured by the Hartree energy, namely exchange and correlation energies. The exchange energy provides a negative contribution to the energy that arises from two sources: the Pauli exclusion principle, and correction of the self-interaction of electrons implicit in the Hartee term of the functional. The correlation energy is somewhat more nebulous. The definition varies from source to source, but roughly it includes all the correlations of many-electron systems not otherwise accounted for[24].

The functional derivative of $E_{xc}[n]$ is the exchange-correlation potential $V_{xc}(\boldsymbol{r})$[24]. This is a crucial point at which approximation enters into DFT. Getting the exchange and correlation of the system exactly correct would require returning to the many-particle system, so instead simplifications are used in place of this. The simplest of these approximations is based on the assumption that at any point the electron density can be represented locally as being equal to that of a homogeneous electron gas, and the (known) exchange and correlation of a homogeneous electron gas with the given density can be used in place of the exchange and correlation of the real system at that point. This form for $E_{xc}[n]$ is known as the Local Density Approximation (LDA) and was provided by Kohn and Sham[23] as the first exchange-correlation potential.

With an exchange-correlation potential in hand, one can define a Schrödinger-like equation for Kohn-Sham DFT[24]:

$$(-\frac{1}{2}\nabla^2 + V_{ext}(\boldsymbol{r}) + V_{Hartree}(\boldsymbol{r}) + V_{xc}(\boldsymbol{r}))\psi_i(\boldsymbol{r}) = \epsilon_i\psi_i(\boldsymbol{r}) \quad (2.2)$$

$V_{Hartree}$ is the potential corresponding to the Hartree term in Equation 2.1 (i.e. its functional derivative), $\psi_i(\boldsymbol{r})$ are the wavefunctions, and ϵ_i the Kohn-Sham equation eigenvalues.

While LDA proved surprisingly accurate for such a simple approximation, it has obvious shortcomings when the electron density varies rapidly. In their same paper, Kohn and Sham suggested the next step in of the approximation: include gradient terms in $E_{xc}[n]$. Approaches based on this suggestion are known as Generalized-Gradient Approximation (GGA) potentials. Unlike LDA, however, there is not a unique approach to GGA. Because of this, many different GGA potential forms exist. By far the most popular today (and the one used in all DFT work presented in this dissertation) is the method of Perdew, Burke, and Enzerhof[25] (known as PBE). In PBE, the various coefficients that arise when taking the gradient of the exchange-correlation functional are constructed by enforcing seven physical constraints, and thus all parameters for the gradients are fundamental constants. The lack of fitting parameters as well as the efficiency and accuracy of PBE has lead to it being one of the dominant forms for exchange-correlation in DFT over the last two decades.

Once an exchange-correlation functional form is chosen, the Kohn-Sham functional is complete. However, there remains room for further simplification before moving on. Consider the structure of an atom. In the center is the nucleus, which consists of neutrons and protons. Surrounding this are the tightly-bound core electrons, and further out are the valence electrons. In most of the common pictures of interatomic bonding, only the valence electrons play an important role. Therefore it seems reasonable to replace the nucleus plus all-electron picture of our atom with one that has an ionic core that includes some of the more tightly-bound electrons, plus the valence electrons. In doing so one can significantly reduce the degrees of freedom of the problem and thus greatly increase computational efficiency. Potentials that follow this ion-plus-valence-electrons model are known as pseudopotentials. Choosing a pseudopotential amounts to answering the question "how will I replace the ionic core with an effective potential?". But I will put that question on hold for a moment.

Next is the problem of how to actually solve for the ground-state electron density of a system of interest. This involves choosing a basis, which invites some consideration of the system of interest. In this work, all the systems considered are metals, and I am interested in bulk properties. Thus an obviously useful configuration is a periodic system, and a useful choice of basis set is plane waves. The choice of basis set and pseudopotential are closely connected, as choice of a useful pseudopotential for a given basis can greatly simplify electronic structure calculations[24].

Many pseudopotential types have been developed and are described at length in resources such as Martin's Electronic Structure textbook[24]. Here, I will describe only the Projector Augmented-Wave (PAW) method[26] which is employed in the calculations presented below. This is an efficient and robust method regarded as one of the standard pseudopotentials in DFT, though to be more accurate it is actually a simplified all-electron method rather than a proper pseudopotential method. The goal of this method is to achieve the accuracy of all-electron methods for all observables using pseudo-wavefunctions instead of all-electron wavefunctions. This is done by defining a transformation $\mathcal{T}$ that links the pseudo-wavefunction $|\tilde{\Psi}\rangle$ and all-electron wavefunction $|\Psi\rangle$:

$$|\Psi\rangle = \mathcal{T}|\tilde{\Psi}\rangle. \tag{2.3}$$

$|\tilde{\Psi}\rangle$ only differs from $|\Psi\rangle$ in a spherical region called the augmentation sphere about each atom. In this region, $|\tilde{\Psi}\rangle$ is expanded in terms of spherical Bessel functions. Outside of the

sphere, $|\tilde{\Psi}\rangle$ consists of the same plane waves as $|\Psi\rangle$. In typical PAW implementations the electronic states that are inside the augmentation sphere are considered to be frozen and are not relaxed during calculation. By eliminating these degrees of freedom computational efficiency can be greatly improved. However, as described in Chapter 3, it is important to check which states can be considered to be frozen.

Having chosen a basis set, the remaining task is to integrate Equation 2.1 over it and minimize. It appears that this requires integration over all space, but thanks to Bloch's theorem it is only necessary to integrate over a primitive cell in reciprocal space (the Brillouin zone). In practice, a sum of samples taken at special points is used in place of integration (k-point sampling), with the set of special points selected referred to as the k-point mesh. At each of these points a sum over the chosen plane wave basis functions is performed, up to a chosen cutoff wavevector magnitude (often specified in terms of energy). Typically these points are chosen to be an evenly-spaced grid in reciprocal space, which can then be reduced to a smaller set of points (the irreducible wedge) by using the symmetry operations of the system of interest to determine which points are redundant. In most of the calculations presented in this dissertation the k-point meshes are of the Monkhorst-Pack[27] form, centered on the Γ-point because most of the lattices are hcp. One interesting note on k-point sampling is that the k-point mesh density is one parameter with respect to which the DFT energy is not variational. In other words, increasing the k-point mesh density (increasing calculation accuracy) does not always decrease the computed energy of the system. Adding more k-points does not increase the degrees of freedom of the system, just the level of detail of bookkeeping (and thus the accuracy of the approximation to the real system).

Unfortunately, for DFT calculations of metals integration is not quite that simple. Metallic bonding is defined by partially-filled valence bands, which leads to discontinuities in the functions being integrated. For example, consider the total charge of the system I:

$$I = \int_{Brillouin\ Zone} S(E(\boldsymbol{k}) - E_f)g(\boldsymbol{k})d\boldsymbol{k} \tag{2.4}$$

where E_f is the Fermi energy, $E\boldsymbol{k})$ is the energy of the band as a function of $\boldsymbol{k}$, $g(\boldsymbol{k})$ is the density of states, and S is a step function defined as $S(x) = 1 - \Theta(x)$ with $\Theta(x)$ a Heaviside step function. Clearly the discontinuity of $S(E(\boldsymbol{k}) - E_f)$ will make this function very difficult to integrate, and inaccurate if naively summed over some finite set of points. This is especially problematic for calculations of forces (which naturally require differentiation). In this work, this problem is alleviated by employing the method of Methfessel and Paxton[28]. In this method, S is replaced by a smooth function that can be used to integrate accurately. In particular, they use

$$
\begin{aligned}
S_0(x) &= \frac{1}{2}(1 - erf(x)) \\
S_N(x) &= S_0(x) + \sum_{n=1}^{N} A_n H_{2n-1}(x)e^{-x^2}
\end{aligned}
\tag{2.5}
$$

where $H_n(x)$ is the Hermite polynomial of degree n, and A_n are coefficients given in their paper. To use this method in conjunction with a k-point sampling method, they provide the

definition of x in Equation 2.5 as the list of points x_i that correspond to the k-point mesh points $\boldsymbol{k}_i$:

$$x_i = \frac{E(\boldsymbol{k}_i) - E_f}{W}, \tag{2.6}$$

with W this smearing or broadening parameter. This parameter adds an effective electronic temperature to the system, and is proportional to the amount of smoothing of the function S. To put it another way, for smaller W the system approaches the un-smoothed one, and thus greater integration difficulty from discontinuities arises and more k-points are required. For larger W the effects of smoothing are greater, and electronic entropy influences the calculated energy of the system to a greater degree, which reduces accuracy. In the DFT metals community, the usual compromise is to choose the greatest value for W that results in an electronic entropy contribution to the total energy of less than 1 meV per atom in the system. This is done in this work.

The above summarizes the components required to compute the energy of a system of interest using DFT. However, for the purposes of this work I wish to go a step further and actually optimize the structure of the system as well. This requires computation of forces (as alluded to above) as well as stress to guide rearrangement of ions in the system. To calculate the forces on the ions, the theorem attributed to Hellmann and Feynman but in fact documented by numerous authors[29–32] is employed. This theorem results from perturbation theory applied to the derivative of the energy with respect to the positions of each ion in the system, and some helpful cancellation results in:

$$F_i = -\int n(\boldsymbol{r}) \frac{\partial v(\boldsymbol{r})}{\partial \boldsymbol{R}_i} d^3\boldsymbol{r} - \frac{\partial E_{II}}{\partial \boldsymbol{R}_i} \tag{2.7}$$

where F_i is the force on ion i at position $\boldsymbol{R}_i$.

To compute stresses and thereby relax the shape of atomic configurations in DFT, the generalized virial theorem of Nielsen and Martin[33, 34] is used.

I am quite thankful that it was not necessary to implement software to invoke all of the above. Instead, the DFT calculations presented in this dissertation were computed using the Vienna *Ab initio* Simulation Package (VASP)[35, 36]. This robust, efficient, and well-documented software package enabled me to take advantage of modern supercomputing resources to perform many relatively large-scale DFT calculations (including up to some hundreds of atoms). The workflow to complete a DFT calculation including structural relaxation, from my perspective, is as follows:

1. construct the atomistic representation of the system of interest,

2. select the level of exchange correlation potential appropriate for the system and the desired results (here, the PBE form of GGA),

3. select the form of pseudopotential (here, PAW),

4. choose which electronic states will be considered to be (frozen) core states,

5. set the size of the planewave basis set to be used,

6. set the k-point mesh density and geometry desired,

7. select a smearing parameter and order,

8. choose tolerances for energy and force convergence.

Given all this input from the user (me), the workflow from VASP's perspective is:

1. guess an initial electron density function $n(\boldsymbol{r})$ and calculate the corresponding energy using Equation 2.1,

2. calculate $v(\boldsymbol{r})$ corresponding to $n(\boldsymbol{r})$,

3. calculate the (pseudo) wavefunctions that solve Equation 2.2 for $v(\boldsymbol{r})$,

4. determine a new $n(\boldsymbol{r})$ corresponding to the wavefunctions and calculate the corresponding energy using Equation 2.1,

5. if the change in energy is smaller than the selected tolerance, calculate forces and stress; if larger, return to 2,

6. if forces and stress are smaller than the selected tolerance, terminate calculation; if not, adjust lattice vectors and ionic coordinates then return to 2.

In this way, all the complexity of the preceding section is effectively replaced by carefully choosing a set of parameters. Of course, these choices must be made in the light of understanding of the significance of each to the calculation at hand as well as the interplay between them. In practice, these choices are checked and re-checked to ensure the convergence and also the significance of the calculation results.

2.2 Embedded Atom Method

While DFT was a massive step forward in terms of what systems one could calculate the structure and energy of, the $\mathcal{O}(n^3)$ or $\mathcal{O}(n^2 log(n))$ computational intensity vs number of electrons (n) scaling of most DFT implementations (including VASP) makes performing DFT calculations of systems with more than some hundreds of atoms impractical. In this dissertation the largest DFT calculations involve 577 atoms. For many of the systems of interest here, that is simply not enough atoms to accomplish our research goals. Therefore in many of the following chapters a higher level of approximation that provides access to larger system sizes and faster computation is applied, and that is the Embedded Atom Method (EAM).

EAM has its roots in a corollary of DFT, known as the quasiatom. The concept of a quasiatom (introduced by two professors from my undergraduate department at Queen's University, Malcolm Stott and Eugene Zaremba) is that if an atom is added to an electronic host system, the energy of that addition is a functional of the electron density of the unperturbed host system[37]. This concept was expanded upon by Daw and Baskes, who showed

that this idea could be applied to all atoms in a system, with each being embedded into the system containing all the others[38, 39]. This transforms the quasiatom concept:

$$E_{quasiatom} = E_z(\rho_h(\boldsymbol{R})) \tag{2.8}$$

with z the atomic number, ρ_h the host electron density and $\boldsymbol{R}$ the embedding position, to a method for calculating the energy of the entire system, along the lines of:

$$E_{EAM} = \sum_i E_{z_i}(\rho_{h,i}(\boldsymbol{R}_i)) + \frac{1}{2} \sum_{\substack{i,j \\ i \neq j}} \phi_{ij}(R_{ij}). \tag{2.9}$$

Here, the first sum runs over all atoms i in the system, and $\rho_{h,i}(\boldsymbol{R}_i)$ is the host electron density at the position of the ith atom ($\boldsymbol{R}_i$), if the ith atom is omitted. The second sum is over atom pairs, with $\phi_{ij}(R_{ij})$ representing the Coulombic repulsion between cores separated by distance R_{ij}.

On the face of it, this doesn't make the problem any simpler. To calculate the energy exactly, one would have to find all $\rho_{h,i}(\boldsymbol{R}_i)$, which actually seems like more work than the DFT problem was. However, what it provides is a useful framework for developing empirical potentials in which $\rho_{h,i}(\boldsymbol{R}_i)$ is taken to be the sum of fixed density functions about each atom center (which are assumed to be zero beyond a certain cutoff radius, usually a few times the nearest-neighbor distance in the system), and the embedding energy as a function of density is fit to experimental and/or calculated data. Empirical potentials of this form are commonly referred to as EAM potentials.

By considering the electron density to simply be a sum of fixed densities the amount of computation required is greatly reduced. Compared to DFT, this effectively skips the electronic structure part of the optimization (often referred to as the "inner loop") and goes directly to energy and force evaluations. Further, not worrying about interacting electrons and considering only short-range interactions improves the computational scaling to $\mathcal{O}(n)$. However, empirical potentials (including EAM) are naturally less flexible than *ab initio* techniques (such as DFT), because calculations are only valid when the atomic configurations are similar to those which the potential was fit to represent. Configurations that would induce large changes in the electron density (such as placing two atoms very near each other) do not yield meaningful results in EAM (nor in fact in frozen-core DFT with core radii set too large). Of course, properties that can derived from the ground-state electron density in DFT such as specific heat or susceptibility are not available from EAM, since the electron density is not realistic, and typically is not explicitly calculated at all.

On the other hand, EAM was a major improvement in accuracy over (but is also more computationally expensive than) its predecessor empirical methods such as pair potentials. By approximately including effects of changes to the electron density around an atom EAM is able to reproduce energies of surfaces, cracks, and vacancies in metallic systems that pair potentials could not. In EAM, the presence of an atom affects the way that nearby atoms bond to each other through its contribution to the electron density. This matches the common understanding of metallic bonding, but is the sort of behavior that is absent when only pairwise interactions are considered.

The most commonly-used empirical potential in this dissertation is in fact not of the original EAM form, but a more recent form developed by Baskes, Nelson, and Wright known as the Modified Embedded Atom Method (MEAM)[40, 41]. This method builds on EAM chiefly by including 3-body interaction terms, and thus capturing some of the angular dependence of atomic bonding.

Calculations involving empirical potentials are implemented in the Large-scale Atomic/Molecular Massively Parallel Simulator (LAMMPS) software package[42]. This is an open-source package that has many forms for empirical potentials implemented, as well as optimization methods, MD with a rich variety of options, NEB, and more.

2.3 Optimization

The above sections cover the two choices for rules of type (1) employed in this dissertation, as introduced in Chapter 1. These rules determine how the energies, forces, and stresses on atomic configurations are calculated in atomistic simulations. In this section and the following, options for rules of type (2) – how to evolve the structure given energy and forces – are described. This section in particular describes how this is done in simulations that do not consider time or temperature. Optimization methods are used simply to find the lowest-energy configuration. The degree to which this tends to be a global or local minimum depends on both the method used and the potential energy landscape of the system of interest.

Perhaps the most obvious way to optimize a system is called Steepest Descent (SD). At each step of SD, the gradient of the energy in configuration space is determined from the calculated forces, and the system moved in the direction of the gradient by an amount scaled to magnitude of the forces. If this process is repeated sufficiently, eventually the system reaches the force tolerance at the bottom of the nearest local minimum of the potential energy.

While the merit of SD is clear, in practice it can be very inefficient for finding minima. Often it takes many steps along the same direction, for example in optimizing a 2-dimensional parabolic function it may simply alternate between two orthogonal directions over and over and take many steps to converge for even this simple problem[43]. To avoid this re-use of directions and in general improve the rate of convergence, one can make use of information from previous steps in the optimization to improve the next step. One method of doing this is to take each step along a direction that is perpendicular to all previous search directions. If those directions are generated from gradients, then this corresponds to the method of conjugate gradients (CG). This method is described in detail in the excellent (and excellently-named) work "An Introduction to the Conjugate Gradient Method Without the Agonizing Pain"[43]. In brief, the first step taken is the same as in SD. For all following steps, the gradient is calculated but then orthogonalized (following a Gram-Schmidt process) with all previous gradients before the next step is taken.

Another way to take into account previous steps is to use an "inertial" term in the optimization, as is done in the FIRE[3] algorithm for example. As a brief summary, this algorithm directs that if the current force and the most recent direction of optimization are well-aligned, then the optimization should be accelerated in this direction. When they are

not, the added "inertia" is canceled. This method in particular is mentioned because it is used in this work in conjunction with the nudged elastic band method in some cases, as will be described below.

It is worth noting also that optimization is important to the creation and core functioning of methods such as DFT and EAM. For example, in the inner loop of a DFT calculation the electron wavefunctions are being optimized to yield the lowest energy for the current ionic coordinates. In VASP, this is done with a CG-like algorithm. For empirical potentials, the fitting process typically involves a good deal of optimization.

2.4 Molecular Dynamics

When interested in the time-dependent evolution of a system at finite temperature, rather than advancing down an energy gradient what one must do is integrate equations of motion. For practical temperatures (well above the Debye temperature) and most atomic species (those heavy enough to neglect tunneling effects), it is appropriate to employ the classical equations of motion, as the behavior of the ions will not display any appreciable amount of quantum behavior. Therefore the relevant equations are those due to Hamilton:

$$
\begin{aligned}
\frac{d\boldsymbol{p}_i}{dt} &= -\frac{\partial \mathcal{H}}{\partial \boldsymbol{r}_i} \\
\frac{d\boldsymbol{r}_i}{dt} &= +\frac{\partial \mathcal{H}}{\partial \boldsymbol{p}_i}
\end{aligned}
\tag{2.10}
$$

where $\boldsymbol{r}_i$ are the atomic coordinates, $\boldsymbol{p}_i$ the momenta of the atoms, and $\mathcal{H}$ the Hamiltonian of the system:

$$
\mathcal{H}(\boldsymbol{r}, \boldsymbol{p}) = \sum_i \frac{\boldsymbol{p}_i^2}{2m_i} + V(\boldsymbol{r}),
\tag{2.11}
$$

with m_i the mass of the ith atom, and $V(\boldsymbol{r})$ the potential energy of the system. $V(\boldsymbol{r})$ (as well as a function for calculating forces $\boldsymbol{F}_i(\boldsymbol{r})$) is the part supplied from a method such as DFT or EAM, so in general can be a very complicated function. Further, typical MD simulations contain thousands to millions of atoms. These factors make it impossible to deliver an analytical solution for the time evolution of the system, and instead this is determined numerically using a timestepping algorithm.

One of the earliest and most popular MD algorithms (known as integrators) – and the only one used here – is the velocity Verlet algorithm[44]. To make use of the algorithm, first one chooses a timestep (Δt). In typical atomistic simulations this is 1 fs. Then, assuming that at time t the positions and momenta of all particles in the system are known (they may begin from rest, or one might supply an initial randomized velocity distribution to induce a desired temperature for the system), the algorithm proceeds as follows to $t + \Delta t$[45]:

$$
\begin{aligned}
\boldsymbol{p}_i(t + \frac{\Delta t}{2}) &= \boldsymbol{p}_i(t) + \frac{\Delta t}{2m_i}\boldsymbol{F}_i(\boldsymbol{r}(t)) \\
\boldsymbol{r}_i(t + \Delta t) &= \boldsymbol{r}_i(t) + \Delta t \boldsymbol{p}_i(t + \frac{\Delta t}{2}) \\
\boldsymbol{p}_i(t + \Delta t) &= \boldsymbol{p}_i(t + \frac{\Delta t}{2}) + \frac{\Delta t}{2m_i}\boldsymbol{F}_i(\boldsymbol{r}(t + \Delta t))
\end{aligned}
\tag{2.12}
$$

and so on for following steps.

The velocity Verlet algorithm is useful because it obeys the basic rules for classical simulations: it is time-reversible[45], and in the limit of infinitesimal timesteps conserves the energy of the system.

While this last point is certainly a good feature, often one does not desire to perfectly conserve the total energy of a system. The physical system of interest does not exist in a vacuum, and in fact will be in contact with media with which it can exchange energy and volume. Therefore in atomistic simulations the goal is often to maintain a selected temperature and stress state. The tools which permit us to achieve these goals are known as thermostats and barostats.

The thermostat used in this work is called the Langevin thermostat, and functions by modifying the force on each atom during the MD simulation by adding a random force and a damping term. To put it another way, the force experienced by an atom when a Langevin thermostat is employed is $\boldsymbol{F}_i^{Langevin}$[46]:

$$\boldsymbol{F}_i^{Langevin} = \boldsymbol{F}_i - \gamma_i \frac{\boldsymbol{p}_i}{m_i} + \boldsymbol{F}_i^R(t) \tag{2.13}$$

where γ_i is the damping coefficient and $\boldsymbol{F}_i^R(t)$ is the random force. $\boldsymbol{F}_i^R(t)$ is a Gaussian process with the following properties[46]:

$$\langle \boldsymbol{F}_i^R(t) \rangle = \boldsymbol{0}$$
$$\langle \boldsymbol{F}_i^R(t) \boldsymbol{F}_i^R(t')^\intercal \rangle = 2\gamma_i k_B T m_i \delta(t - t') \tag{2.14}$$

where k_B is the Boltzmann constant, T is the target temperature, $\delta(t)$ is a Dirac delta function, and $\langle x \rangle$ indicates the expectation value of x. The dispersion of the Gaussian is chosen to be σ_i:

$$\sigma_i^2 = \frac{2m_i \gamma_i k_B T}{\delta t}. \tag{2.15}$$

In this way, the Langevin thermostat approximates a heat bath by adding energy to the particles according to a random distribution corresponding to the desired temperature, but also removing velocity (and thus kinetic energy) through the damping term to ensure the system does not become over-heated.

Similarly to how a thermostat can be used to hold the system at a desired temperature, a barostat can be employed to apply a desired stress to the system. Examples of target stresses include setting all stress components to zero (i.e. allowing the system to relax at low pressure), or setting one component to some large value and the rest to zero, as might be the case in a uniaxial tensile test. As with the thermostat, applying a barostat alters the equations of motion to be integrated in MD. When a barostat is used in this dissertation, it is that due to Parrinello and Rahman[47]. This barostat is a particularly useful extension of the earlier formulation of Hoover *et al.*[48], which adds the capacity to set each stress component independently.

The role of the barostat is to adjust the vectors that define the dimensions of the periodic simulation cell ($\boldsymbol{h}$) such that the target stress ($\boldsymbol{\sigma}_{target}$) is reached. The positions of the atoms

in the cell are then scaled to the new lattice vectors. This, of course, requires that one knows the stress in the system at the current time ($\boldsymbol{\sigma}_{actual}$). This is found using a virial theorem:

$$\Omega\boldsymbol{\sigma}_{actual} = \sum_i \frac{\boldsymbol{p}_i\boldsymbol{p}_i}{m_i} - \sum_i \sum_{j>i} \frac{F_{ij}}{r_{ij}}\boldsymbol{r}_{ij}\boldsymbol{r}_{ij} \tag{2.16}$$

where Ω is the volume of the cell (i.e. $||\boldsymbol{h}||$), F_{ij} is the magnitude of the force acting between atoms i and j (a formalism for extracting useful approximations for these from EAM and MEAM type potentials exists for this purpose), $\boldsymbol{r}_{ij}$ is the vector connecting these atoms, and r_{ij} its magnitude.

$\boldsymbol{\sigma}_{target}$ is converted to a symmetric form $\boldsymbol{\Sigma}$:

$$\boldsymbol{\Sigma} = \boldsymbol{h}^{-1}(\boldsymbol{\sigma}_{target} - \frac{Tr(\boldsymbol{\sigma}_{target})}{3})\boldsymbol{h}^{-\intercal}\Omega \tag{2.17}$$

And this is used to evolve the cell vectors:

$$W\frac{d^2\boldsymbol{h}}{dt^2} = (\boldsymbol{\sigma}_{actual} - \frac{Tr(\boldsymbol{\sigma}_{actual})}{3})\boldsymbol{h}^{-\intercal}\Omega - \boldsymbol{h}\boldsymbol{\Sigma}. \tag{2.18}$$

Here, W is a relaxation time for the stress, and enters MD simulations as a parameter chosen by the user. Anderson suggests[49] and Parrinello and Rahman reiterate[47] that a good choice for W is on the order of the length of the cell divided by the speed of sound in the system.

2.5 Nudged Elastic Band Method

A key technique in this work is the nudged elastic band (NEB) method[50]. NEB is a method for computing energy barriers for transitions between local minima in phase space. Often the energy barriers of interest are large, and thus the transition is unlikely to occur within the timescale of an MD simulation. Thus, it must be forced to happen for the energy barrier to be computed. This is done by constructing an "elastic band" consisting of $N+1$ images $\boldsymbol{Q}_0$ through $\boldsymbol{Q}_N$, each a replica of the entire atomistic system. $\boldsymbol{Q}_0$ and $\boldsymbol{Q}_N$ are the endpoint images, and thus are the states of the system in the local minima of interest. The images $\boldsymbol{Q}_1$ through $\boldsymbol{Q}_{N-1}$ lie between them in phase space, in order. A common practice is to use linear interpolation of the positions of all atoms to form the initial guess for the intermediate images. In relaxing the system, all images simultaneously relax while each image is considered to be attached to its neighbors by "springs".

To accomplish this, first find the tangent ($\hat{\boldsymbol{\tau}}$) in phase space at each image[51]:

$$\begin{aligned}\boldsymbol{\tau}_i &= \frac{\boldsymbol{Q}_i - \boldsymbol{Q}_{i-1}}{|\boldsymbol{Q}_i - \boldsymbol{Q}_{i-1}|} + \frac{\boldsymbol{Q}_{i+1} - \boldsymbol{Q}_i}{|\boldsymbol{Q}_{i+1} - \boldsymbol{Q}_i|}\\ \hat{\boldsymbol{\tau}}_i &= \frac{\boldsymbol{\tau}_i}{|\boldsymbol{\tau}_i|}.\end{aligned} \tag{2.19}$$

The component of the potential energy gradient in phase space ($\boldsymbol{\nabla}V$) that is perpendicular to $\hat{\boldsymbol{\tau}}$ is then calculated:

$$\boldsymbol{\nabla}V(\boldsymbol{Q}_i)|_\perp = \boldsymbol{\nabla}V(\boldsymbol{Q}_i) - \boldsymbol{\nabla}V(\boldsymbol{Q}_i)\cdot\hat{\boldsymbol{\tau}}_i \tag{2.20}$$

and the force due to the springs (given spring constant k) also found:

$$\boldsymbol{F}_i^s|_\| = k((\boldsymbol{Q}_{i+1} - \boldsymbol{Q}_i) - (\boldsymbol{Q}_i - \boldsymbol{Q}_{i-1})) \cdot \hat{\boldsymbol{\tau}_i}. \tag{2.21}$$

Equations 2.20 and 2.21 are summed to yield the force added to each image F_i^{NEB}:

$$\boldsymbol{F}_i^{NEB} = \boldsymbol{F}_i^s|_\| - \boldsymbol{\nabla}V(\boldsymbol{Q}_i)|_\perp. \tag{2.22}$$

The situation then is akin to two valleys separated by mountains. The elastic band is stretched over the mountain tops, and allowed to relax with the hope that it will locate the lowest mountain pass that connects the valleys. The "altitude" of this pass is actually the energy barrier to completing the transition between the two states of interest, which can be used to estimate the transition rate. The performance of this method can be improved by using what is known as the Climbing Image NEB (CI-NEB) method, in which the sign of the second term in Equation 2.22 is replaced with:

$$\boldsymbol{F}_{max}^{NEB} = -\boldsymbol{\nabla}V(\boldsymbol{Q}_{max}) + 2\boldsymbol{\nabla}V(\boldsymbol{Q}_{max}) \cdot \hat{\boldsymbol{\tau}}_{max} \tag{2.23}$$

for the image with the maximum energy, to ensure that it finds the very top of the pass[52].

The CI-NEB method is implemented in LAMMPS, and can be added to VASP by installing the Transition State Tools package[51, 52].

Chapter 3:

$\langle a \rangle$-Type Screw Dislocation Core Structures at 0 K and 0 Applied Stress

This chapter includes work that has previously been published in Reference[53] with the permission of co-authors.

3.1 Introduction

In hexagonal close packed (hcp) α-titanium alloys the glide of $\langle a \rangle$-type screw dislocations with Burgers vector $a\frac{\langle 11\bar{2}0 \rangle}{3}$ on the $\{1\bar{1}00\}$ (prismatic) planes plays a dominant role in plastic deformation[16]. These screw dislocations are by far the most commonly observed deformation mechanism in α-titanium alloys, and motion of these dislocations accounts for the majority of plastic deformation at common operating temperatures and strain-rates. The key role of dislocation core structure in controlling dislocation motion and dynamics[12] is well known in bcc[6], fcc[7], and hcp[8–11] metals. However, the configuration of $\langle a \rangle$-type screw dislocation cores in titanium (along with many other metal systems) is not fully understood in part because the compact nature of the dislocation core has prevented a complete experimental analysis. Therefore gaining a better understanding of these cores through atomistic modeling is of significant value to predicting the mechanical properties of α-Ti and its alloys.

Dislocation core spreading and the resulting effects on slip were first introduced by Peierls[13] and expanded on by Nabarro[14]. According to their model, for a given Burgers vector, line direction, and material there is a plane in which the dislocation will have a minimal barrier to slip. For a dislocation with edge character this plane will always be the plane that contains both the Burgers vector and line direction, but for a pure screw dislocation these directions are parallel and thus there are many possible glide planes.

The geometry of the hcp system and the relevant slip planes is illustrated in Figure 3.1. An example $\langle a \rangle$-type screw dislocation would be aligned along the blue vector, and be able to slip on any of the highlighted planes (as well as any others containing the Burgers vector, in principle), as all three contain the Burgers vector/line direction of the screw dislocation.

As illustrated by Clouet *et al.*[10] in recently reported density-functional-theory (DFT) based calculations, the difference in energies of screw dislocation cores spread on different planes can be very small, and yet the differences still have significant implications for plasticity in α-titanium. Clouet *et al.*'s calculations indicate that core spreading on the first-order pyramidal ($\{1\bar{1}01\}$, referred to simply as pyramidal going forward) plane is the stable configuration for $\langle a \rangle$-type screw dislocations in titanium. However, the barrier to cross slip onto the prismatic plane (i.e. a change of dissociation plane) followed by slip on the prismatic plane is lower than that for slip on the pyramidal plane. All of the energies involved are
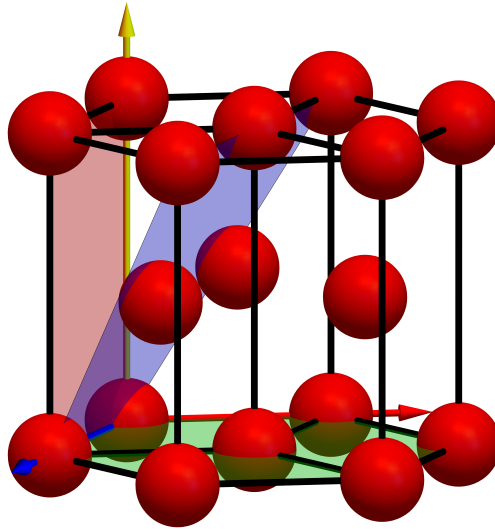
Figure 3.1: The hcp crystal system. Atom positions are red spheres, and the two ⟨a⟩-type lattice vectors are shown with red and blue, while the c lattice vector is yellow. The red, blue, and green planes are the prismatic {1$\bar{1}$00}, pyramidal {1$\bar{1}$01}, and basal (0001) planes. Three primitive cells are shown to highlight the hexagonal structure.

quite small: Clouet *et al.* found these mechanisms to have energy barriers of 21.7 meV/b and 33.4 meV/b respectively, where b indicates the magnitude of the Burgers vector, which is approximately 2.93 Å for these dislocations. However, cross slip involves large dislocation segments, magnifying these differences. Therefore this small difference is able to explain the previous in-situ TEM observation of "jerky" slip in titanium[8]. Because the largest barrier along the prismatic slip path is the change between core configurations it was proposed that prismatically spread cores are "unlocked" and free to slip with little barrier, while pyramidally spread cores are "locked" and must await activation into the prismatic configuration before slipping. Clearly accurate predictions of slip behavior require sufficient precision to both find the ground-state core configuration as well as the energetic difference between that configuration and other nearby configurations.

Several authors have examined ground-state core configurations for ⟨a⟩-type screw dislocations in hcp titanium recently[10, 54–56]. While these studies all include DFT results, they vary significantly in simulation cell configuration as well as calculation parameters. In the DFT calculations of Clouet et al., periodic supercells were used and the results indicate a stable pyramidal core configuration as well as a metastable prism configuration that is only slightly higher in energy[10]. Ghazisaeidi and Trinkle performed both DFT and modified embedded atom method (MEAM) classical potential calculations using a lattice Green function boundary condition approach, finding a mirrored (prismatic) core configuration that was 12 meV/b lower in energy than an unmirrored (mixed prismatic/pyramidal) configuration within the MEAM potential[54]. Due to the boundary conditions, they are not able to compare core structure energies in DFT. Similarly, Rao et al.[57] found that the prismatic dislocation core is the stable configuration in the MEAM potential within fixed boundary

conditions. DFT calculations by Yu et al. employed periodic supercells to find a stable configuration with an asymmetric prismatic core that appears to have a small component in the pyramidal plane[58]. Tarrat et al. found six different core configurations in DFT calculations by varying the initial position of the singularity of the dislocation when it is introduced into their pseudo-hexagonal cluster simulation cell[56]; all six of these configurations were found to have excess energies within approximately 22.6 meV/b of each other, and an asymmetric core of mostly prismatic character was found to be the stable configuration.

In the modeling of dislocation cores by atomic-scale simulations the results can be affected by convergence issues associated with the supercell size and geometry, numerical settings in the DFT calculations, and the choice of interatomic potential model for classical simulations. Considering first the size effects, if I assume from the outset that the calculations are modeling a straight dislocation (i.e. the periodic dimension of the supercell along the line direction as short as possible), I might at least hope to model physically realizable dislocation densities. In α-titanium alloys that have been cold worked 9%, one might observe dislocation densities as high as 3×10^{14} m^{-2} (3×10^{-6} Å^{-2})[16]. Within the periodic boundary condition approach at least two dislocations per supercell are required. A dislocation density of 3×10^{14} m^{-2} corresponds to $\sim$350000 atoms per supercell, well beyond the capacity of brute-force DFT calculations. In addition to the quadrupolar configuration used in this work, there are several approaches to first-principles dislocation modeling with the goal of eliminating - to the largest extent possible - effects associated with the finite size of the supercells. These include the approaches of Woodward and Rao[59] and Zhao and Lu[60], which in general use a high-precision calculation technique near the dislocation core, assume little distortion from a perfect lattice far from the core, and bridge these regions by an appropriate method. In all cases checks are needed to ensure the final results are not affected by the details of the simulation geometry and size. Additionally, these methods lead to difficulty in calculating energy differences between different structures.

The second set of convergence issues arises in all DFT calculations. Parameters related to the basis set and the sampling of electronic states, as well as the choice of exchange-correlation potential can all influence significantly both calculation accuracy and cost. In assessing convergence with respect to these various parameters, it is important to emphasize that I am interested in results beyond simple energies and forces, such as the configuration of atoms in the dislocation core region. More specifically I wish to know which of several possible dislocation core configurations (and possibly their superpositions) is the ground-state. Determining this configuration from the atom positions is not exact or straightforward, and therefore stating whether a calculation has converged to a given structure is not easily done. Considering these difficulties and the differences in cell configurations between the various studies, it is not surprising that there has been disagreement between previously published computational results.

Here I demonstrate the dependence of the calculated ground-state dislocation core structure on a number of parameters and suggest minimum settings for converged calculations by DFT. In the present work I consider two arrangements (Figure 3.2) of periodic arrays of dislocations and demonstrate the high sensitivity of the final core structures to choice of valence electronic states and k-point mesh density. Within each arrangement I also use two initial positions of the dislocations, one between basal planes and the other within basal planes.

(Meta)stable pyramidal and prismatic dislocation core structures exist within both the DFT and MEAM potentials, and the relaxed structure resulting from my anisotropic elasticity theory solution depends only on the initial dislocation positions. The pyramidal configuration results when the dislocations are initialized between basal planes, and the prismatic configuration results when the dislocations are initially within basal planes. In DFT I find the ground-state core structure to be purely pyramidal. I find that it is necessary to include the semi-core $3p$ electrons as valence states in order to converge the ground-state dislocation core configuration in either arrangement, and in particular to correctly find the difference in energy between this state and other metastable core configurations. It is demonstrated that a k-point mesh of at least $1 \times 1 \times 15$ is necessary to converge the dislocation core structure for a supercell one Burgers vector deep. Use of higher k-point densities or inclusion of additional semi-core electronic states as valence electrons results in the same core structure. I include MEAM calculations to demonstrate the effects of supercell size, and these findings suggest that my DFT calculations are performed with large enough supercells to avoid significant finite-size effects associated with stress gradients near the dislocation core structures.

3.2 Methods

All DFT calculations were performed using the Vienna ab initio simulation package (VASP)[35, 36]. The projector-augmented wave (PAW)[26, 61] method was used, and the calculations were performed spin-averaged. Three PAW potentials for titanium were tested, all of which are based on the Perdew-Burke-Ernzerhof (PBE)[25] form of the general gradient approximation (GGA). The three functionals differ in which electrons are frozen in the core, versus considered as part of the valence states. The standard functional ($4s$-valent) includes 4 valence electrons ($3d^2 4s^2$), the pv functional ($3p$-valent) includes 10 ($3d^2 4s^2 3p^6$), and the sv potential ($3s$-valent) includes 12 ($3d^2 4s^2 3p^6 3s^2$). Inclusion of more electrons improves calculation accuracy, but significantly increases the computational cost. Brief convergence testing (based on the requirement that the energy term due to entropy of the electron system at the effective electronic temperature associated with the finite smearing be no larger than 0.001 eV/atom) led to the choice of second-order Methfessel-Paxton smearing [28] with a broadening of 0.2 eV. After other parameters were converged, broadenings of 0.15 eV and 0.1 eV were tested and no changes to the dislocation core structure were found. The cutoff energies for the plane wave basis were 400 eV, 600 eV and 700 eV for the $4s$-valent, $3p$-valent, and $3s$-valent potentials, respectively. These were compared to calculations with cutoff energies of 600 eV, 700 eV and 800 eV, respectively and all other parameters set to converged values. No substantial differences were found, indicating the first set of cutoffs was sufficient for convergence. Electronic structure self consistency loops were terminated at an energy tolerance of 10^{-6} eV, and ionic relaxation was terminated at a force tolerance of 0.002 eV/Å.

For all dislocation calculations I use periodic dislocation arrays arranged such that each dislocation has four nearest neighbors, and every dislocation has the opposite sign of Burgers vector from its neighbors. These arrangements are known as quadrupolar, and minimize the elastic energy of a periodic dislocation array due to some cancellation of long-range stress fields[62]. The line direction of all dislocations is $[11\bar{2}0]$, and therefore the Burgers vectors
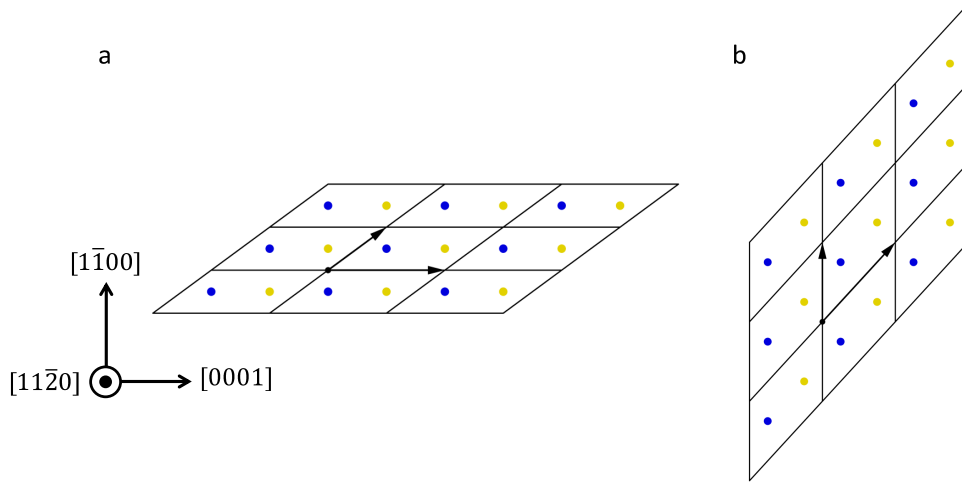
Figure 3.2: Outlines of supercell configurations used for dislocation calculations. Arrows indicate lattice vectors for a single supercell. (a) shows the O arrangement, which has dislocations of opposite signs (positions indicated by dots, with Burgers vector sign corresponding to color) alternating on the same basal and prism planes. (b) is the S arrangement, which has dislocations of only one sign on a given basal or prism plane.

for the $\langle a \rangle$-type screw dislocations are $\pm a \frac{[11\bar{2}0]}{3}$. Dislocation supercells are oriented such that [0001] is parallel to the x-axis, [1$\bar{1}$00] is parallel to the y-axis, and the line direction/Burgers vector [11$\bar{2}$0] is parallel to the z-axis. Supercell lattice vectors are tilted to account for the distortion from the dislocations as prescribed by Lehto and Öberg[63]. Initial displacements were determined using the method of Daw[62], which yields good starting points that account for elastic anisotropy while only requiring lattice parameters and elastic constants as inputs.

For DFT calculations of dislocations I use supercells in both the so-called O and S arrangements (outlines of these supercells are shown in Figure 3.2 a and b) for dislocation quadrupoles[9] with two dislocations per unit cell. It is useful to compare these configurations because while both result in zero stress at the dislocation centers, the gradient in the stress is quite large in small supercells. This gradient differs for different quadrupolar configurations, and because the dislocation cores spread beyond their centers one might expect different stress gradients to lead to different ground-state core configurations. DFT calculations were performed on an O-arranged supercell with 12 periodic units along the x-axis, 4 along y-axis, and 1 along the z-axis for a total of 192 atoms, as well as an S-arranged supercell with 8 periodic units along the x-axis, 8 along y-axis, and 1 along the z-axis for a total of 256 atoms. These arrangements were selected to maximize the separation of dislocations along the prism plane without increasing the number of atoms past a reasonable number for DFT calculations.

For calculations involving either quadrupolar arrangement I proceeded by taking the configuration generated by linear anisotropic elasticity theory code and relaxing ionic positions in VASP, starting with a low number of k-points and gradually increasing until no further changes in the core configurations are observed. In this way k-point convergence proceeds independently for each PAW potential considered. An issue that arises during this process

is that convergence of the core configuration is not as clearly defined as typical convergence criteria such as energy or force tolerances. There is, to my knowledge, no commonly recognized order parameter by which a core structure can be characterized. Therefore the tasks of classification and determination of convergence of core structures are performed manually. Two calculations are performed to assist this task: Nye tensor analysis (via the method of Hartley and Mishin[64]), and differential displacement maps (also know as "arrow plots", following Vitek[6]).

In the differential displacement map representation, the dislocation core is imaged as a set of arrows pointing between neighboring columns of atoms. The length of each arrow depends on the differential displacement between the columns, i.e. the change in the displacement when a dislocation is introduced to the system. For this reason, one requires a reference configuration (a perfect lattice of the similar geometry but containing no dislocations) to generate the differential displacement map. Call the set of atomic positions in the reference state $\boldsymbol{r}^{ref}$ and the positions after the dislocation has been introduced $\boldsymbol{r}^{dis}$. The length (l) of the arrow connecting columns i to column j is:

$$l = ((\boldsymbol{r}_i^{dis} - \boldsymbol{r}_j^{dis}) - (\boldsymbol{r}_i^{ref} - \boldsymbol{r}_j^{ref})) \cdot \boldsymbol{b} \frac{\left|(\boldsymbol{r}_i^{dis} - \boldsymbol{r}_j^{dis})\right|}{3\left|\boldsymbol{b}\right|} \tag{3.1}$$

where $\boldsymbol{b}$ is the Burgers vector and the last term in the scaling enforces that a loop of three perfectly connected arrows (cycling uniformly) represent enclosure of the full Burgers content of the dislocation. Any other path which sums to three arrows fully connecting columns also encloses the full Burgers vector. The length of the arrows is a representation of the amount of distortion created by the dislocation, and if long arrows are extended along a plane, this indicates the dislocation is spread in that plane.

The Nye tensor is an alternative method for visualizing the distribution of Burgers vector content. It is more detailed but also more involved to compute. The definition of the Nye tensor $\boldsymbol{\alpha}$ is:

$$\boldsymbol{\alpha} = \int_A (\boldsymbol{\alpha} \cdot \boldsymbol{n}) ds \tag{3.2}$$

where A is the surface of a circuit that completely encloses the Burgers vector and $\boldsymbol{n}$ is the normal to that surface[64]. Now consider sets of lattice vectors $\boldsymbol{x}^{ref}$ and $\boldsymbol{x}^{dis}$, and a transformation $\boldsymbol{G}$ such that $\boldsymbol{x}^{dis} = \boldsymbol{x}^{ref} \cdot \boldsymbol{G}$. By definition for the perfect reference system on any path C^{ref}, one knows $\int_{C^{ref}} d\boldsymbol{x}^{ref} = \boldsymbol{0}$. By the Burgers construction then, $\int_{C^{dis}} d\boldsymbol{x}^{dis} = -\boldsymbol{b}$. Combining this with the definition of $\boldsymbol{G}$:

$$\boldsymbol{b} = -\int_{C^{ref}} d\boldsymbol{x}^{ref} \cdot \boldsymbol{G}. \tag{3.3}$$

Then by Stokes' theorem:

$$\boldsymbol{b} = -\int_A ((\boldsymbol{\nabla} \times \boldsymbol{G}) \cdot \boldsymbol{n}) ds. \tag{3.4}$$

Finally, combining Equations 3.2 and 3.4 yields the expression used to calculate $\boldsymbol{\alpha}$[64]:

$$\boldsymbol{\alpha} = -(\boldsymbol{\nabla} \times \boldsymbol{G}). \tag{3.5}$$

Thus, calculation of the Nye tensor requires computing the lattice correspondence tensor that connects the reference and dislocation atomic configurations, and taking its curl. In

a 3-dimensional simulation, the Nye tensor has 9 components. For the purposes of this dissertation which focuses on screw dislocations, only the screw component is visualized. This is the diagonal entry corresponding to line the direction of dislocation. The Nye tensor is typically visualized as a density plot. This makes it convenient to overlay the Nye tensor and differential displacement map representations of the dislocation core structure.

Classical potential calculations were performed using the Large-scale Atomic/Molecular Massively Parallel Simulator (LAMMPS)[42]. The modified embedded atom method[41] (MEAM) potential of Hennig et al.[65] for titanium was used. This potential is advantageous in that it reproduces the elastic constants of α-Ti well and was fit to a number of defect energies for this structure. However, the potential was not fit to properties specific to dislocations. This leads to some discrepancies between DFT and MEAM results, as discussed below. Despite these differences the significantly reduced computational cost of MEAM relative to DFT allows us to use much larger supercells and thereby examine finite-size effects in my calculations. For MEAM calculations of dislocations I again used both O- and S-arranged supercells, and varied the size of both arrangements from the size used for DFT calculations up to supercells with over 1000 atoms. Relaxations were performed at zero temperature and terminated when the norm of the forces on all atoms is less than 1 μeV$/$Å.

3.3 Generalized Stacking Fault Energy Calculations

A useful preliminary to dislocation core structure calculations is to calculate the Generalized Stacking Fault (GSF) energy surface[66] for the system of interest. In GSF calculations a continuum of possible stacking faults on a selected plane are considered, and an energy surface representing these is formed. This energy surface can provide an idea of what the dislocation behavior will be, because a stacking fault is analogous to a dislocation core of infinite width spread on the plane of the fault. Planes that have low-energy paths across the GSF surface in the direction of a Burgers vector of interest will accommodate slip of dislocations with that Burgers vector more easily than those where all paths are high-energy. Also, accessible local minima in the GSF surface may indicate possible dislocation dissociation configurations.

I performed GSF calculations for pure titanium first within the MEAM potential. Three planes were of interest, because they represent the lowest-index planes along which $\langle a \rangle$-type screw dislocations can slip. These were the prismatic, pyramidal, and basal planes. In the case of the prismatic and pyramidal planes, there are two variants of each plane – one with narrow spacing (referred to as "dense"), and one with wide spacing (referred to as "loose"). This is a consequence of the two-atom basis in hcp. GSF calculations for both dense and loose prismatic and pyramidal planes were carried out to determine which is preferred for dislocation slip. The results for the prismatic planes are shown in Figure 3.3, pyramidal in Figure 3.4, and basal in Figure 3.5. Fortunately, these planes have short periodic lengths. In the plane of interest only one unit vector in each direction is required. Perpendicular to this plane I used enough layers to make the system roughly 30 Å tall, then added a vacuum gap of 15 Å to avoid creating a second stacking fault layer in the supercell. The system is able to relax into this gap along the vertical direction to accommodate the stacking fault layer.

These GSF calculations yield a few interesting observations. The most significant are
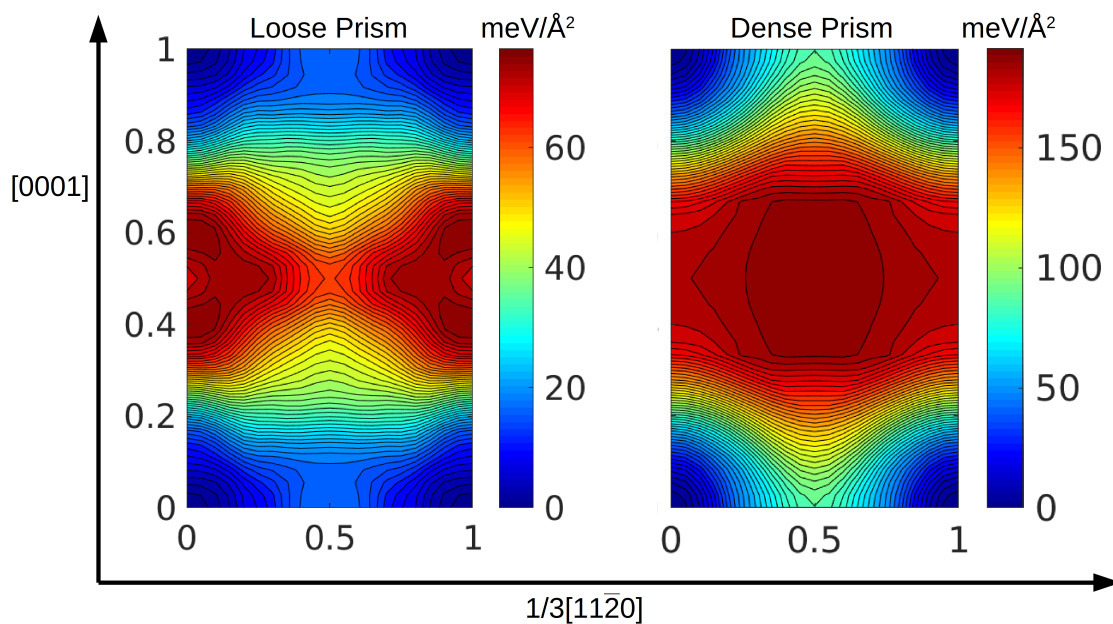
Figure 3.3: Stacking fault energy surfaces calculated from MEAM on the loose and dense prismatic planes.
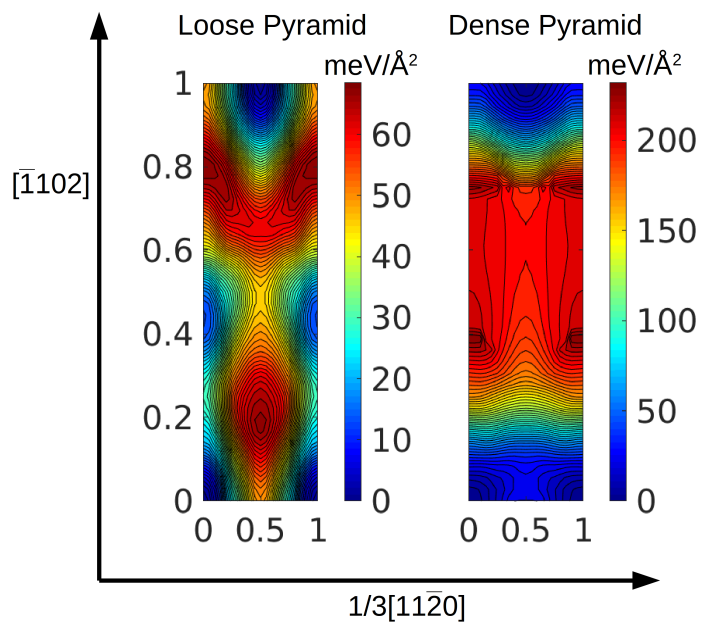

Figure 3.4: Stacking fault energy surfaces calculated from MEAM on the loose and dense pyramidal planes.
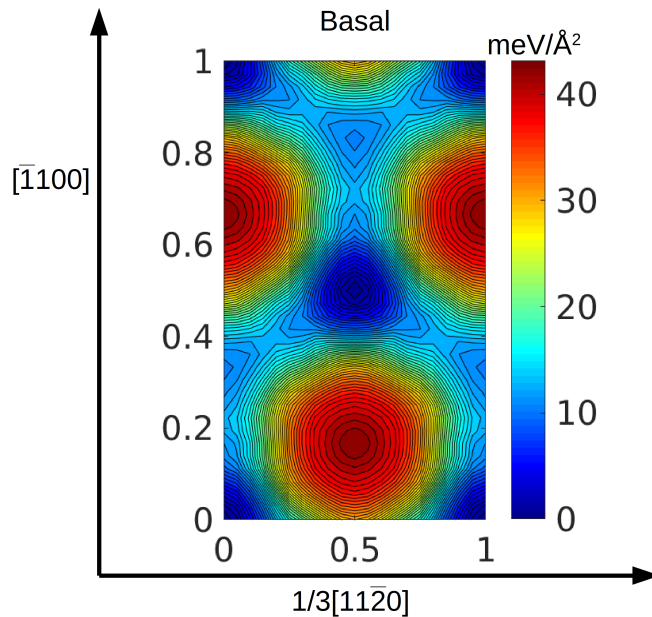
Figure 3.5: Stacking fault energy surfaces calculated from MEAM on the basal plane.

that slip appears simplest on the loose prismatic plane, where slipping directly along the Burgers vector direction (i.e. the x-axis on the plot) requires overcoming a barrier of only 17 meV/Å^2. The dense prismatic plane appears totally unfavorable, with no low-energy paths or local minima. More curious is the pyramidal plane. The dense pyramidal plane has regions of much higher energy than the loose variant, as one would expect. However, the path along the Burgers vector direction is relatively unobstructed, with a minimum barrier of 25 meV/Å^2 at a position halfway along the Burgers vector direction and slightly displaced along the [$\bar{1}$102] direction. While overall the energies on the loose variant are lower, its minimum barrier for slip is 49 meV/Å^2. The basal plane displays a local minimum midway along the Burgers vector direction, and a minimum slip barrier of only 13 meV/Å^2 if a rather indirect path across the surface is taken. This is surprising, as basal core spreading is not observed experimentally in pure titanium. It is likely that this barrier is underestimated within the MEAM potential.

Next, I undertook to repeat portions of the above calculations within DFT. Because DFT calculations are significantly more computationally intensive than MEAM, I was more selective about which calculations were performed. I eliminated the dense prismatic plane and the loose pyramidal plane completely, as the other variants of these were much lower in energy in the MEAM calculations. For the loose prismatic plane and dense pyramidal plane, only sections of the GSF surface were calculated. Regions away from the x-axis were ignored as they were found to be much higher in energy, and only the left half of the surface was calculated due to the symmetry of the GSF surfaces. Results for the loose prismatic is shown in Figure 3.6, dense pyramidal in Figure 3.7, and basal in Figure 3.8.

The DFT results largely – but not completely – agree with those from MEAM. On the loose prism plane the minimum barrier is 15 meV/Å^2 halfway along the [11$\bar{2}$0] axis. On the
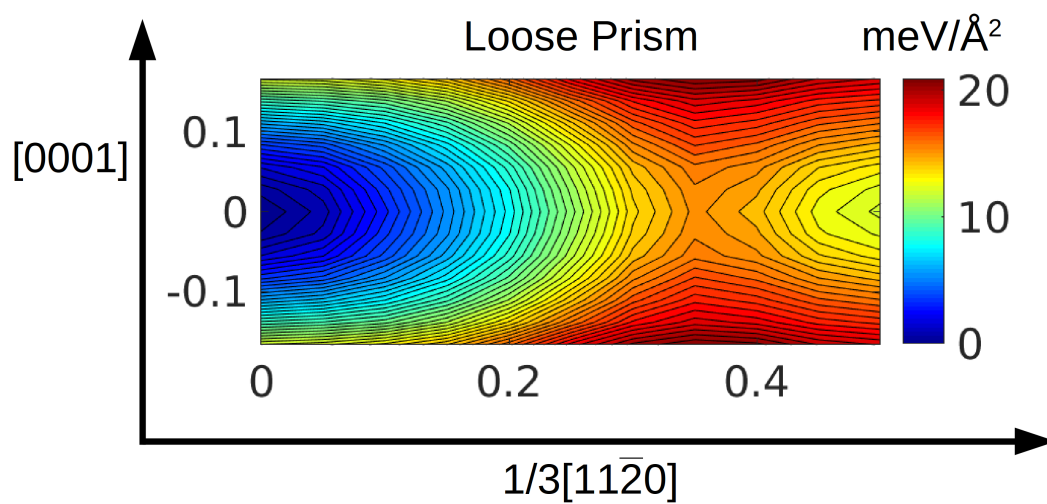
Figure 3.6: Stacking fault energy surfaces calculated from DFT on the loose and dense prismatic planes.
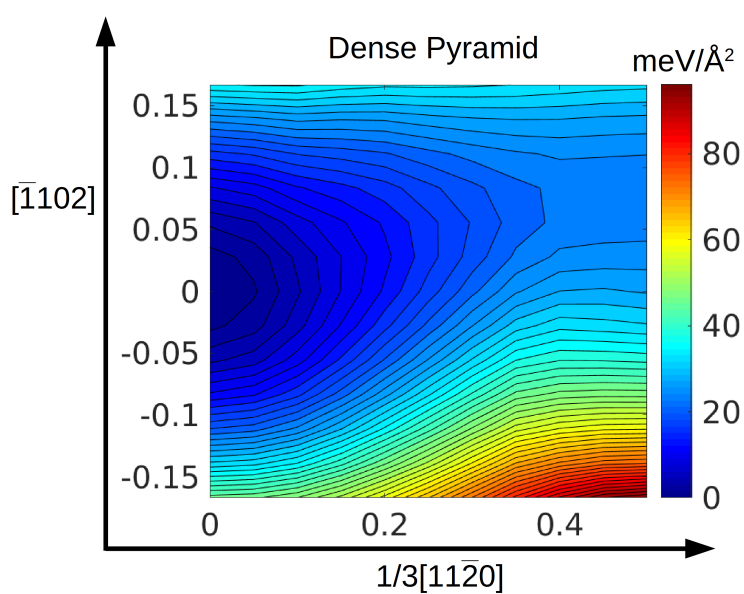

Figure 3.7: Stacking fault energy surfaces calculated from DFT on the loose and dense pyramidal planes.
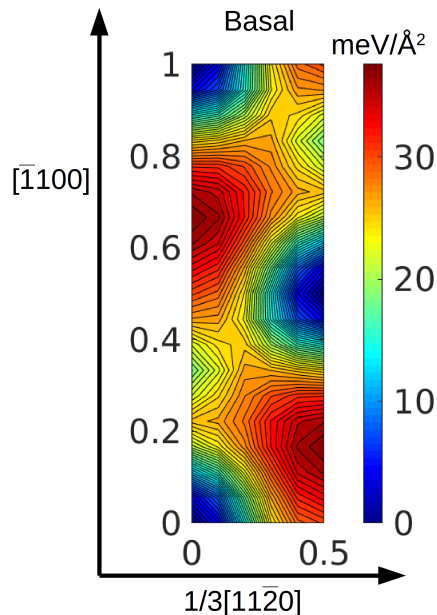
Figure 3.8: Stacking fault energy surfaces calculated from DFT on the basal plane.

dense pyramidal plane the minimum barrier is 23 meV/ Å^2, and again it occurs at a position with a small displacement in the $[\bar{1}102]$ direction. The most significant difference from the MEAM results is that the barrier to the dissociation on the basal plane is 26 meV/ Å^2, twice as high as in MEAM. This agrees with the previous speculation that the MEAM is in error in this case. However, the good agreement for the two more relevant planes is encouraging for using the MEAM potential in place of DFT for calculations that are not feasible in DFT.

3.4 Core Structure Calculations

3.4.1 DFT

Relaxation of the 192 atom O-arranged supercell with dislocations placed between basal planes within the $4s$-valent potential and a $1 \times 1 \times 4$ k-point grid results in a clearly prism-oriented dislocation core structure that is spread approximately 4 c-vectors in width, with minimal spread in the perpendicular (basal) direction (approximately 1 a-vector). A differential displacement map and the screw component of the Nye tensor for a dislocation core relaxed with these settings is shown in Figure 3.9a. The width of spreading is determined from the differential displacement map construction, using a cutoff of a $\frac{b}{6}$ displacement of neighboring columns of atoms. When the k-point mesh in increased gradually to a $1 \times 2 \times 19$ mesh the width along the prism plane is reduced to 3.5 c-vectors and the width in the basal plane increased to 1.5 a-vectors (Figure 3.9c). While the structure remains mostly prismatic in nature, its symmetry is reduced such that it is apparent that it has gained a pyramidal component to the spreading of the core. Most of this change in core structure is captured by a $1 \times 1 \times 9$ k-point mesh (Figure 3.9b), but plotting displacement magnitudes between

relaxation with this mesh and with the $1 \times 2 \times 19$ mesh shows that there are still some small differences in dislocation core structure that require the higher k-point density to capture. Different core structures are separated by only tenths of Angstroms in terms of atomic coordinates, and rearrangements on the scale of hundredths of Angstroms within a core structure are important to capture if I wish to directly compare the energies of different structures.

Use of the $3p$-valent potential and a $1 \times 1 \times 4$ k-point mesh results in almost the same prismatic core structure as for the same mesh and $4s$-valent potential. However, use of higher k-point density in the $3p$-potential leads to much more significant changes in the core structure. With a $1 \times 1 \times 9$ k-point mesh I find a core structure that is almost equally split between prismatic and pyramidal spreading (based on the differential displacement map) where the right-hand side of the structure appears to be spread on one plane and the left-hand the other. Increasing the k-point density to $1 \times 1 \times 15$ I find a pyramidal structure with only small tails that extend along the prism plane. Further increase of the k-point density to $1 \times 2 \times 25$ leads to only very small (thousandths of Å) changes in atom positions and I obtain essentially the same dislocation core structure. Figure 3.9d-f shows the progression of relaxed core structures with increasing k-point mesh density when the $3p$-valent potential is used.

I find that use of the $3s$-valent potential results in the same pyramidal configuration observed with a k-point density that is well converged for the $3p$-valent potential. In the $3s$-potential all k-point meshes used result in this pyramidal core structure. Comparing relaxation with various k-point meshes in the $3s$-valent potential to relaxation with the $1 \times 2 \times 25$ mesh in the $3p$ potential, displacement magnitudes are larger for lower k-point densities and uniformly reduce as k-point density is increased. The atomic positions in the configuration computed with the highest k-point density used in conjunction with the $3s$ valent potential ($1 \times 2 \times 15$) differ from the converged result of the $3p$ valent potential by less than one hundredth of an Angstrom. Therefore I find that the $3p$ valent potential is sufficient to determine the ground-state dislocation core structure, and the inclusion of $3s$ semicore states in the valence has minimal effect.

With this pyramidal core configuration stabilized, it is possible to calculate the energy associated with this structure at different parameter settings either with the atomic positions held fixed or permitted to relax. In both the $4s$-valent and $3p$-valent potentials with $1 \times 1 \times 4$ k-point mesh, this pyramidal configuration is significantly higher in energy than the prism structure presented, and is unstable when atomic positions are relaxed. For higher-density k-point meshes this pyramidal structure is actually lower in energy than the prism configurations that resulted from the initial relaxation, but the energy differences between the structures are significantly different from those found under converged conditions. For example, use of the $4s$-valent potential in conjunction with a $1 \times 1 \times 15$ or a $1 \times 2 \times 19$ k-point mesh results in an energy difference between pyramidal and prismatic structures roughly double that found under converged conditions. On the other hand, use of lower-density k-point meshes within the $3p$-valent potential results in an underestimate of the energy difference between core structures. These energy differences are summarized in Table 3.1.

Returning to the settings sufficient to find the converged pyramidal core structure ($3p$-valent potential and $1 \times 1 \times 15$ k-point mesh), I can stabilize a prismatic dislocation core
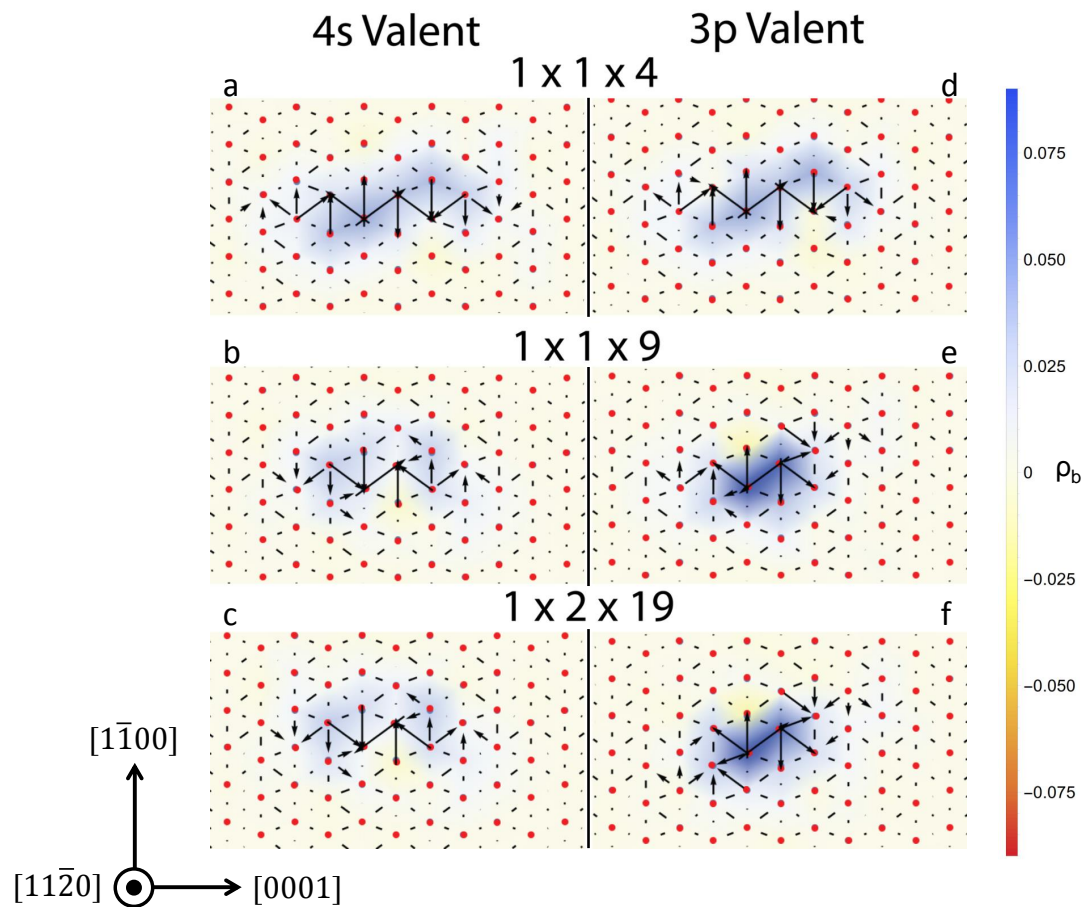
Figure 3.9: Relaxed dislocation core structures calculated with different DFT parameters. Dots represent columns of atoms, arrows are from the differential displacement map construction[6] and coloring between atoms represents the screw component of the Nye tensor. a-c result from the 4s-valent potential, d-f from the 3p-valent potential. a and d used a $1 \times 1 \times 4$ k-point mesh density, b and e $1 \times 1 \times 9$, c and f $1 \times 2 \times 19$. The core structures in a-d are purely prismatic, e is mixed pyramidal and prismatic, and f is entirely pyramidal.

Table 3.1: Difference in energy between prismatic and pyramidal dislocation core structures (i.e. $E_{prismatic} - E_{pyramidal}$) for calculations using different semicore states and k-point mesh densities. * indicates that pyramidal core structure was unstable, and the energy for the pyramidal core corresponds to a calculation on the converged-settings atomic positions under the indicated parameter settings.

Potential Valence	k-Point Mesh	$E_{prismatic} - E_{pyramidal}$ per b [meV]
$4s$	$1 \times 1 \times 4$	-118.3*
$4s$	$1 \times 1 \times 9$	29.2
$4s$	$1 \times 1 \times 15$	32.5
$4s$	$1 \times 2 \times 19$	33.7
$3p$	$1 \times 1 \times 4$	-89.7*
$3p$	$1 \times 1 \times 9$	11.4
$3p$	$1 \times 1 \times 15$	18.4
$3p$	$1 \times 2 \times 19$	18.4

structure by relaxing from a configuration where the initial position of the dislocation line is in a basal plane rather than between basal planes (as used in the above). This prismatic core structure was found to be 18.4 meV/b higher in energy than the pyramidal core structure, in good agreement with the results of Clouet et al.[9]. This prismatic core structure is not equivalent to that which is found to relax from the inter-basal initial site when insufficient k-point density is used. The prism core resulting from insufficient convergence is more extended on the prism plane, and is unstable at higher k-point densities. This new structure that results from the alternative dislocation placement is metastable under fully converged conditions. Further, I find that a mixed prismatic/pyramidal core structure is also metastable with these same parameter settings, if relaxation is initiated from a mixed configuration. This mixed configuration is 12.6 meV/b higher in energy than the pyramidal configuration.

Use of the $3p$-valent potential and $1 \times 1 \times 4$ k-point mesh in conjunction with the traditional 256 atom S-arranged supercell with dislocations placed initially between basal planes leads to the same result as for the O configuration: the core structure is extended along the prism plane with no pyramidal component. Also in agreement with the results from the O arrangement, I find a similar mixed prismatic/pyramidal core structure when a $1 \times 1 \times 9$ mesh is used. However the results of the two configurations begin to differ at this point. For higher k-point mesh densities the core configuration in the S arrangement does not become fully pyramidal, but instead remains in the mixed state described above. Increased k-point mesh density up to $2 \times 2 \times 15$ yields similar results, as does use of the $3s$-valent potential. This core structure is shown in Figure 3.10b. As in the O arrangement no changes are found for meshes denser than the k-point mesh of $1 \times 1 \times 15$.
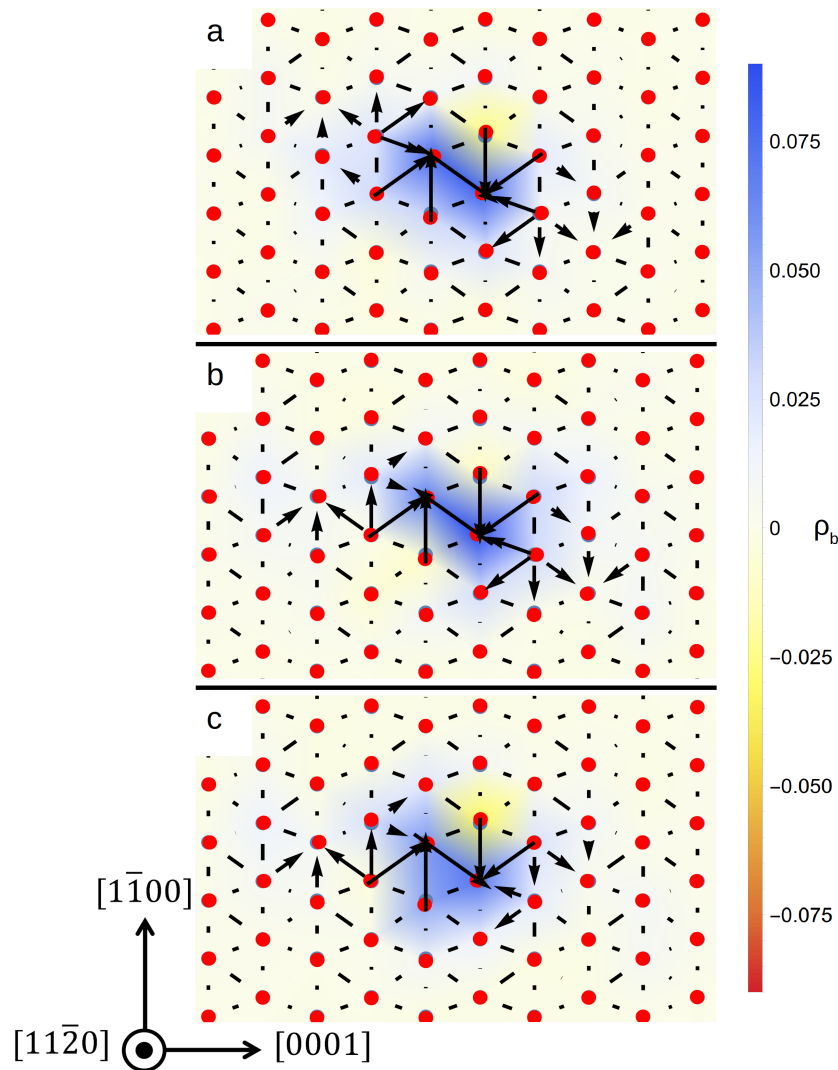
Figure 3.10: DFT calculated core structures in S-type 256-atom supercell: (a) stable pyramidal core structure, (b) metastable mixed core structure, and (c) metastable prism core structure.

As with the O-arranged supercell I also placed the dislocations initially within basal planes and thereby stabilized prismatic dislocation cores (Figure 3.10c). In this configuration this core structure is 10.2 meV/b higher in energy than the mixed core.

One complicating factor in the S arrangement is that the elastic energy of the system can be lowered by moving the dislocations on the prism plane, but without resulting in dislocation annihilation because the dislocations are immobile on the basal plane. This results in a dipolar arrangement. I placed dislocations initially in this arrangement (in which dislocations of opposite sign lie in the same basal plane) in the inter-basal site and allowed them to relax. The result was a pyramidal core structure (Figure 3.10a) which is lower in energy than the mixed structure by 10.7 meV/b after accounting for the change in elastic energy due to the displacement of the dislocations following the method of Daw[62]. The basal site is not possible in this arrangement and therefore was not also tested.

The relative energies of the three dislocation core structures in the two arrangements are summarized in Table 3.2. The stable pyramid configuration is taken as reference in each configuration. The energy differences between the various core structures show only a weak dependence on the arrangement used.

Table 3.2: List of the 6 core structures stabilized in DFT and energy found for each. The energy is taken relative to the pyramidal structure for each configuration, which in both cases is the stable core structure.

Arrangement	Number of Atoms	Core Structure	Relative Energy per b [meV]
O	192	Pyramidal	-
O	192	Mixed	12.6
O	192	Prismatic	18.4
S	256	Pyramidal	-
S	256	Mixed	10.7
S	256	Prismatic	20.9

3.4.2 MEAM

The goal in undertaking MEAM calculations on these dislocation cores is to determine to what degree the predictions of the potential agree with DFT calculations, and to gain some insight into supercell size and configuration effects. To this end I performed relaxations of quadrupolar dislocation configurations in both the O and S arrangements, and in each arrangement used multiple supercell sizes ranging from the corresponding size in the DFT simulations to over 1000 atoms. Four sizes of the O arrangement were used, and three sizes of the S arrangement. For each arrangement and size I utilized two initial positions of the dislocations, thus there were 14 configurations in total. The configurations as well as the resulting structures and energies are summarized in Table 3.3.

As in the DFT calculations, placing the dislocations initially between basal planes results in a pyramidal core structure, while placing the dislocations within basal planes results in a prismatic core structure. Thus the MEAM potential also finds the two structures to be metastable, as previously demonstrated by Ghazisaeidi and Trinkle[54]. My further findings also agree with those previously obtained using the same potential, in that the predicted core structure is predominantly prismatic. I find this to be the case at any supercell size and configuration except the smallest O-arranged supercell. For this outlier I find that there is overlap of Nye tensor distributions between neighboring dislocation cores after relaxation

Table 3.3: List of the 14 quadrupolar configurations used with MEAM and the resulting core structure and energy found for each configuration. The energy is taken relative to the prism structure for each configuration. The only pyramid configuration for which this energy is negative is the smallest (192 atom) O-arranged supercell.

Arrangement	Number of Atoms	Core Positions	Core Structure	Relative Energy per b [meV]
O	192	Inter-basal	Pyramidal	-1.0
O	192	Basal	Prismatic	-
O	768	Inter-basal	Pyramidal	5.3
O	768	Basal	Prismatic	-
O	1728	Inter-basal	Pyramidal	7.8
O	1728	Basal	Prismatic	-
O	3072	Inter-basal	Pyramidal	9.1
O	3072	Basal	Prismatic	-
S	256	Inter-basal	Pyramidal	12.2
S	256	Basal	Prismatic	-
S	576	Inter-basal	Pyramidal	7.3
S	576	Basal	Prismatic	-
S	1024	Inter-basal	Pyramidal	8.7
S	1024	Basal	Prismatic	-

in the MEAM potential, which was not the case in DFT. This overlap is likely the cause of the stability inversion. This core overlap does not exist in any of the larger supercells. My largest calculations indicate that the prismatic core is stable, and is lower in energy than the pyramidal core by 9 meV/b in this MEAM potential. This is similar to the 12 meV/b reported by Ghazisaeidi and Trinkle[54] from calculations using lattice Green function boundary conditions, as well as the 4 meV/b reported by Rao et al.[57] within fixed boundary conditions.

3.5 Conclusions

I find that for sufficiently converged DFT calculations at feasible supercell sizes, the lowest-energy core structure of ⟨a⟩-type screw dislocations in hcp titanium is predicted to be spread on the first-order pyramidal plane. The DFT results are found to be sensitive to

the nature of the frozen core approximation and k-point sampling: inclusion of $3p$ semi-core states in the valence and at least 15 (k-points times Burgers vectors) along the dislocation line direction are required to obtain converged results for the core structure. I find that for underconverged calculations (particularly for insufficient k-point meshes) a prismatic or mixed dislocation core structure is predicted to be lowest energy. For the $4s$-valent potential the energy difference between core structures is overestimated, but it would also appear that the metastability of the prismatic core structure is enhanced since no combination of settings was sufficient to find the pyramidal configuration without starting the calculation in this configuration. This may explain some of the disagreement between published results, though it is likely that use of non-quadrupolar supercells may lead to different conclusions within calculations that are otherwise well-converged with respect to DFT parameters.

The lack of perfect agreement between calculations using different supercell configurations indicates that stress gradient effects are significant at these supercell sizes. Because dislocation cores have finite size, part of the core is subject to non-zero stresses even in a perfect quadrupole and these stresses influence relaxed atom positions. No known periodic supercell results in zero stress and zero stress gradient at the dislocation core and therefore these effects are always present to some degree. While increasing supercell size will decrease the stress gradient, this decrease is slow (the stress field around a dislocation falls off as $1/r$, and its gradient as $1/r^2$) and increasing the size a significant amount is not currently feasible within pure DFT calculations. Therefore it is important to note when examining or comparing dislocation core calculations that supercell configuration and resulting stress gradient plays a role in the calculated core structure.

Comparison to MEAM calculations suggests that my supercells for DFT calculations are large enough to avoid the most serious small supercell size effect, dislocation core overlap. However, this does not allow us to say for certain that the proximity of dislocations does not have any influence on the core structure. The elastic strain field around a dislocation decays algebraically, and therefore the interaction between neighboring dislocations is never completely eliminated. This applies in real materials as well as simulations, but the dislocation density in my DFT simulations is approximately three orders of magnitude higher than in even the most heavily cold-worked titanium. One solution to this issue is to use the Green's function boundary conditions introduced by Rao *et al.*[67], as done by Ghazisaeidi and Trinkle[54]. A recently developed method that couples DFT and EAM by matching electron densities between the two in a transition region[68] provides an electronic structure focused alternative. It has been demonstrated that by modeling the region around the dislocation core with DFT and allowing the long-range stress field to be relaxed in a classical potential, one can treat lower dislocation densities without significantly increasing the computational cost[60]. However, convergence with any of these methods still depends on the size of the DFT region and calculation of total energy is not available within these methods.

The second conclusion from the comparison between MEAM and DFT is that even for very similarly configured supercells the ground-state dislocation core structures do not agree. This is unfortunate because larger supercell sizes and finite temperature molecular dynamics simulations are much more accessible within MEAM. While the same dislocation core structures are possible within the potential of Hennig *et al.*[65], the prediction of Clouet et al. that locking unlocking mechanism in titanium is related to the dislocation core structure[10]

relies on the pyramidal core structure being the ground-state rather than simply a possible configuration.

Finally, it is important to note that all of these calculations are performed for perfectly straight dislocations. In my calculations the thickness of the supercell along the dislocation line is the magnitude of only one a-vector. This imposes the constraint that the dislocation does not bend and that there cannot be any variation of the core structure along the dislocation line. These conditions are necessary to complete these calculations with present resources, and it is reasonable to believe that the ground-state core structure is one that does not have any variation along the line direction. I can confirm that this is the case for dislocations in the MEAM potential for lengths up to 96 Burgers vectors. In the more realistic and useful scenario of finite temperature and applied stress causing dislocation motion, it is well known that dislocations bow at pinning sites. This is necessarily accommodated by deviation from the straight dislocation configuration used here and the nature of this deviation is likely significant to the dislocation motion and related material properties.

In summary for this chapter, I have four main findings:

1. Within DFT calculations using periodic quadrupolar supercells the calculated lowest-energy dislocation core structure of the $\langle a \rangle$-type screw dislocation in α-titanium is spread on the first-order pyramidal plane.

2. I find that it is necessary to include the semi-core $3p$ electrons as valence states in the DFT calculations, in order to converge the ground-state dislocation core configuration in either arrangement, and in particular to find the pyramidal component of the core structure.

3. It is demonstrated that a k-point mesh with at least 15 points along the Burgers vector direction is necessary to converge the dislocation core structure for a supercell one Burgers vector deep.

4. With the MEAM potential considered in this work, I find the ground-state core configuration to be spread predominantly on the prismatic plane, in contrast with the DFT results.

Chapter 4:

Non-Schmid Effects on ⟨a⟩-Type Screw Dislocation Core Structures

4.1 Introduction

Titanium alloys are known to exhibit a deviation from the Schmid law for dislocation slip[69–74]. In hcp α-titanium alloys the glide of ⟨a⟩-type screw dislocations with Burgers vector $a\frac{\langle11\bar{2}0\rangle}{3}$ on the $\{1\bar{1}00\}$ (prismatic) planes plays an important role in plastic deformation[16]. Experimental observations indicate there is a tension-compression asymmetry in the critical resolved shear stress (CRSS) for these dislocations[72, 73], and more generally a substantial loading orientation dependence of the CRSS[70, 71], particularly at lower temperatures. In these studies it was suggested that the non-Schmid law behavior may arise from a change in the core structure of the dislocations. The important role of dislocation core structure in controlling tension-compression asymmetry is well known in bcc metals[6], but the effect of applied stress on the configuration of a-type screw dislocation cores in hcp titanium has not been thoroughly investigated.

Under zero applied stress, the difference in energy between dislocation core structures can be very small and yet still have significant implications for plasticity in α-titanium, as discussed in Chapter 3. First-principles calculations indicate core spreading on the $\{1\bar{1}01\}$ first-order pyramidal plane is the energetically most stable configuration[10, 53], but that the barrier to cross slip into the $\{1\bar{1}00\}$ prismatic plane followed by slip on the prismatic plane is lower than that for slip on the pyramidal plane[10]. Here I show that stresses with zero RSS can have significant effects on the core structure of ⟨a⟩-type screw dislocations in titanium and thereby influence the energy barrier for slip. In particular, I find for certain directions of applied stress that compression (tension) enhances the pyramidal (prismatic) character of the dislocation core. The nudged elastic band method is used to calculate barrier energies and transition paths for dislocation slip. This allows me to determine how non-Schmid effects can influence dislocation mobility by changing the dislocation core structure. My results suggest that the tension-compression asymmetry may be attributable to these effects.

4.2 Methods

The setup and necessary calculation parameters for convergence of dislocation core structure calculations were discussed in Chapter 3 and published in Reference [53]. The following sections summarize those findings and the methods used in the present study.

4.2.1 Density Functional Theory

All DFT calculations were performed using the Vienna ab initio simulation package (VASP)[35, 36]. The projector-augmented wave (PAW)[26, 61] method was used, and the calculations were performed spin-averaged. Use was made of the Perdew-Burke-Ernzerhof (PBE)[25] form of the general gradient approximation (GGA), and the PAW potential employed in the calculations included the $3d^24s^23p^6$ electrons as valence states. The second-order Methfessel-Paxton smearing scheme[28] was used in the Brillouin-zone integrations with a width of 0.2 eV. The cutoff energy for the plane wave basis was 600 eV for dislocation core calculations. A Γ-centered k-point mesh with 15 points along the Burgers vector was used for all calculations. These calculation parameters are based on the convergence tests described in Chapter 3.

4.2.2 $\langle$a$\rangle$-type Screw Dislocations

For all dislocation calculations I use periodic dislocation arrays arranged such that each dislocation has four nearest neighbors, and every dislocation has the opposite sign of Burgers vector from its neighbors. These arrangements are known as quadrupolar, and minimize the energy of a periodic dislocation array due to cancellation of long-range stress fields[62]. The line direction of all dislocations is [$11\bar{2}0$], and therefore the Burgers vectors for the $\langle$a$\rangle$-type screw dislocations are $\pm a\frac{[11\bar{2}0]}{3}$. Dislocation supercells are oriented such that [0001] is parallel to the x-axis, [$1\bar{1}00$] is parallel to the y-axis, and the line direction/Burgers vector [$11\bar{2}0$] is parallel to the z-axis. Supercell lattice vectors are tilted to account for the distortion from the dislocations as prescribed by Lehto and Öberg[63]. Initial displacements were determined using the method of Daw[62], which yields good starting points that account for elastic anisotropy while only requiring lattice parameters and elastic constants as inputs.

For DFT calculations of dislocations I use cells with 12 periodic units along the x-axis, 4 along y-axis, and 1 along the z-axis for a total of 192 atoms. The O arrangement for dislocation quadrupoles[9] was used with two dislocations per supercell. This arrangement was selected to maximize the separation of dislocations along the prism plane while keeping the total number of atoms in the supercell at a level that was reasonable for performing well-converged DFT calculations.

4.2.3 Nudged Elastic Band Method

Energy barriers for dislocation slip were calculated via the nudged elastic band (NEB) method[50]. We employed the implementation of this approach within VASP available through the Transition State Tools package[52, 51]. For prism slip the endpoints are taken to be the relaxed configuration of the dislocation and the same configuration translated by a [0001] lattice vector. Linear interpolation is used to create the initial configuration for each image, and there were 3 intermediate images. In the structural relaxations use was made of a tolerance for convergence corresponding to a maximum force component on any atom of 2 meV/Å.

4.3 Results

4.3.1 Core Structure Under Applied Stress

I began by applying a series of strains to the supercells containing dislocation quadrupoles. These applied strains were chosen to induce tensile and compressive stresses of $\pm\{1,2,3\}$ GPa along each of the [0001], [1$\bar{1}$00], and [11$\bar{2}$0] axes (x, y, and z in the supercell) in turn. Second- and third-order elastic constants[75] of pure, undeformed hcp titanium were used to compute the required homogeneous strains due to the large stresses targeted. The supercells were relaxed in DFT, and the resulting core structures visualized using differential displacement maps[6] as well as the screw component of the Nye tensor (α_{screw})[64]. One relaxed core for each applied stress on the x- and y-axes is shown in Figure 4.1. Stresses applied on the z-axis were not found to induce any change in dislocation core structure.

Under zero stress the ground-state core is spread along a $\{1\bar{1}01\}$ pyramidal plane, as discussed in Chapter 3. Under all applied stresses considered, the principal direction of dislocation core spread remains along this same axis. However, the degree of spreading of the dislocation core along the [0001] axis varies significantly with applied stress. With positive (tensile) stress applied along the x-axis, the core constricts noticeably and is spread nearly exclusively on a pyramidal plane. With negative (compressive) stress on the x-axis, the pyramidal component remains but significant spread is also added from the ends of the pyramidal section, extending in the [0001] direction. This creates a core that has both pyramidal and prism components. This trend is reversed for stress applied along the y-axis, as one would expect from the Poisson effect. In fact, the change in core structure is larger for the same magnitude of stress when it is applied along the y-axis.

The larger change in core structure when stress is applied on the y-axis is more apparent in the Nye tensor distribution than in the arrow plot. To more clearly illustrate the difference, Figure 4.2 plots the difference in Nye tensor screw components between the highest tensile stress on the y-axis and highest compressive stress on the x-axis. This shows that the core under tension on the y-axis has considerably more of its Burgers vector content in the periphery of the core rather than in the center. While the total area over which the two cores are spread is similar, the core is more evenly distributed with tension along the y-axis. As will be shown in the next section, it is much easier for the dislocation to glide under tension on the y-axis than under no applied non-Schmid stress, and this is likely related to this increase in ground-state spreading.

4.3.2 Dislocation Mobility Under Applied Stress

The energy barriers to dislocation slip on the prismatic plane under each of the stresses on the x- and y-axes discussed above were calculated using the NEB method with 5 images. Plots of energy vs. reaction coordinate are shown for three example NEB calculations in Figure 4.3. A summary of these results is shown in Figure 4.4. While stress applied on the x-axis had a marked effect on the core structure as represented by the Vitek arrow plots, the change in the barrier to slip on the prismatic plane across the stress range is relatively small. On the other hand, the change in energy barrier when stress is applied on the y-axis is considerable. Under 3 GPa tension along the y-axis, the barrier of 8.5 meV/b is less than
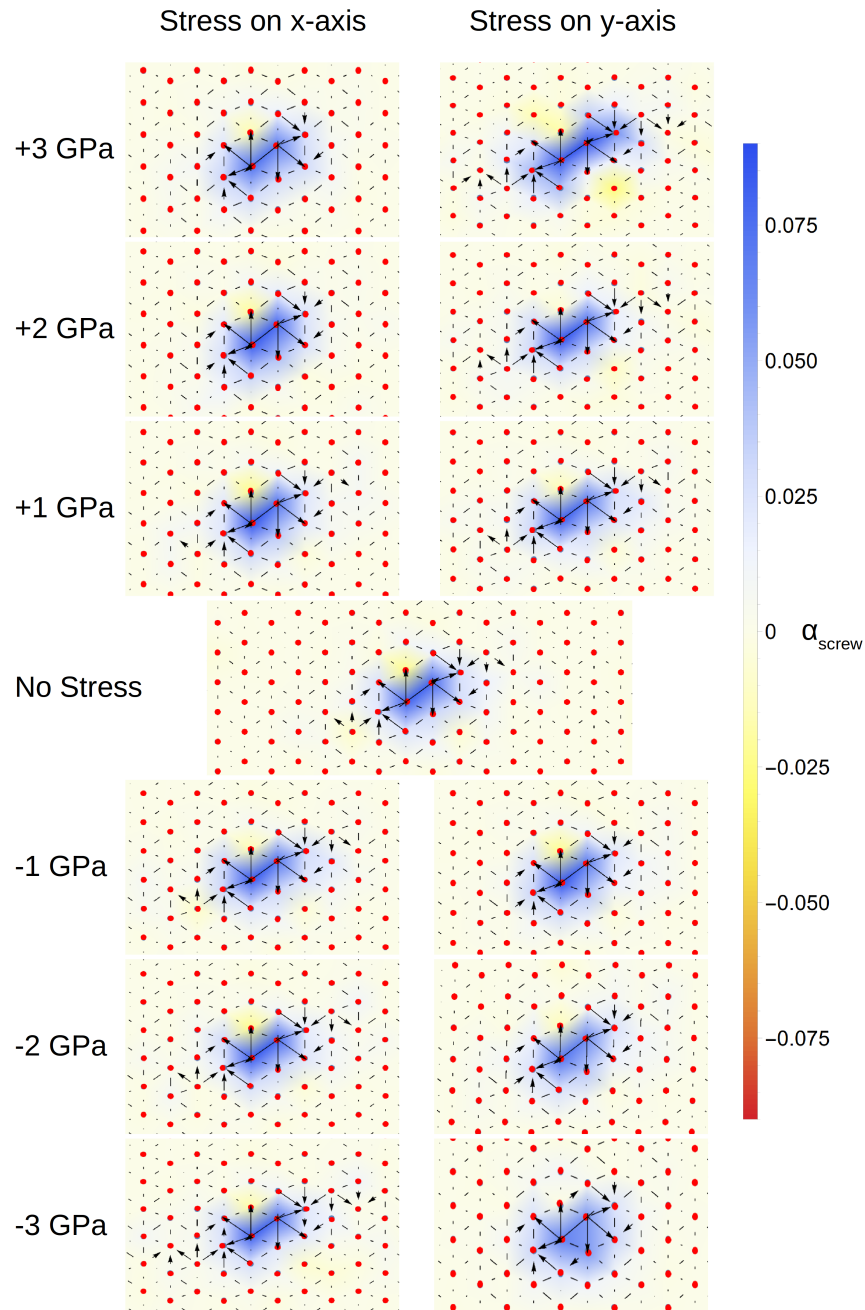
Figure 4.1: Relaxed ⟨a⟩-type screw dislocation cores structures for a series of stresses on the x [0001] (left) and y [1$\bar{1}$00] (right) axes of the supercell. The color distribution is the screw component of the Nye tensor, the arrows are Vitek arrows, and points represent positions of columns of atoms in the reference state without dislocation (blue) and with the dislocation (red).

one third of the 30.6 meV/b barrier under zero stress, while the barrier rises to 41.1 meV/b under 3 GPa of compression along the same axis.

Figure 4.2: Difference in Nye tensor screw components between +3 GPa on y-axis and -3 GPa on x-axis (i.e. $\alpha_{screw}^{y+3} - \alpha_{screw}^{x-3}$). Vitek arrows are shown for the core with -3 GPa stress applied on the x-axis to assist in locating the dislocation core center.
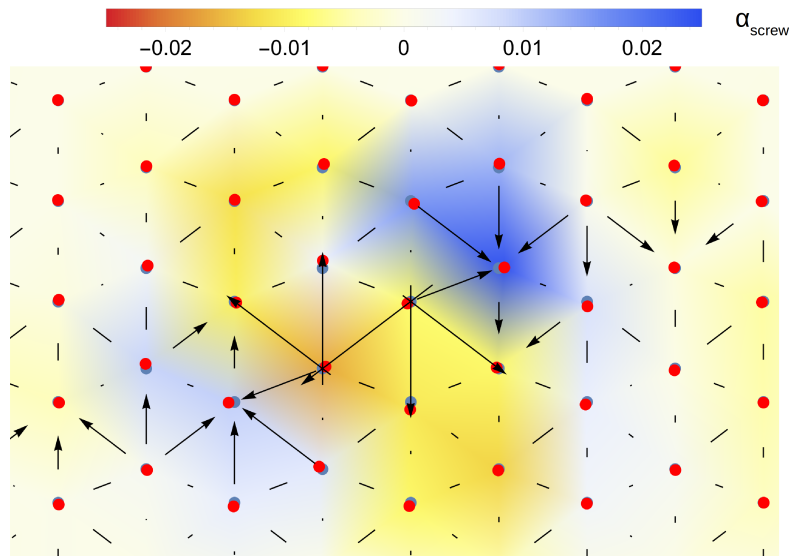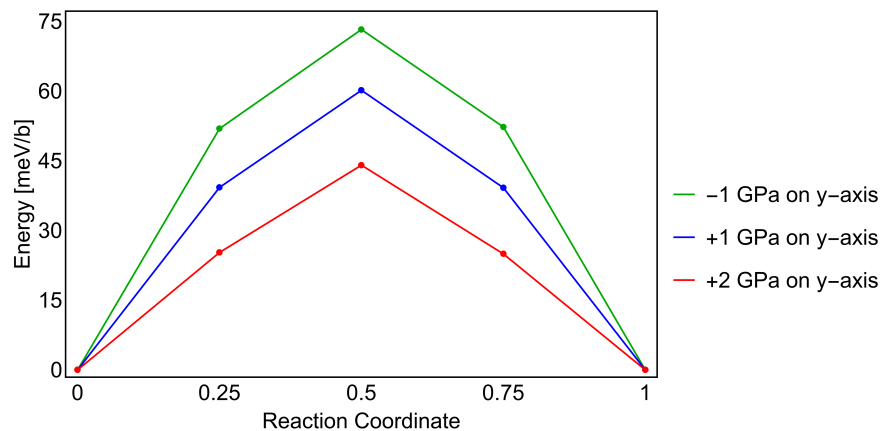

Figure 4.3: Energy vs. reaction coordinate for NEB calculations of $\langle a \rangle$-type screw dislocation slip on the $\{1\bar{1}00\}$ prismatic plane under three applied stresses on the y-axes.

4.4 MEAM Calculations

In Chapter 3 the ground-state configuration of $\langle a \rangle$-type screw dislocations in the MEAM potential was calculated, and was found to be prismatic. While this is not in agreement with my DFT calculations, it is interesting to test if the response of the MEAM potential to non-Schmid stresses parallels that in DFT. Accordingly, calculation of the ground state core structure in the same range of applied stresses on the $[1\bar{1}00]$ axis as for the DFT potential (up to 3 GPa in tension and compression) was performed. The results are plotted and contrasted with DFT results in Figure 4.5.
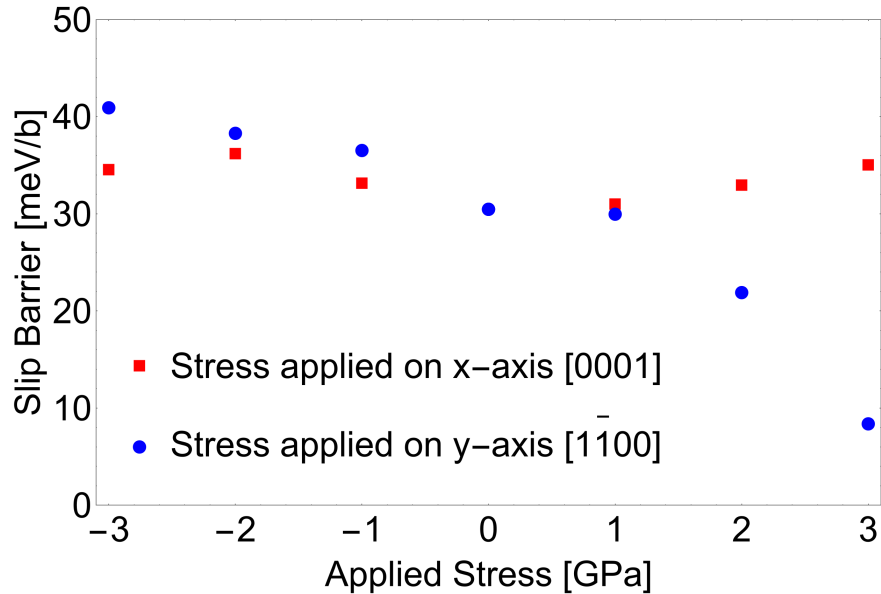
Figure 4.4: Energy barrier to $\langle a \rangle$-type screw dislocation slip on the $\{1\bar{1}00\}$ prismatic plane under applied stress on the x- and y-axes.

Interestingly, the effects of non-Schmid stresses on the ground state core structure are larger for the MEAM potential than for the DFT. Under tension the core becomes very extended along the prism plane with no significant components on other planes. Under compression, on the other hand, the core structure comes to resemble the DFT core quite closely, falling somewhere between the no stress and 3 GPa compression ground state core structures calculated by DFT. Using the NEB method to measure the barrier to prism slip under applied stress on the $[1\bar{1}00]$ axis, I find it is 2.0 meV/b under 1 GPa tension, 7.3 meV/b under no stress, and 14.5 meV/b under 1 GPa compression. This shows a strong trend that follows the same pattern as my DFT calculations. More discussion of the effects of stress on dislocation cores in the MEAM potential will be discussed in the next chapter.

4.5 Discussion

Clouet *et al.* argued that prismatic slip of $\langle a \rangle$-type screw dislocations in titanium is accomplished via a rearrangement of the dislocation core from its ground state pyramidal structure to a prismatic structure[10]. My findings here are consistent with this analysis both under no applied stress and at all applied stresses considered. In each NEB calculation I find the endpoints have pyramidally-configured dislocation cores, while the center image has chiefly prismatic core structure. An example of a transition core structure is shown in Figure 4.6(a), and the difference in Nye tensor screw components between the relaxed and transition core in Figure 4.6(b). It is in fact the rearrangement between these core structures that accounts for the majority of the energy barrier for slip. Under no applied stress, for example, the energy difference between the pyramidal and prismatic states is 18.4 meV/b[53],
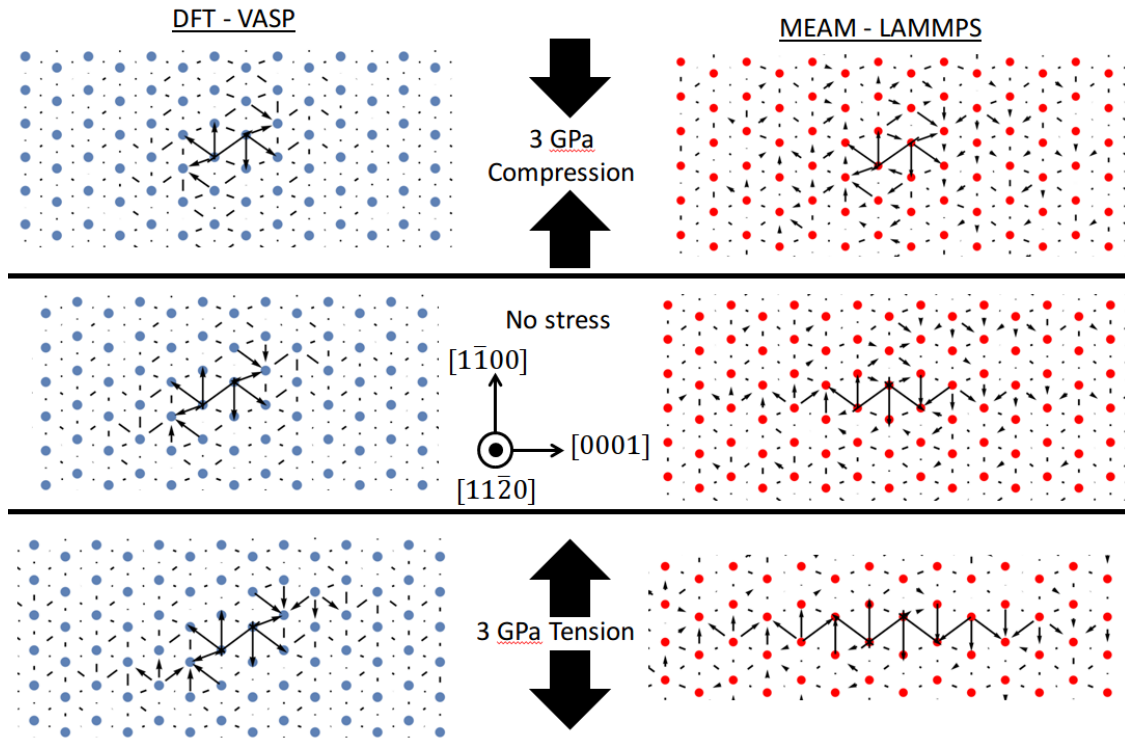
Figure 4.5: Relaxed ⟨a⟩-type screw dislocation cores structures in DFT (left) and MEAM (right) for a series of stresses on the and [$1\bar{1}00$] axes of the supercells. The arrows are Vitek arrows, and points represent positions of columns of atoms.

which accounts for most of the 30.6 meV/b barrier to slip calculated here.

This rearrangement provides the link between the applied stress and the slip barrier. Tension along the y-axis [$1\bar{1}00$] promotes a core structure that is more extended along the prismatic plane and correlates with a reduction in the energy required to convert the core into one that can slip easily along the prismatic plane. Conversely, compression on this axis promotes a more compact pyramidal core structure that provides greater resistance to prismatic reconfiguration and slip.

Consider an experimental tension or compression test on a single-crystal hcp-Ti specimen oriented to favor prismatic slip, i.e., with the maximum resolved shear stress on the prismatic plane. In this geometry the axis for uniaxial tension or compression is the midway between the [$1\bar{1}00$] and [$11\bar{2}0$] directions in the hcp structure. Tension (compression) along this axis leads an tensile (compressive) component of the stress along the [$1\bar{1}00$] and [$11\bar{2}0$] directions. As described previously, there is a negligible effect on the energy barrier for slip resulting from of tension or compression on the [$11\bar{2}0$] axis. Therefore only the component of this stress resolved on the [$1\bar{1}00$] axis is relevant to core structure rearrangement. My prediction based on the non-Schmid effects on core structure is that uniaxial compression in this direction leads to a larger change in the energy barrier for slip than tension, which matches with experimental observations on high-purity titanium samples where compression far from the [0001] direction leads to the greatest suppression of dislocation slip, and tension along the same axis leads to the lowest yield strength[73]. The same study found that the tensile
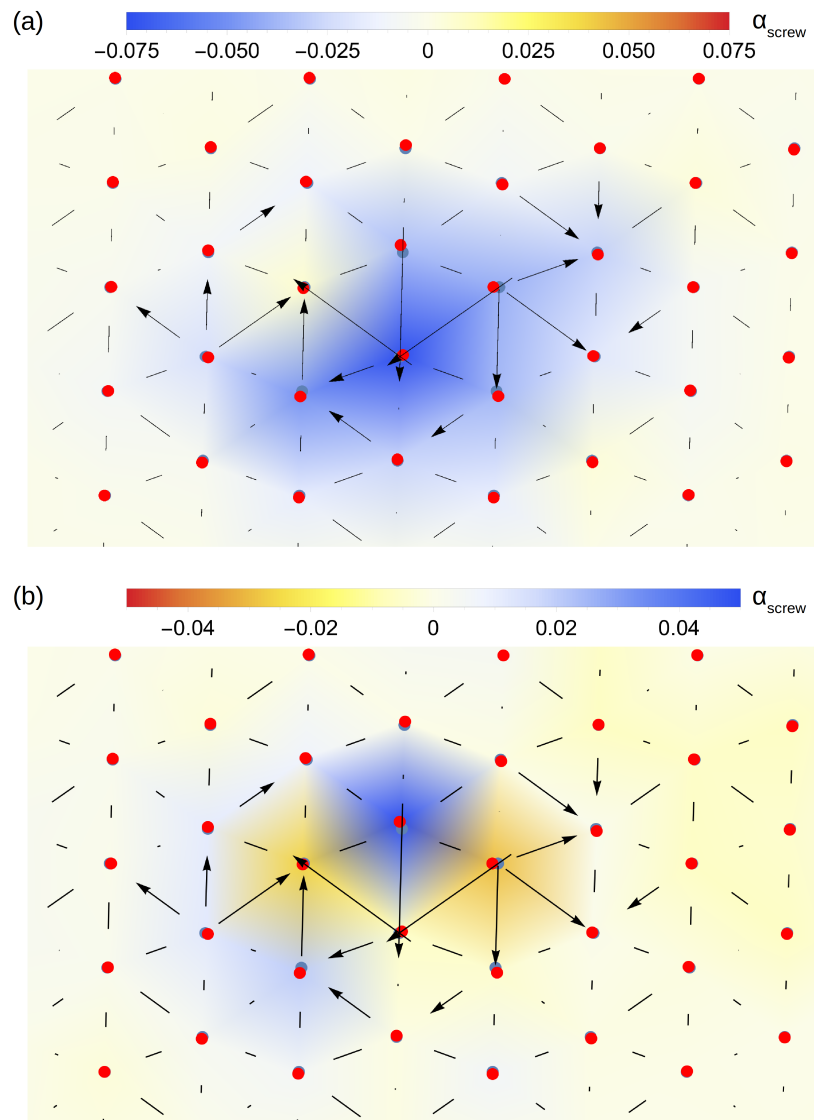
Figure 4.6: (a) Transition-state dislocation core structure for prismatic slip under 2 GPa of compressive stress on the y $[1\bar{1}00]$ axis. (b) Difference in Nye tensor screw components between the transition state core in (a) and the relaxed core under the same applied stress (i.e. $\alpha_{screw}^{transition} - \alpha_{screw}^{relaxed}$). Differential displacements maps are shown for the transition state core to assist in locating the dislocation core center.

direction leading to the highest yield strength (for tension) was the nearest to the $[0001]$ axis of those tested, also in line with the predictions of my calculations. Further, their pole figures demonstrate that grains in samples tested in compression tend to rotate such that the compressive axis becomes aligned along their $[0001]$ axis, further suggesting that plasticity is better-accommodated when compression is far from the $[1\bar{1}00]$ axis. However, these experiments were performed on polygranular samples at much lower stresses than those in my calculations, which limits direct comparison between the two. My calculations agree with the trends observed in these experiments, and suggest a possible cause for these trends.

A related observation from Figure 4.1 is that there does not appear to be a discrete switching between core structures, i.e. pyramidal at zero stress to prismatic at some critical stress. Rather, applying tensile stress on the y-axis causes a smooth extension of the core along a prismatic plane, while considerable pyramidal character remains. In compression on the same axis, the prismatic extension is smoothly reduced and again the pyramidal component remains. Similarly, the transition state cores found in the NEB calculations are not entirely prismatic in nature. Rather than observing a pyramidal to prismatic switching, I see a continuum of cores from "mostly pyramidal" to "mostly prismatic" during slip. Many of these core structures are in fact non-planar, as Sakai and Fine, Naka *et al.*, and Neeraj *et al.* suggested to be the explanation for their observation of non-Schmid slip behavior in α-titanium alloys[70–72].

Non-planar dislocation core structures are understood to be the underlying cause of non-Schmid behavior in bcc metals[76], but those core structures are strikingly more non-planar than observed here. Further, the non-Schmid stresses applied in my DFT calculations are much higher than those in the experimental observations of non-Schmid slip behavior in titanium alloys. However, my calculations suggest that the dislocation core structure in α-titanium can be skewed by non-Schmid stresses. Moreover, there is a continuum of dislocation core structures which can be occupied. Previous calculations of the energies separating the "pure" prismatic and pyramidal stresses in DFT at 0 K put them within tens of meV per Burgers vector of each other[10, 53, 54, 56, 57]. This suggests that $\langle a \rangle$-type screw dislocation cores will occupy different structures according to a thermal distribution at finite temperatures. Applying non-Schmid stresses would thus produce a skew in these distributions, creating non-Schmid slip behavior even at much lower stresses than those applied in my zero-temperature DFT calculations. Additionally, it is possible that the dislocation core structure is more susceptible to applied stress when titanium is alloyed.

4.6 Conclusions

I have performed density functional theory calculations to determine the ground state core structure of $\langle a \rangle$-type screw dislocations in titanium under a range of applied stresses. These calculations indicate that the core structure is altered by applied stresses that have zero resolved shear stress on the dislocation. The core can be made to extend or contract along the prismatic $[1\bar{1}00]$ plane, but always retains a pyramidal component over the range of stresses considered. Nudged elastic band calculations under the same range of stresses show that increased prismatic components are correlated with a lower barrier to slip of the dislocation on the prismatic plane, while contraction into a compact pyramidal core leads to a higher barrier to slip on the prismatic plane. These results corroborate earlier conjecture that the non-Schmid slip behavior of $\langle a \rangle$-type screw dislocations in α-titanium alloys is due to non-planar core structure.

Chapter 5:

Finite Temperature Analysis of ⟨a⟩-Type Screw Dislocation Core Structures

5.1 Introduction

Thus far the discussion of dislocation core structures has focused entirely on relaxed core structures at 0 K, whether considering applied stress or not. While it is no doubt important – not to mention surprisingly complicated – to gain an understanding of the potential energy landscape for dislocation core structures, this does not very well reflect the behavior of dislocations in situations that engineers care about for practical applications. In real engineering applications these dislocations exist at finite temperature. As the differences in energy between different core structure configurations are small (comparable to thermal energies at working temperatures if the intrinsic length scale of the dislocation segment is take to be on the order of the Burgers vector), one would expect thermal occupation of the available states at modest temperatures. However, the free energy of competing dislocation core structures, which governs the equilibrium probability of the dislocation taking on these core structures, is not a topic that has been given much thought.

It seems likely that the dislocation core structure is somewhat correlated spatially. If at a given position on the dislocation line the core is extended prismatically, it is reasonable to expect that two Burgers vectors along the line dislocation line the core structure is likely to be prismatic, and that in fact there might be an energy cost to transitions between regions of differing core structures. If this were the case then applying an Ising-like model[77–79] for the dislocation core structure might be appropriate, particularly if there is a small number of important states.

Besides fitting the core structure data to an existing model (which will have to be work for a future researcher, as I have not done this) there are many other interesting questions that might be answered if one had access to dislocation core structures at different times, temperatures, and stress states. For example, it is theorized that a locking-unlocking mechanism[10] is crucial to the motion of ⟨a⟩-type screw dislocations in titanium. However, this prediction has so far been based solely on TEM observations (which are unable to resolve dislocation core structures for titanium) and zero-temperature DFT calculations. So despite the theory being fundamentally dependent on occasional activation of prismatic core structures by thermal fluctuations of atoms in the dislocation core, there is so far no time- or temperature-dependent atomistic data available to support the hypothesis. Here, I develop a method to measure the dislocation core structure efficiently from MD data, and use it to develop the temperature and stress dependence of dislocation core structure distributions. Further, the lock-unlocking mechanism is demonstrated by showing the correspondence be-

tween prismatic core configurations and slip of the dislocations on the prismatic plane.

5.2 Choice of Core Structure Descriptor

At the outset of this investigation there is a fundamental issue: there is no existing method by which one could acquire sufficient information about dislocation core structures from a simulation to have any semblance of statistically significant data. So far the method for determining the core structure of a segment of dislocation in an atomistic simulation has been to calculate the Nye tensor or differential displacement maps (or both), look at the data, and make a determination. This method is time consuming and requires a great deal of human input and decision making that leaves plenty of room for bias or error in classifying dislocation cores. It is also a very coarse classification method. Human observers of dislocation core structures have tended to sort the structures into a small number of bins, for example in hcp metals most references only discuss basal, prismatic, pyramidal, and something along the lines of asymmetric or mixed[10, 11, 53, 57, 56]. This human classification scheme may in fact be glossing over the significance of core structures that do not fit neatly into one of these bins, or the importance of intermediate core structures.

Automatically characterizing dislocation core structures requires making some definitions. This includes important considerations such as which atoms should be considered to be part of the dislocation core, and how atoms in the core contribute to the characterization of the core. One reasonable set of choices is to allow all atoms to contribute to core structure identification and to weight contributions by a function of the atomic strain. Intuitively this makes sense, because a dislocation core is a highly strained region, and thus the atomic strains in the core should be large compared to the surrounding elastically-strained material. The atomic strain may fall off quickly or slowly as a function of distance from the dislocation core, and measuring the rate at which it does could provide an estimate of the dislocation core size. Moreover, considering more-strained atoms to contribute more to the assessment of the dislocation core orientation matches (and formalizes) the existing practice when identifying core structures by hand.

Previously, two methods for visualizing dislocation core structures were discussed: the Nye tensor and differential displacement maps. These are effectively two choices for the function of strain used. The differential displacement map construction is useful for visualization, but is a bit of an odd beast if one attempts to use it to automate dislocation core identification. At each atom position there are 6 different vectors (for hcp) connecting to the neighboring columns, each with different length and direction. Attempting to make use of these do determine the degree to which an atom contributes to the Burgers vector content is far from straightforward. The Nye tensor on the other hand contains the information required in a relatively straightforward manner. One could take the magnitude of the screw component of this tensor to be the weighting factor used. However, the Nye tensor is not very convenient to compute, and now that the goal is to calculate millions of dislocation core structures, efficiency has become more important. Because the Nye tensor is calculated as the curl of the atomic strain, it requires calculation of the strain of the neighboring atoms to those of interest, which in turn means finding reference-dislocation pairs for the neighbors of the neighbors of the atoms of interest, which is not computationally ideal.

One sometimes-used definition for a dislocation core is that it is the region in which the stress predicted by linear elasticity theory is greater than the ideal strength of the material[80–82]. The intuition behind this is that in this region elasticity theory has broken down and therefore this region is "plastic". This definition is interesting because it suggests that the extent to which an atom is within a dislocation core can be calculated from the strain itself (rather than from a derivative of the strain), eliminating a layer of difficulty of computation compared to the Nye tensor. Following the work of de Jong *et al.*[75], the ideal strength of a material can be accurately estimated if one knows the second and third order elastic constants for the material. This is done by finding the eigenvalues of the symmetrized Wallace tensor[83] ($\boldsymbol{B}$), which is a function of stress (and thus of strain, provided one knows the elastic constants at the given strain state). When an eigenvalue of the symmetrized Wallace tensor goes to zero, the ideal strength has been reached.

Another way of thinking about this is that the nearness to plasticity (i.e. exceeding the ideal strength) can be assessed by calculating the size of the smallest eigenvalue of the symmetrized Wallace tensor. If one has access to atomic strains, this can be done for each atom. This forms the basis for a new method of determining dislocation core structures. For each atom in a simulation a parameter υ is computed:

$$\upsilon_i = \frac{min(eig(\boldsymbol{B}^{ref})) - min(eig(\boldsymbol{B}^i))}{min(eig(\boldsymbol{B}^{ref}))} \tag{5.1}$$

where $\boldsymbol{B}^{ref}$ is the symmetrized Wallace tensor for the reference (undeformed) system, and $\boldsymbol{B}^i$ is the symmetrized Wallace tensor for atom i in the current configuration of an atomistic simulation. Given that $min(eig(\boldsymbol{B}^{ref})) > 0$ for a stable reference configuration and $min(eig(\boldsymbol{B}^{ref})) \geq min(eig(\boldsymbol{B}^i))$, the parameter $\upsilon \geq 0$.

This is an appealing and straightforward parameter to characterize dislocation core spread, but how well does it work in practice? One way to determine this is to compare it with an established dislocation identification method such as the Nye tensor for the same dislocation. One test case that is both simple and important is the representation of the ground-state dislocation cores calculated by DFT. A comparison of these between the existing Nye tensor and differential displacement map visualizations and υ is presented in Figure 5.1, which shows that all methods yield structures that are clearly oriented on the same pyramidal planes.

Another important test case is the performance of this parameter on atomic positions extracted from an MD simulation, because these will have thermal noise. If this parameter is to be used to classify core structures generated by MD simulations, it must be able to tolerate this noise. An example of this is shown in Figure 5.2, for a timestep from an MD simulation at 300 K using the MEAM potential for titanium.

As Figure 5.2 demonstrates, υ represents the core structure as effectively as the Nye tensor screw component, and does so with a lower computational cost. There is also a elegance benefit to using υ rather than $\boldsymbol{\alpha}$: calculation of this parameter makes use of no adjustable parameters, whereas there is an angular cutoff set in Nye tensor calculation that can significantly affect results if chosen poorly.
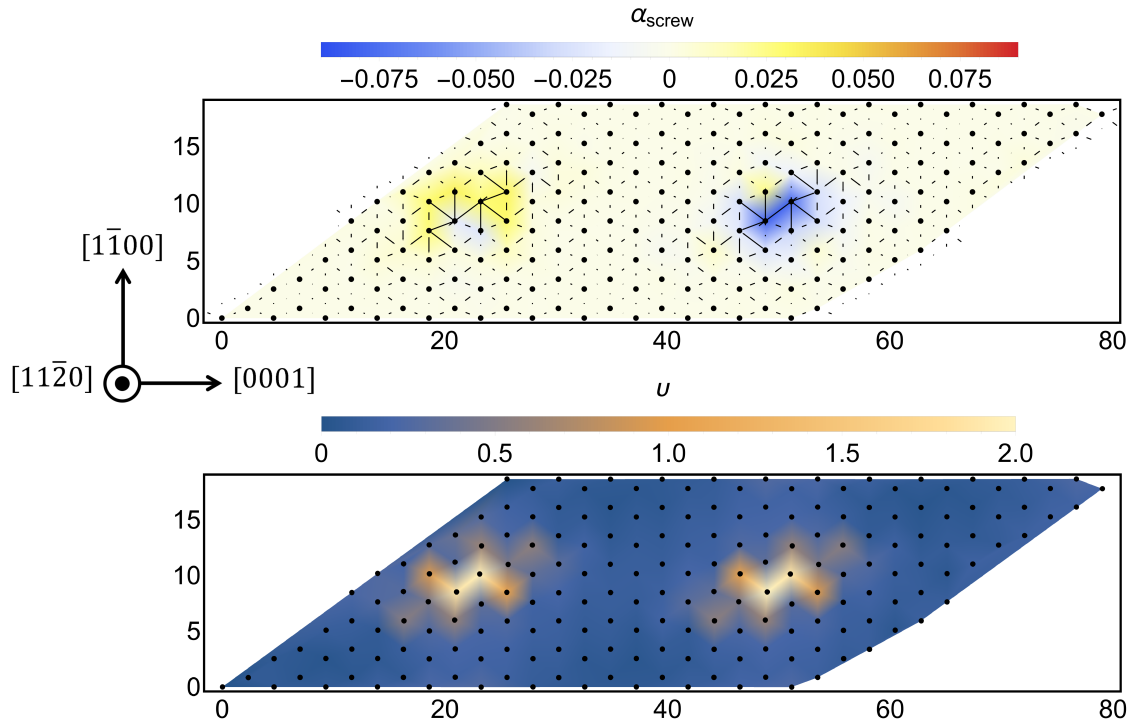
Figure 5.1: Top: Nye tensor screw component and differential displacement map representation of the ground-state dislocation cores for ⟨a⟩-type screw dislocations in titanium calculated by DFT in Chapter 3 of this dissertation. Bottom: New parameter υ representation of the same dislocation cores.

5.3 Fitting the Core Structure Descriptor

Taking υ as the choice for weighting the contribution of each atom to the dislocation core, the next step is to choose a method of extracting the relevant information about the core structure. What information is relevant depends on the system and the researcher, so this method will not be unique. In this case, I am interested in finding the distribution and evolution in space and time of screw dislocation core structures in titanium. From my experience, I know that these tend to be fairly planar and extended along pyramidal and prismatic planes. Therefore in this study the key parameter of interest is the angle the core makes with some fixed plane of interest (I take the basal plane as reference here, which makes the prismatic plane 90° and the first-order pyramidal planes 61.5° and 118.5° for the c/a ratio of the MEAM potential at 0 K). For other problems, completely different features that can be extracted using the υ calculation may be of more interest. For example, in bcc metals the width of the dislocation core is typically of more interest than its orientation, as screw dislocations in bcc metals can spread with 3-fold symmetry but require constriction to become glissile[6].
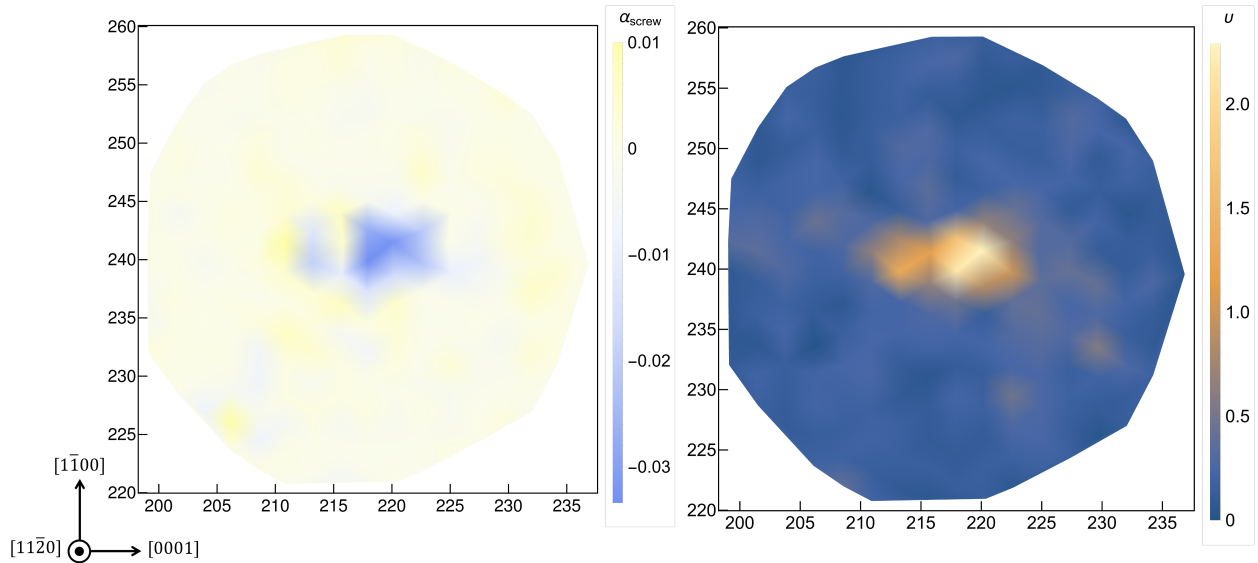
Figure 5.2: Left: Nye tensor screw component representation of the sample dislocation core. Right: New parameter υ representation of the same dislocation core. This example comes from an MD simulation at 300 K using the MEAM potential for titanium. I would like to make it clear that this is no carefully-chosen example case, rather it is the very first core that I had at hand.

To extract the core orientation I fit to a 2-dimensional Gaussian function of the form:

$$\upsilon^{fit}(\xi, \psi) = max(\upsilon) \exp(-((\frac{\cos^2(\theta)}{2\sigma_1^2} + \frac{\sin^2(\theta)}{2\sigma_2^2})(\xi - \xi_0)^2 +$$

$$(\frac{\sin(2\theta)}{2\sigma_1^2} + \frac{\sin(2\theta)}{2\sigma_2^2})(\xi - \xi_0)(\psi - \psi_0) + (\frac{\sin^2(\theta)}{2\sigma_1^2} + \frac{\cos^2(\theta)}{2\sigma_2^2})(\psi - \psi_0)^2))$$

(5.2)

where ξ and ψ are the components of position projected onto the plane normal to the dislocation line direction, $\{\xi_0, \psi_0\}$ is the center of the dislocation, θ is the dislocation orientation angle relative to the basal plane, and σ_1 and σ_2 are the magnitudes of the major and minor axes. These allow for definition of the eccentricity of the core (i.e. a characterization of how planar the core structure is) $\mathcal{E} = \frac{\sigma_1}{\sigma_2}$. Viewed as a contour plot (as in Figure 5.3) the result looks elliptical.

For this example core, θ is found to be 90.97°, indicating that it is almost exactly aligned along the prismatic plane. $\mathcal{E}$ is 2.20, indicating a definite extension of the core along this plane. Both of these findings match with what I would have determined visually from the Nye tensor shown in Figure 5.2.

5.4 Application to $\langle a \rangle$-Type Screw Dislocation Cores in MD

As discussed previously in this dissertation, the MEAM potential for titanium that I have been using predicts a prismatic core structure as the ground state for $\langle a \rangle$-type screw dislocations, which does not agree with DFT calculations (in which a pyramidal core structure is predicted). However, it is also known that there are strong effects of stresses with no
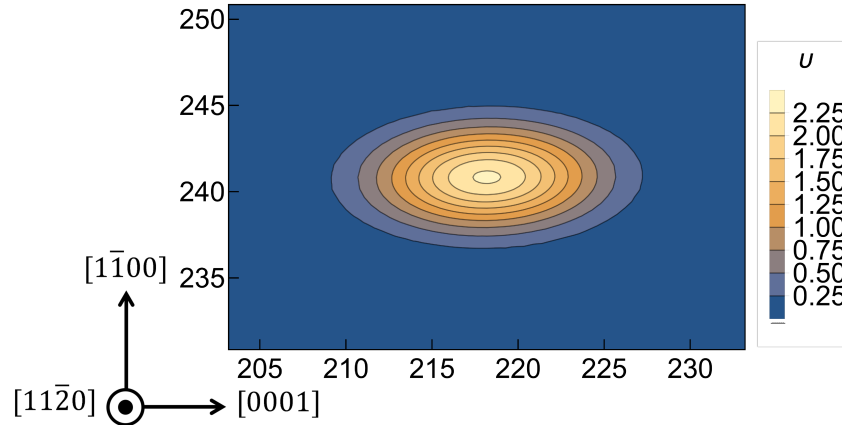
Figure 5.3: Fit of Equation 5.2 to the parameter υ calculated for the same dislocation core shown in Figure 5.2.

resolved shear stress for prism slip on $\langle a \rangle$-type screw dislocations in the MEAM potential when stress is applied along the $[1\bar{1}00]$ axis. In fact, I showed that this non-Schmid stress can induce a transformation of the dislocation core structure from prismatic to pyramidal. Some interesting aspects of this can now be studied using the approach outlined above. For example, what is the transition pressure between these structures? Does temperature change the transition pressure? How does the distribution of core structures behave as it approaches the transition? Is one core structure favored at higher temperatures? What are the correlation lengths and times between different core orientations?

To address these questions, a series of MD simulations using a supercell with dimensions 300 Å × 325 Å on its face and 94 Å along the dislocation line (i.e. 32 Burgers vectors deep) containing two dislocations arranged in the S configuration[9] (described in Chapter 3) were performed. In these simulations the temperature is in the range 100 K to 500 K, and the non-Schmid stress on the $[1\bar{1}00]$ axis is in the range 0 to 1 GPa. Each simulation made use of an NσT ensemble with a Langevin thermostat and Parrinello-Rahman barostat[47], and is run for 100 ps using 1 fs timesteps. The atomic positions were saved every 1 ps, and these were used to generate the dislocation core orientation data. To accelerate data collection, DXA[84] in OVITO[85] is employed to locate the centers of the dislocations, and υ is only calculated for atoms near to these centers. υ is calculated for every slice of the supercell (each slice is 1 Burgers vector thick, the minimum repeat length along the dislocation line direction) at each saved timestep, and thus there are 6400 core orientations calculated for each simulation. Unfortunately, not every calculation yields reliable data. The eccentricity $\mathcal{E}$ is used to filter the data set used for further analysis. Orientations corresponding to cores with $1.25 \geq \mathcal{E} \geq 4.00$ were used for the analysis, and those outside of that range were discarded. This is based on a heuristic analysis that eccentricities outside of that range typically correspond to failed convergence of the fit in Equation 5.2. It also naturally makes sense that when $\mathcal{E}$ is close to 1 the orientation is not significant, since the core is roughly circular. However, some of the small-$\mathcal{E}$ states may correspond to kink structures or other compact transitional cores. More work is required to identify any such cases and include them in the future automated analyses. In the simulations presented here, this typically

removes 10-15% of the total data. Figure 5.4 shows an example distribution of $\mathcal{E}$ for a simulation at 300 K and no applied stress.
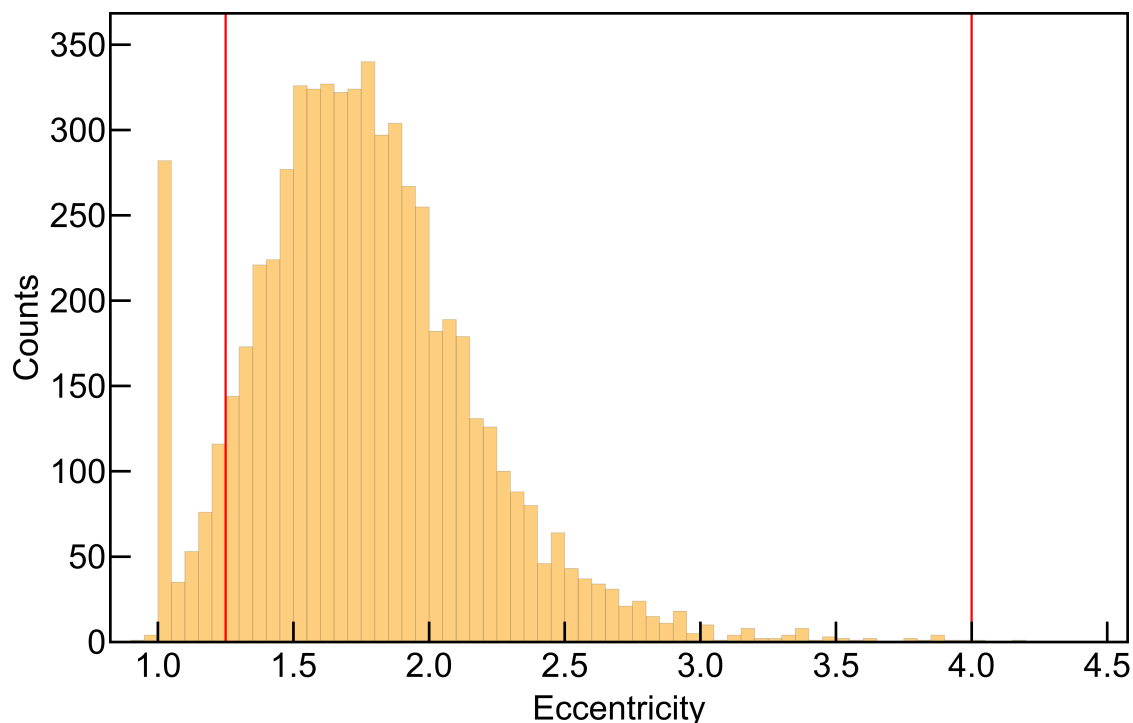

Figure 5.4: Core structure eccentricities of all slices of both dislocations in an MD simulation at 300 K. The lines show the cutoffs core eccentricities included in the following analysis.

One issue that can arise with the development of a new method such as this is visualization of the resulting data. In the present case visualization is complicated because the interest is in the variation of the orientation of dislocation cores in space as well as time. A comprehensive method for visualizing this information is presented in Figure 5.5.

This method represents all the available core orientation data in both space and time for one dislocation in a simulation, and is somewhat informative to look at. For the example in Figure 5.5, one can quickly glean that orientations are centered on the prismatic plane (90°, black line) overall, but at many timesteps the structure tends to lean towards one or the other of the pyramidal planes (61.5° and 118.5°, red lines). Unfortunately, this method is somewhat overwhelming to view, and many of the data points are obscured by others. A similar but simplified modification is shown in Figure 5.6. In this version, only the median orientation at each timestep is shown as a point, and a line plots the range of the lower and upper orientation quartiles. Use of quartiles is preferable to standard deviation because the deviations from the midpoint often tend to be asymmetric. In this visualization it is easy to follow the shifting of the overall structure along the line over time, as well as to see the variation from the midpoint at each step. Figure 5.6 makes it clear that while sometimes the cores in a timestep are centered on the prismatic plane, at most times the center is actually a state that lies between the prismatic and ideal pyramidal configurations. States falling between have not been given a lot of consideration up to this point, but now they begin to look important.
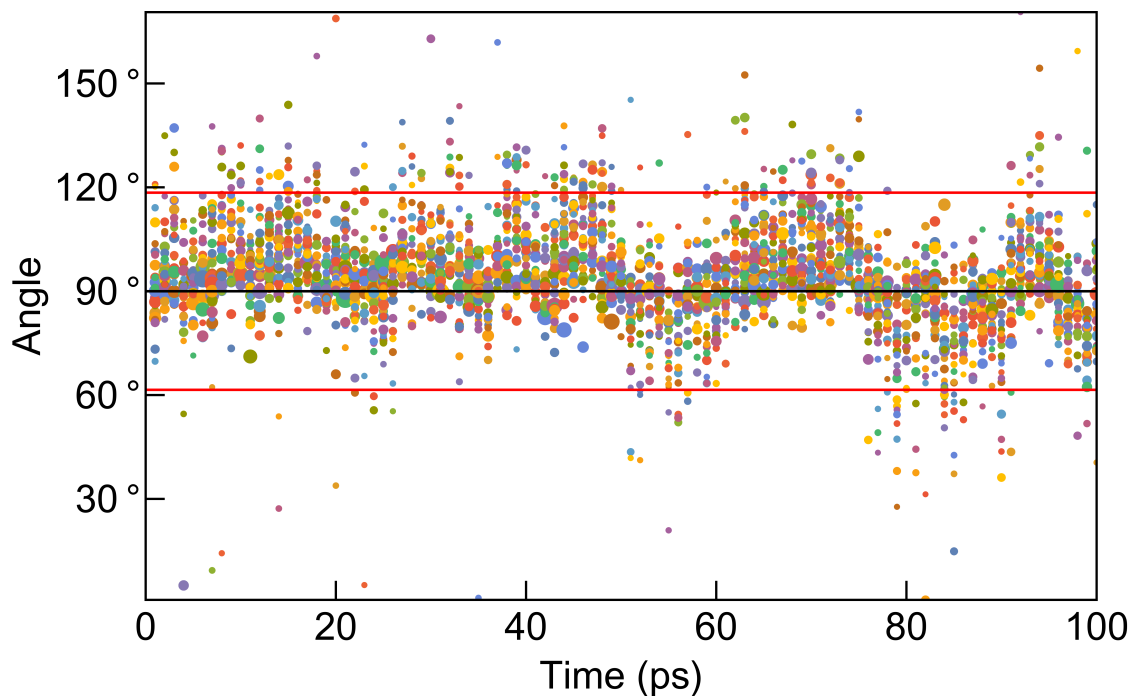
Figure 5.5: Core structure orientation of all slices of one dislocation in an MD simulation at 300 K. Each segment parallel to the y-axis represents one timestep, and the points within a timestep are the orientations of every slice (1 Burgers vector in thickness) along the dislocation line. The size of each point is scaled by the value of $\mathcal{E}$ for that core. The black line shows the position of the prismatic orientation and the red lines are the pyramidal orientations. The colors of the points are varied to assist in distinguishing points.

Another useful visualization method is to throw out the time and position data altogether and simply look at a histogram of the orientations. This is shown for the example case at 300 K in Figure 5.7. This gives a good perspective on the data as a set, for example it makes the prismatic centering of the data more clear than in the previous images. It is worth pointing out that there is no difference between the two dislocations in the simulation (apart from the sign of their Burgers vectors), and therefore they are sampling the same distribution. Given enough time, the blue and yellow distributions would fully overlap.

5.4.1 Effects of Temperature

The visualization methods of Figures 5.6 and 5.7 will be the focus of the following discussion. Now, I will turn to some interesting features that can be investigated using these new developments. Starting with something straightforward, I will examine the change in the core structure distributions as a function of temperature. Simulations at 100 K, 300 K, 400 K, and 500 K under no applied stress were each conducted for 100 ps, and the results are summarized in Figure 5.8.

Clearly as the temperature increases the width of the dislocation core orientation distributions increases significantly. At 100 K virtually all cores are prismatically-oriented, with few outliers further than 10° from the prismatic orientation. At 500 K almost all possible
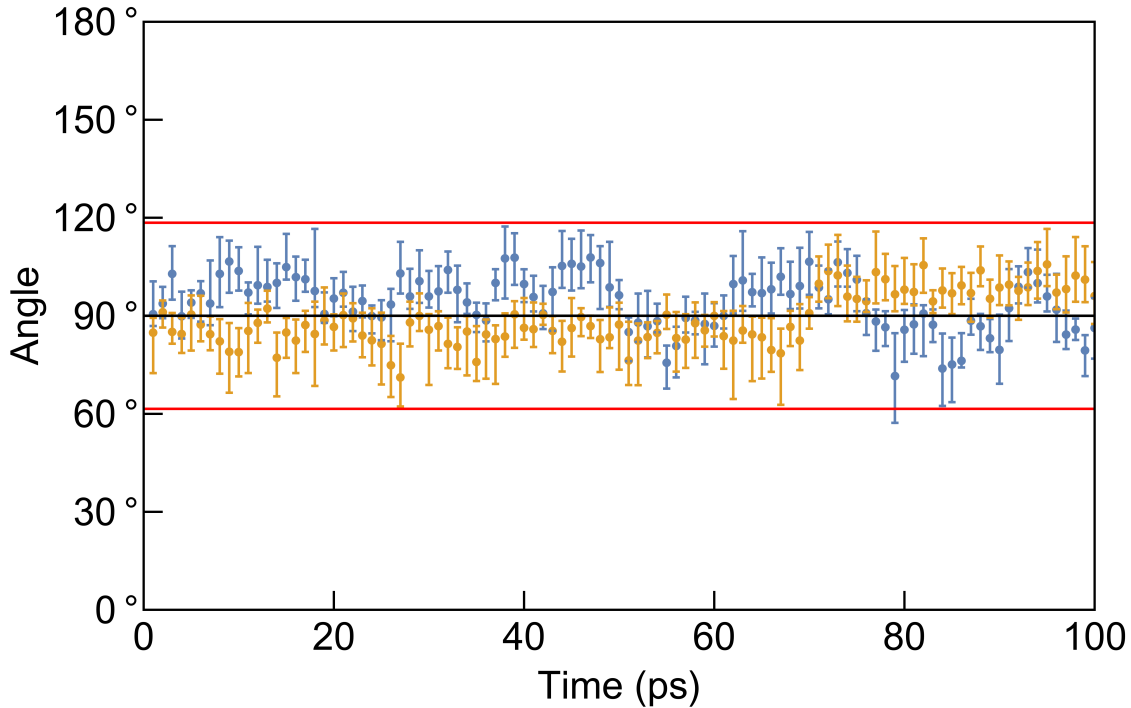
Figure 5.6: Simplified presentation using quartiles and median for core structure orientation of all slices of both dislocations in the same MD simulation at 300 K as shown in Figure 5.5. Each segment parallel to the y-axis represents one timestep. The black line shows the position of the prismatic orientation and the red lines are the pyramidal orientations. The blue data corresponds to the dislocation shown in Figure 5.5, while the orange is the dislocation that was left out in that plot.

core orientations have at least some representation, and at most timesteps even the median core orientation is at least 10° from prismatic. The increase in the spread of the core orientations within each timestep is also significant. At higher temperatures we find dislocations ranging from prismatic to pyramidal on the same dislocation at the same instant frequently. Another observation is that at higher temperatures the overall orientation of the dislocation changes much more rapidly, i.e. the median core orientation for a dislocation changes from pyramidal to prismatic to the other pyramidal regularly. At 100 K there are none of these changes observed.

These behaviors at elevated temperatures largely match expectations. Slightly surprising is that the "pyramidal" structure does not seem to correspond to the ideal pyramidal plane angles (the red lines in the figures), but ultimately this is not shocking. Nye tensor and differential displacement map plots shown in Chapter 3 were never extended precisely along the pyramidal plane. Returning to the data plotted in Figure 5.1 and applying the fit of Equation 5.2, I find that in fact they also fall between the prismatic plane and the ideal pyramidal plane (the pyramidal core from DFT calculations was found to be oriented at 69°). This is one lesson that can be learned from removing the human element of classification and instead looking at algorithmically generated data. Accepting that orientations around 70° and 110° match those that have previously referred to as pyramidal, occupation
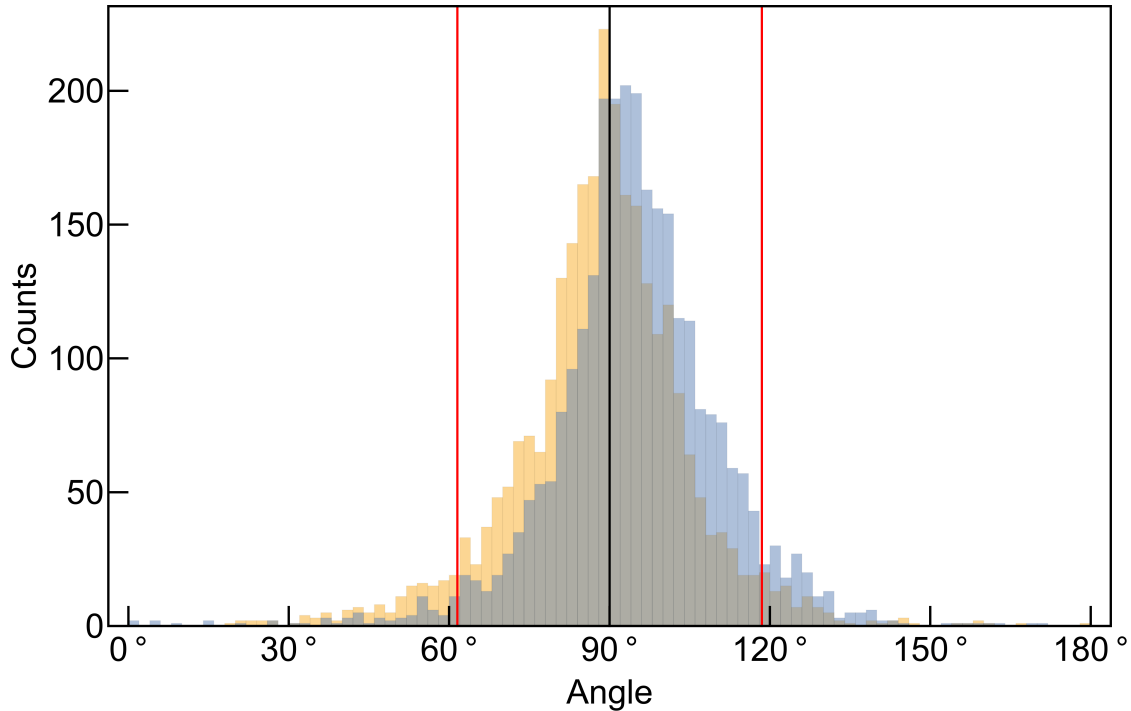
Figure 5.7: Histogram of all core structure orientations slices for both dislocations in the same MD simulation at 300 K as shown in Figure 5.6. The black line shows the position of the prismatic orientation and the red lines are the pyramidal orientations.

of these states is not surprising. The prismatic orientation is the ground state with no applied stress and the pyramidal orientation is accessible within thermal energies (recall the 9 meV/b potential energy difference I calculated in Chapter 3). It follows that increasing the temperature would allow for significant occupation of the pyramidal structure.

The histograms resulting from higher-temperature simulations indicate that the occupations of orientations varies somewhat smoothly. This is mildly surprising, since up to this point the discussion has revolved around a finite number of possible core structures rather than a continuous distribution of structures. Physically, though, this makes sense. Intermediate core structures are necessary for transitions between primary structures (i.e. prismatic, pyramidal, basal) to occur. Moreover, thermal fluctuations induce variation about a local equilibrium structure, as can be seen in the 100 K distributions which certainly do not sample any local basins of attraction other than the prismatic core structure. Given the low potential energy differences between the core structures discussed previously, it is not surprising to conclude that the potential energy landscape is relatively flat and that this leads to the smooth orientation distributions.

5.4.2 Effects of Non-Schmid Stress

On the subject of the various core structures found in earlier optimization calculations, I showed in Chapter 4 that by applying stresses with zero resolved shear stress the ground-state core structure of ⟨a⟩-type screw dislocations in the MEAM potential can be changed.

Figure 5.8: Core orientations (left) and histograms (right) of all core structure orientations slices for both dislocations in MD simulation at 100 K, 300 K, 400 K, and 500 K (top to bottom) under no applied stress. The black line shows the position of the prismatic orientation and the red lines are the pyramidal orientations.

More specifically, I showed that when a large compressive stress is applied on the [1$\bar{1}$00] axis

the equilibrium core structure changes from prismatic to pyramidal. The v parametrization can be used to investigate the pressure at which this transition occurs. I began investigation into this by performing a series of simulations with different applied stresses on the $[1\bar{1}00]$ axis, all at 100 K. This temperature was chosen because Figure 5.8 indicates that there will be minimal spread of the orientations due to thermal fluctuations, and thus it will be simple to assess which core structure is favored. The results of these simulations are summarized in Figure 5.9.

As discussed previously, the core structure under no applied stress is purely prismatic with very little deviation. With 125 MPa compression applied on the $[1\bar{1}00]$ axis, evidence of a small number of excursions toward pyramidal core structures can be observed. Further increasing the compression to 200 MPa, the dislocations spend approximately equal time in prismatic and pyramidal orientations. This, roughly speaking, is the transition pressure at 100 K. It is clear that the transition from one core structure to the other is not sharp (in this supercell), which makes determining the pressure at which it occurs inexact. In the histogram from the 200 MPa, 100 K, simulation one can see the appearance of shoulders, indicating that in this case the pyramidal orientations are occupied to a greater extent than simply as variations about the prismatic orientation. Further increasing the compression to 500 MPa results in only pyramidal core structures. With this simulation I was somewhat fortunate that the two dislocations happened to occupy opposite pyramidal orientation – as mentioned before, the dislocations sample the same distribution so there is no reason to expect this. This results in a lovely histogram that neatly shows the orientations of the two pyramidal structures occupied at this temperature and pressure. At the highest compressive stress simulated (1 GPa), the dislocations happened to select the same pyramidal plane and not transition to any other structures, and thus the distributions overlap. If one compares the histograms resulting from the 500 MPa and 1 GPa simulations quite carefully, it can be observed that the peaks of in the distributions are actually slightly different. With 500 MPa compression applied the lower-angle pyramidal orientation peak is at 71.5°, while under 1 GPa it is at 68.0°, which is closer to the ideal pyramidal orientation (and very similar to the orientation calculated for the DFT ground-state). I did not plot the distribution corresponding to an applied compression of 250 MPa, but this condition results in pyramidal cores peaked at 74.6°, which continues this trend. These are substantial differences in core orientations, and the trend implies that the effect of non-Schmid stresses goes beyond selecting the degree to which the prismatic and pyramidal orientations are occupied: in fact, they also influence the preferred configuration of pyramidal core structures.

Given the significant changes induced by the non-Schmid stresses on the dislocation core structures, one would anticipate strong effects on dislocation slip behavior and thus on plastic deformation. More specifically, in light of the core structure based explanation for the locking-unlocking mechanism proposed by Clouet *et al.*[10], the expected behavior is that under zero non-Schmid stress the dislocations should be able to slip easily on the prismatic plane (known to be the dominant slip plane in titanium), whereas under large non-Schmid stresses that induce the pyramidal core orientation slip should be much more difficult. In other words, it is expected that the dislocation cores will be unlocked under no applied compression on the $[1\bar{1}00]$ axis, and locked under 500 MPa and 1 GPa compression on the same axis, based on the orientation distributions shown in Figure 5.9. For intermediate
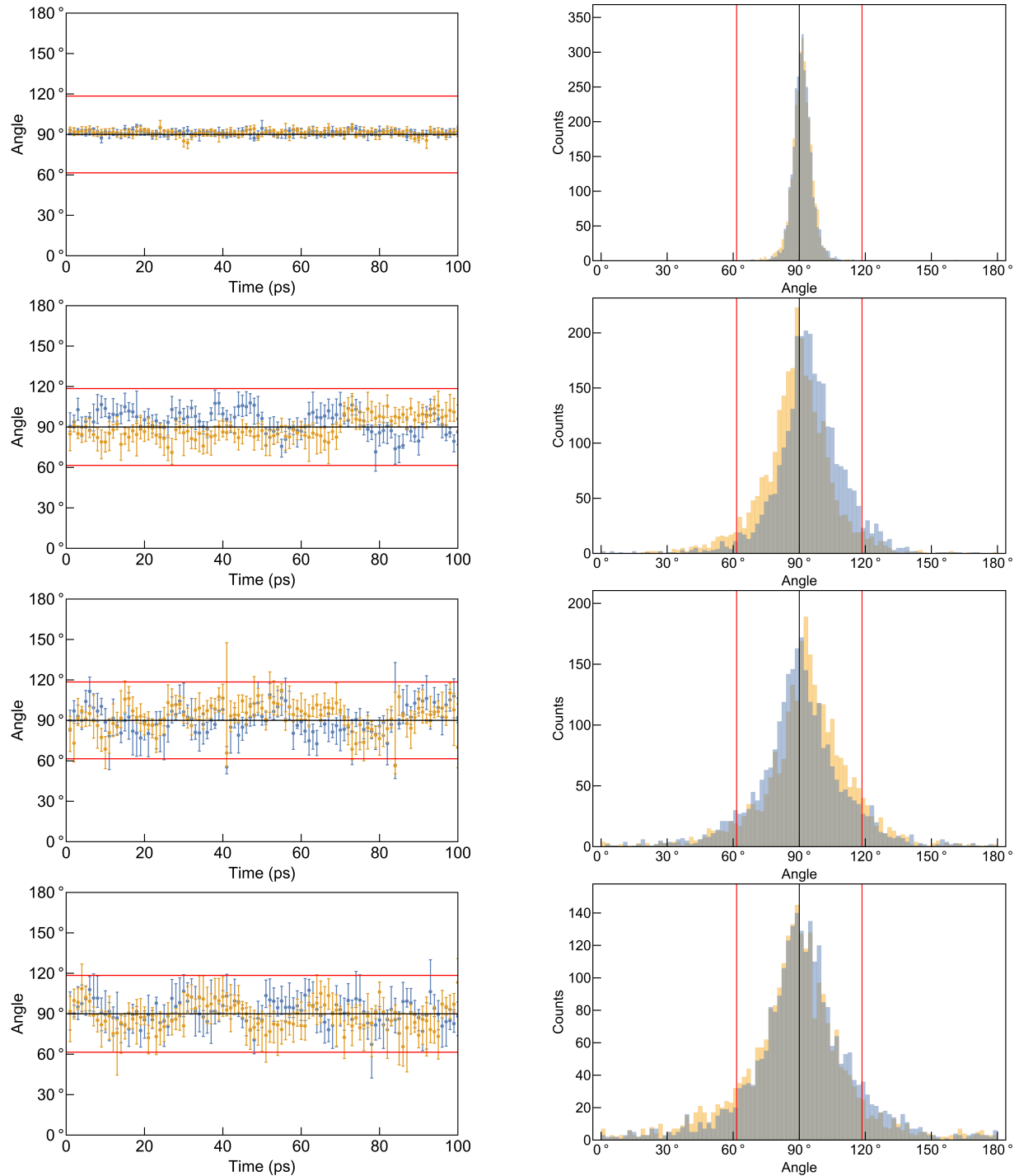
Figure 5.9: Core orientations (left) and histograms (right) of all core structure orientations slices for both dislocations in MD simulation at 0 MPa, 125 MPa, 200 MPa, 500 MPa, and 1 GPa (top to bottom) non-Schmid stress applied on the $[1\bar{1}00]$ axis at 100 K. The black line shows the position of the prismatic orientation and the red lines are the pyramidal orientations.

stresses for which both prismatic and pyramidal cores are represented I expect some slip to occur, but less than for the totally unlocked state. To investigate these predictions, I

performed simulations very similar to the previous set described above, but with a shear stress of 200 MPa oriented with the maximum resolved shear stress on the prismatic plane applied in addition to the non-Schmid stresses. A plot of strain vs time for simulations with 0 MPa, 200 MPa, 500 MPa, and 1 GPa non-Schmid stress applied at 100 K is shown in Figure 5.10.
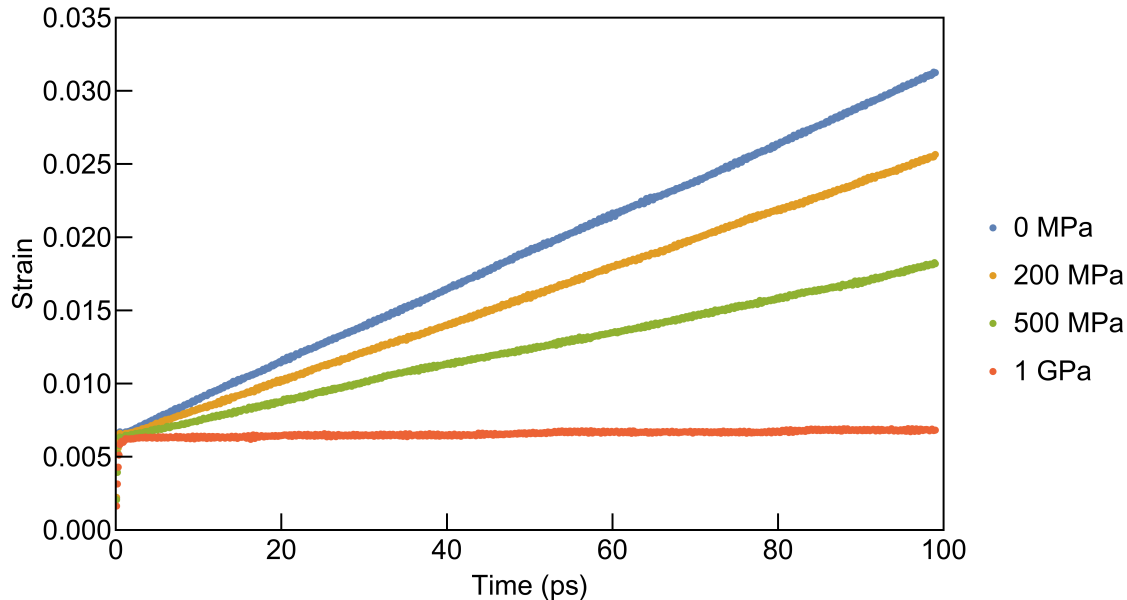
Figure 5.10: Shear strain vs time for MD simulations with 200 MPa shear stress for prismatic slip and 0 MPa, 200 MPa, 500 MPa, and 1 GPa non-Schmid compression along the $[1\bar{1}00]$ axis applied at 100 K.

Examining the strain data in Figure 5.10, it is evident that my predictions largely held true. Slip occurs readily when no non-Schmid stress is applied – the unlocked configuration – and with increasing compression on the $[1\bar{1}00]$ axis the strain decreases. When 1 GPa compression is applied – the locked configuration – the dislocations hardly slipped at all. At 200 MPa, substantial slip occurred because the prismatic orientation is accessible. The only surprising simulation is that under 500 MPa compression. Under these conditions the core is almost entirely pyramidally oriented when there is no shear applied, so I anticipated little or no prismatic slip to occur. However, it is now clear that this stress is not high enough to make the prismatic orientation inaccessible at 100 K, and thus under applied shear stress the cores were able to transform into the prismatic configuration and accomplish substantial slip. One neat feature of applying this technique is that I can compute the core structure distributions during slip just as simply as at rest, and thus verify that the differences in strain are in fact due to the amount of locking of the dislocation cores. The core structure distributions corresponding to the simulations under shear stress at 100 K are shown in Figure 5.11.

It is clear that the greater the fraction of the dislocation cores that are oriented along the prismatic plane, the greater the degree of prismatic slip. It is also plain that under 500 MPa and 1 GPa compression the dislocation cores still have a strong tendency toward pyramidal orientation, which is what is expected based on the calculations with no shear stress applied.
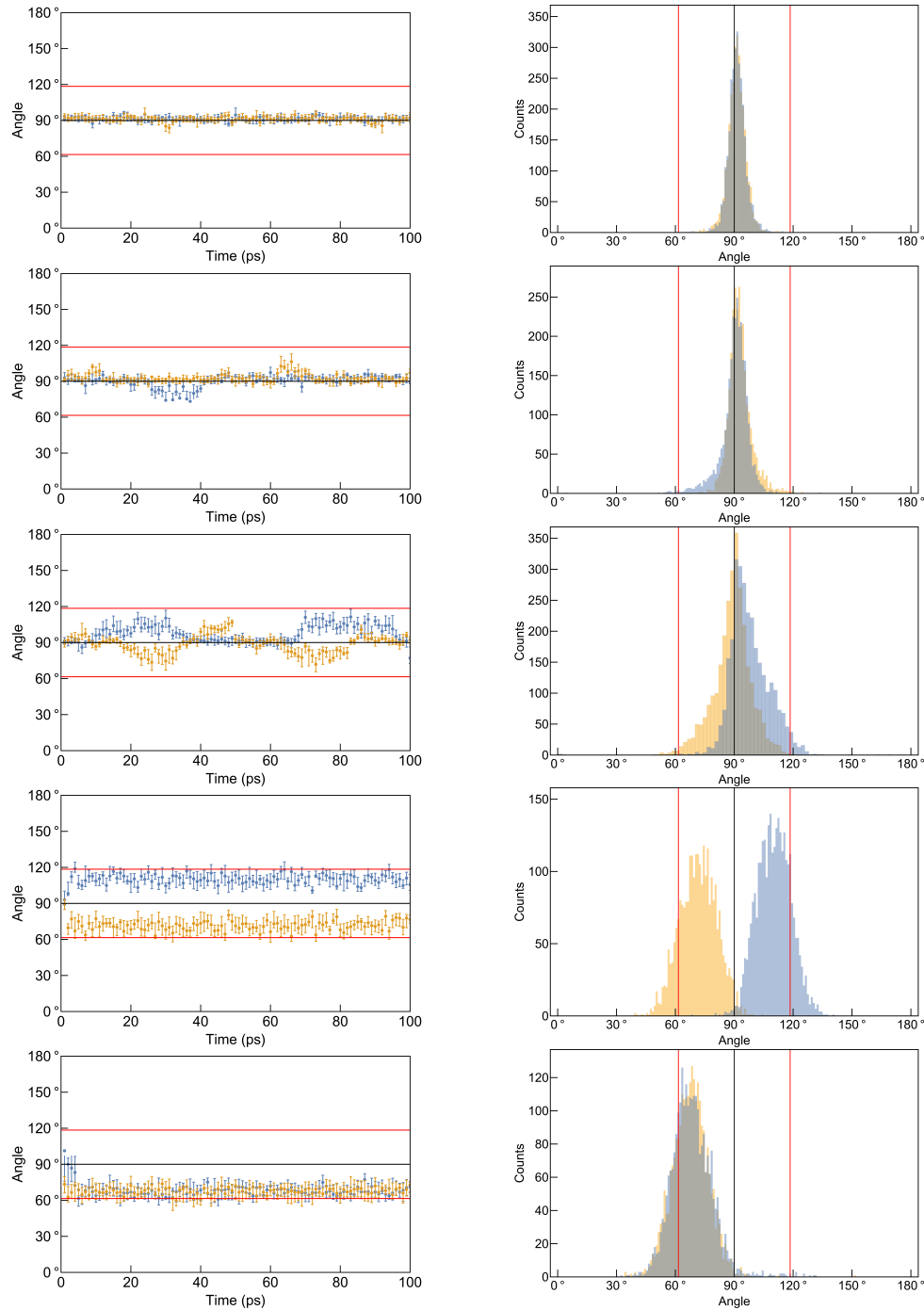
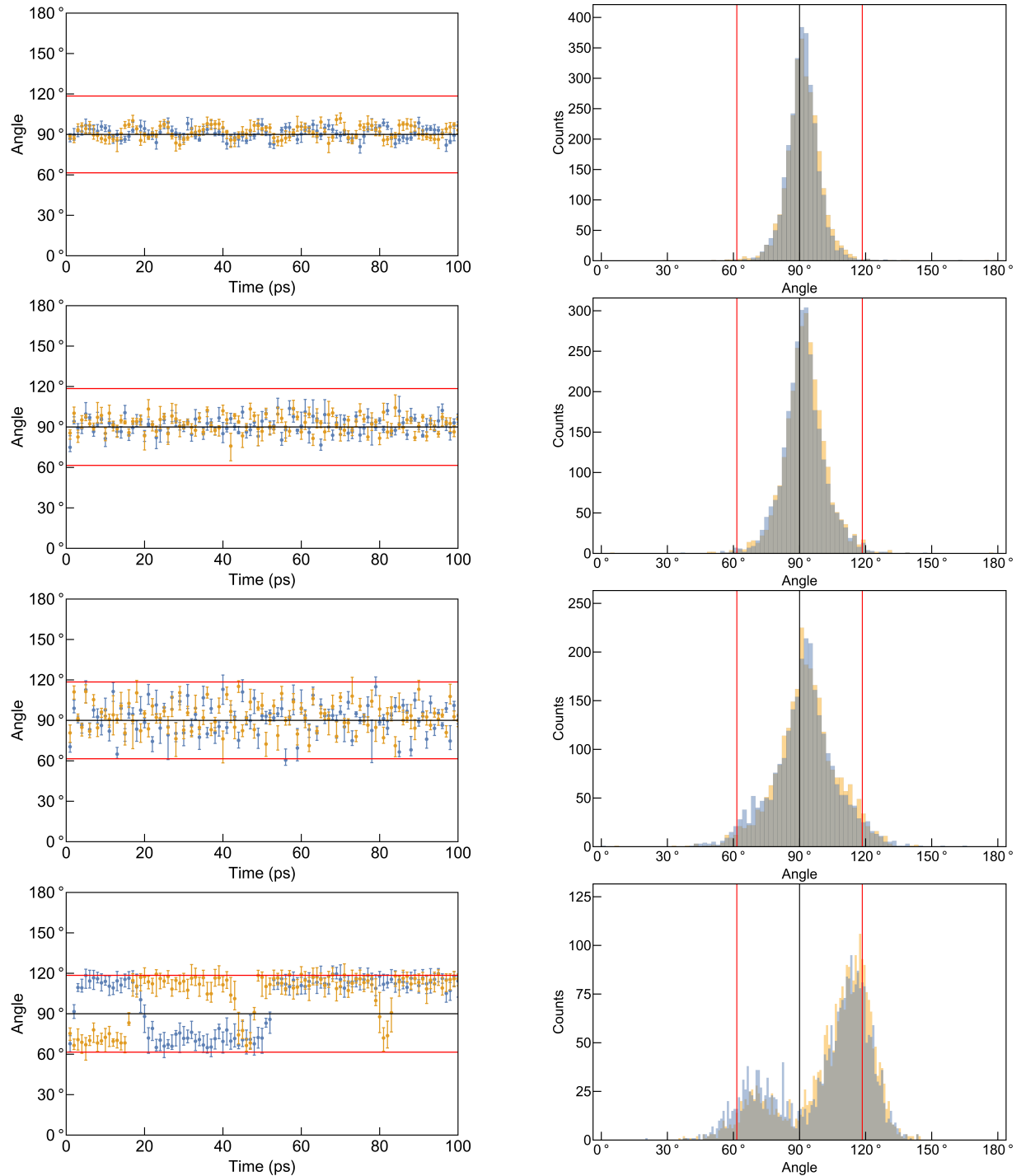**Figure 5.11:** Core orientations (left) and histograms (right) of all core structure orientations slices for both dislocations in MD simulation with 200 MPa shear stress for prismatic slip and 0 MPa, 200 MPa, 500 MPa, and 1 GPa (top to bottom) non-Schmid stress applied on the [1$\bar{1}$00] axis at 100 K. The black line shows the position of the prismatic orientation and the red lines are the pyramidal orientations.

However, the key difference between these two stress states is the accessibility of the prismatic configuration. At 500 MPa the cores can regularly reconfigure to prismatic and slip, as can be seen in the quartile representation which shows frequent switching back and forth across the prismatic line. On the other hand, under 1 GPa compression the prismatic orientation is nearly forbidden. There are only a small handful of slip events observable in Figure 5.10 for this stress state, and each of them corresponds to one of the rare occasions that a dislocation core orientation is prismatic. These unlocking events are short-lived, and the cores rapidly return to one or the other of the pyramidal configurations. This lends strong support to the locking-unlocking hypothesis that was formulated in DFT, as the behavior of the dislocation core structures in MEAM under 1 GPa compression on the $[1\bar{1}00]$ axis matches well with DFT under no applied stress (they show nearly the same ground-state configuration, and have similar energy differences between pyramidal and prismatic configurations).

The existence of the locking-unlocking mechanism due to core structure reorientation can be made more evident by comparing the dislocation core configurations with the positions of the dislocations during the simulation at 1 GPa compression and 200 MPa shear stress at 100 K. The dislocation center positions is a convenient byproduct of using DXA to locate the dislocations as a preprocessing step during calculation of v. This comparison is shown in Figure 5.12, and it is absolutely clear that every single movement of the dislocations along the prismatic plane corresponds to a brief unlocking of the dislocation core structure.

Clearly the locking-unlocking mechanism can explain the behavior under these stress conditions at 100 K. A further prediction of the locking-unlocking theory is that increasing the temperature should promote changes in the dislocation core structure, and thus allow the dislocations to unlock more readily. I test this by performing the same MD simulations again, but now at 300 K. First, I will examine the configurations of the core structures without shear stress applied, to parallel Figure 5.9. This is shown in Figure 5.13.

Examination of Figure 5.13 yields many of the expected observations, as well as a surprising finding. First, the anticipated: for all stress states, the variation in the core orientations is greater at 300 K than at 100 K. This is true both in terms of the widths of the quartiles at each step, and the variation in the median orientations from step to step. This is a straightforward effect of temperature: higher temperature induces broader distributions of the occupied orientations. A related effect is that the dislocations change their overall orientations more frequently. For example, at 100 K and 500 MPa compression the dislocations settled into pyramidal orientations and never changed to prismatic or the other pyramidal. At 300 K and 500 MPa, a number of reorientations can be observed. Given the findings from the simulations under shear stress, this suggests that there should be somewhat more slip at 300 K under the larger compressions than there is at 100 K. This would be in line with previous predictions based on a dislocation core structure explanation for the locking-unlocking mechanism[10].

On the other hand, comparing the simulations with 0 MPa, 125 MPa, and 200 MPa compression at 300 K with the same applied stresses at 100 K, it appears that at higher temperature there is significantly less occupation of prismatic core structures. This is true not just in the sense of greater fluctuation away from these states (which certainly accounts for some of the difference) but also in the locations of the medians. In fact while at 100 K compression of 200 MPa is found to be the transition pressure, at 300 K there are almost no
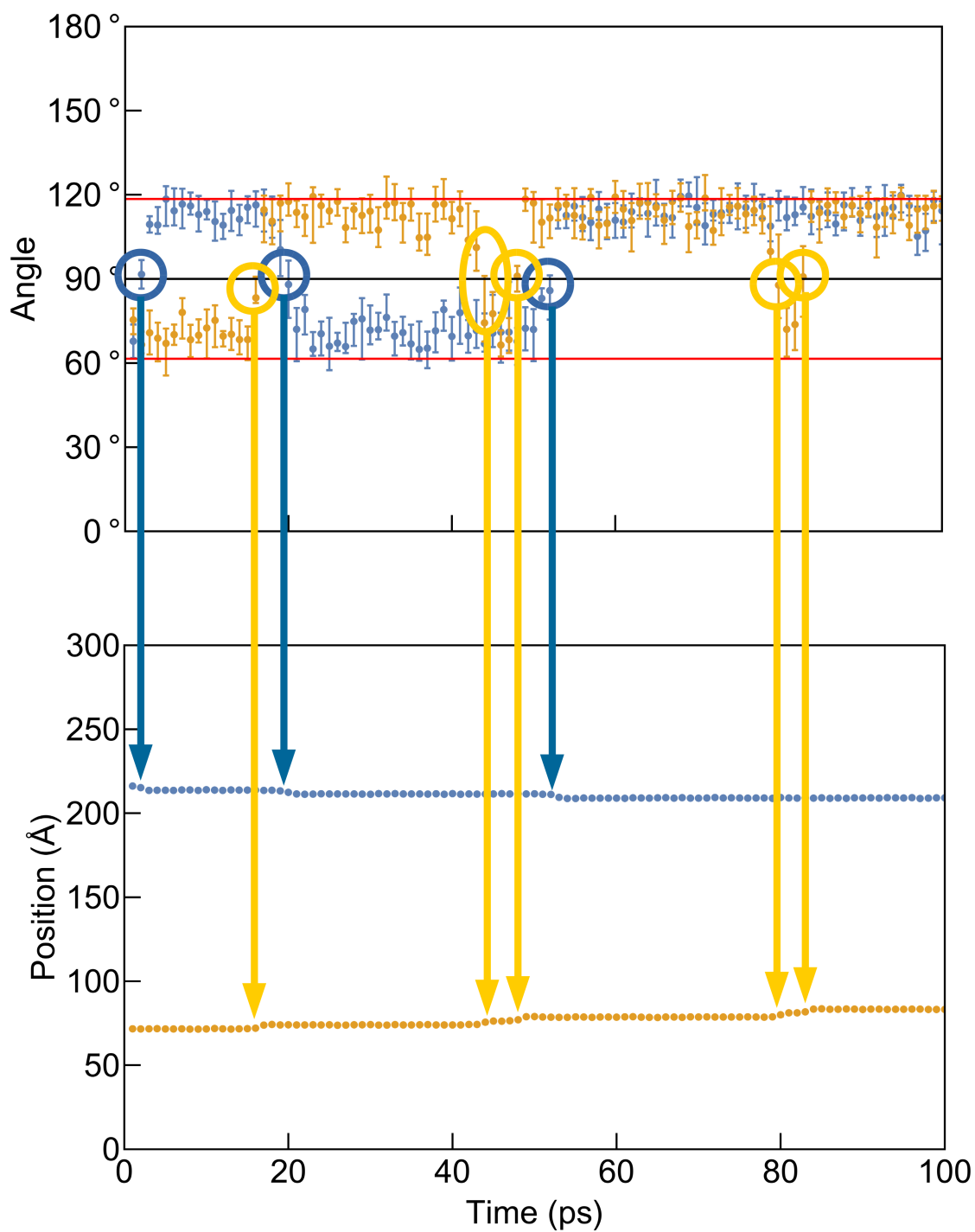
Figure 5.12: (Top) Dislocation core orientations during a MD simulation at 1 GPa compression and 200 MPa shear stress at 100 K. (Bottom) Dislocation centroid positions parallel to the [0001] axis the during the same simulation. Excursions of the core structure into the prismatic configuration are highlighted, and the correspondence between these and slip steps of the dislocations shown.
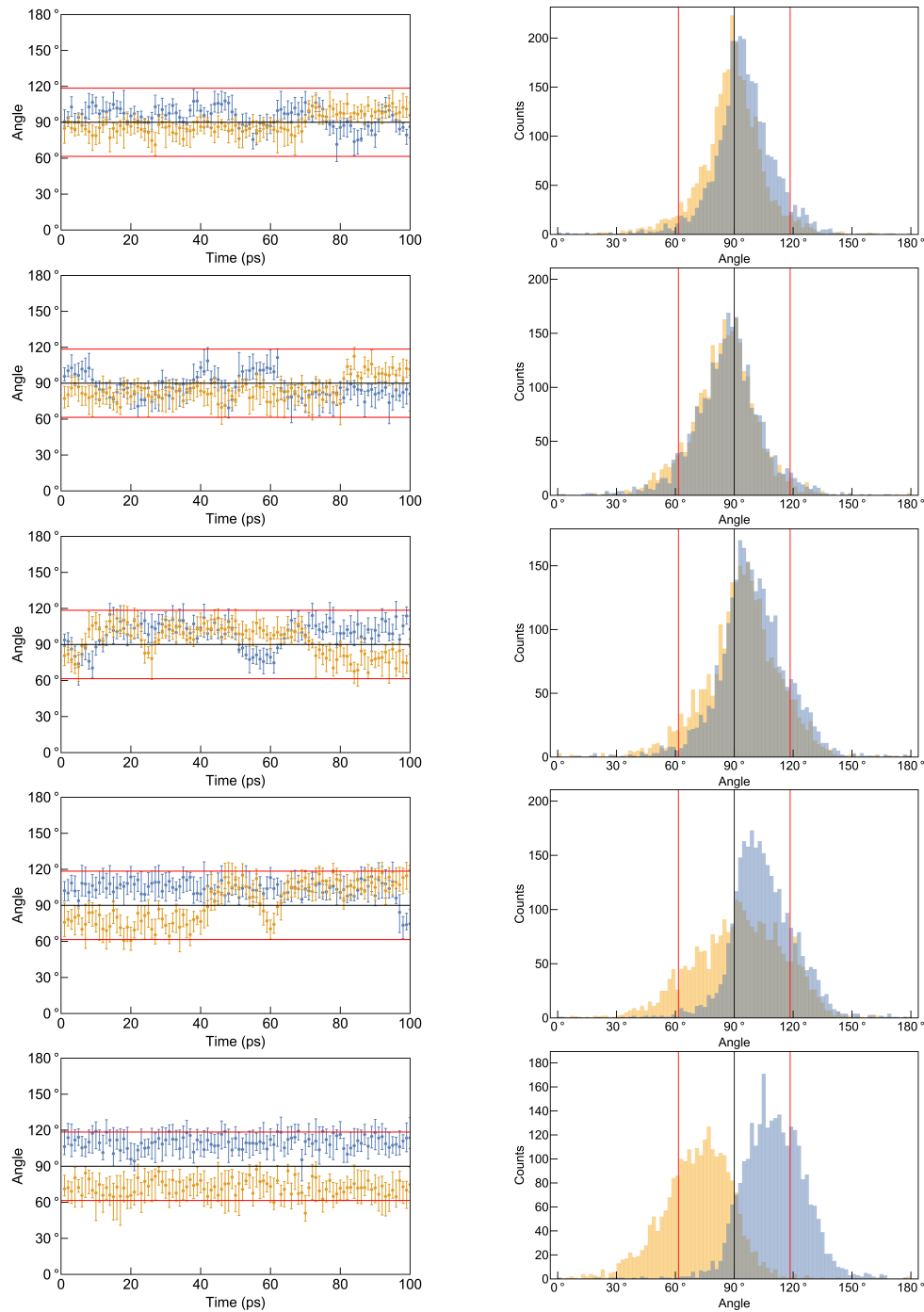
Figure 5.13: Core orientations (left) and histograms (right) of all core structure orientations slices for both dislocations in MD simulation at 0 MPa, 125 MPa, 200 MPa, 500 MPa, and 1 GPa (top to bottom) non-Schmid stress applied on the [1$\bar{1}$00] axis at 300 K. The black line shows the position of the prismatic orientation and the red lines are the pyramidal orientations.

prismatically oriented median structures at this pressure. This suggests that the transition pressure is reduced at higher temperature. Another way of stating this is that the pyramidal

orientations are favored by higher temperature, which implies that these are higher-entropy structures. Calculations on the temperature-dependence of dislocation core structures in semiconductors suggests that in that case vibrational entropy plays an important role in the dislocation structural properties at high temperatures[86]. However, I have seen no literature discussing entropy of competing dislocation core structures in metals. Even when high-temperature effects on core structure are discussed, the entropy of the structures is assumed to be the same[87].

This increase in pyramidal occupations at higher temperatures also suggests another surprising conclusion: increasing the temperature could actually decrease the strain rate for some stress states. Certainly at 500 MPa or 1 GPa compression it is expected that the increased accessibility of the prismatic configuration will lead to easier prismatic slip. At 0 MPa compression, though, the core structure is always prismatically oriented at 100 K, but at 300 K there is significant pyramidal orientation occupation. If the locking-unlocking mechanism dominates the strain rate, then there should be less slip at 300 K than at 100 K for small non-Schmid stresses. To discover whether this is the case, MD simulations under 200 MPa shear strain at 300 K were carried out and the resulting strains plotted in Figure 5.14.
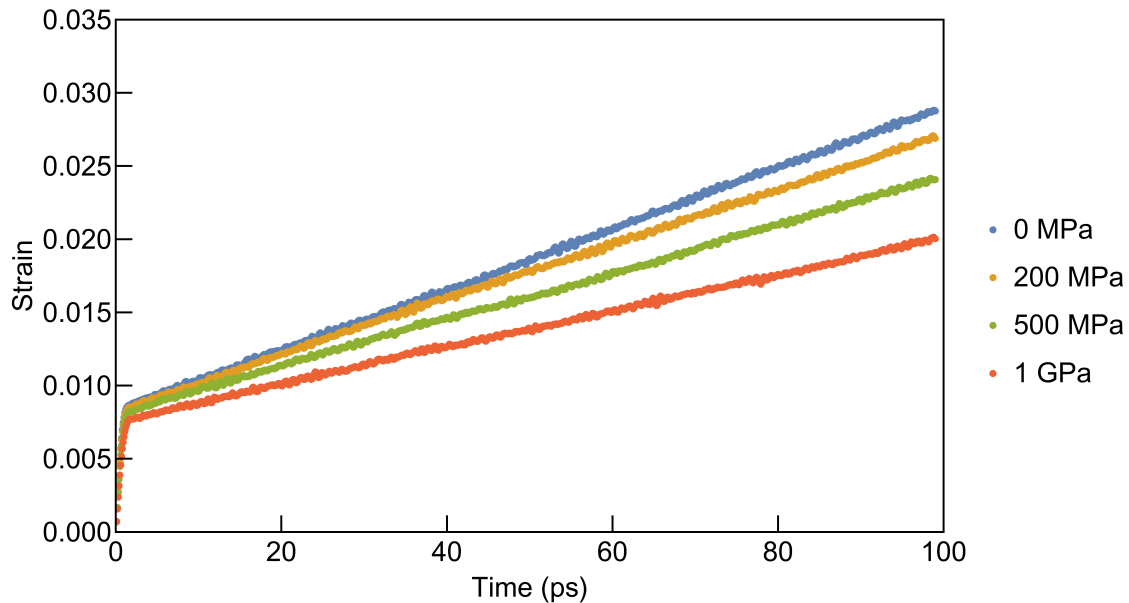
Figure 5.14: Shear strain vs time for MD simulations with 200 MPa shear stress for prismatic slip and 0 MPa, 200 MPa, 500 MPa, and 1 GPa non-Schmid compression along the [1$\bar{1}$00] axis applied at 300 K.

Clearly Figure 5.14 demonstrates that 300 K is sufficient temperature to unlock the dislocations under 1 GPa compression. This validates a key prediction of the locking-unlocking mechanism. It is also plain to see that the differences in strain between the different non-Schmid stress simulations are much smaller at 300 K than at 100 K. What cannot be seen by eye is that the plastic strain under 0 MPa compression at 300 K is actually somewhat lower than that at 100 K: 2.01% vs 2.45%. This proves the more surprising conclusion that increased temperature can reduce the strain rate if it promotes a core structure that is less

favorable for slip. Figure 5.15 shows the core structure distributions for these simulations at 300 K with applied shear stress, which validates that the changes are in fact due to changes in dislocation core orientations.

5.5 Conclusions

In this chapter I have developed (along with Ian Winter) a parameter (υ) based on elastic stability analysis that can accurately and rapidly characterize the extent of a dislocation core. I have also designed (along with Ian Winter and Daryl Chrzan) a fit to this parameter that can be used to extract the dislocation orientations of these cores, where the orientation corresponds to a primary plane of core spreading. Molecular dynamics simulations were performed over a range of temperatures and applied stresses – both non-Schmid and with shear stress oriented for prismatic slip – and core orientation distributions were calculated using this new method. This data illustrates a number of facts about the dependence of dislocation orientations on temperature and stress state. With increasing temperature, the width of orientation distributions is increased as higher-energy core structures become thermally occupied. With increasing compressive stress applied on the $[1\bar{1}00]$ axis, the dislocation core orientations shift from prismatic to pyramidal, but there is apparently no sharp transition between these states for this system size. For example, simulations at 100 K and 200 MPa compression show approximately equal occupation of prismatic and pyramidal orientations. Interestingly, for this MEAM potential the transition pressure from the prismatic to pyramidal core structure is lowered by increased temperature, implying that higher temperatures favor pyramidal orientations. This implies that these orientations have higher entropy than the prismatic orientation, a new wrinkle in the already-complicated field of screw dislocation core structures.

In molecular dynamics simulations with shear stress applied to induce prismatic slip, the locking-unlocking mechanism is apparent. Under 1 GPa compression at 100 K, every slip step of the dislocations can be shown to correspond to an unlocking event. At 300 K and the same stress, slip is substantially easier because the prismatic core structure is thermally accessible. In a surprising, but ultimately consistent, development the strain rate under no compression is reduced in these simulations by increasing the temperature, because this leads to a higher pyramidal core structure occupation.

These simulations provide the first atomistic observations of the locking-unlocking mechanism for $\langle a \rangle$-type screw dislocations in titanium. However, this is only one of many possible applications for this method. As previously discussed, there is a great deal still unknown about the form of the thermal distribution of dislocation core structures. Unfortunately, fully exploring time and spatial correlation of these core structures will require significantly more computational effort, as the (spatial) correlation length is greater than the depth of the supercells used for the calculations presented here. This insufficiency in supercell length may be responsible for the lack of an observed sharp transition between the dislocation core structures as a function of pressure at a fixed temperature, which otherwise is a surprising finding. Addressing these correlations and the energies of transitions between core structures of different orientations appears to be a promising area for further study. Perhaps addressing these areas could lead to the development of an Ising-like model for dislocation
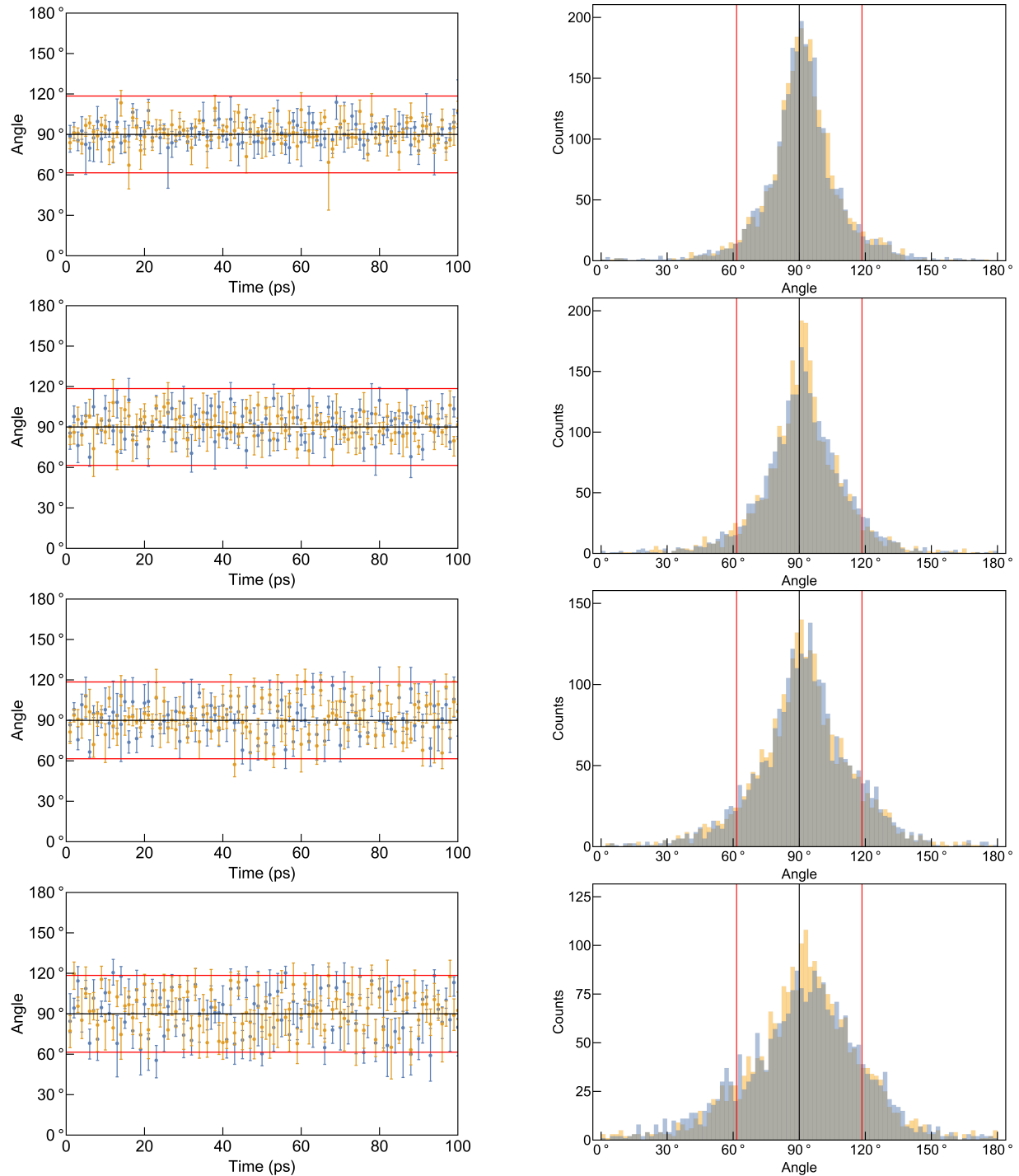
Figure 5.15: Core orientations (left) and histograms (right) of all core structure orientations slices for both dislocations in MD simulation with 200 MPa shear stress for prismatic slip and 0 MPa, 200 MPa, 500 MPa, and 1 GPa (top to bottom) non-Schmid stress applied on the [1$\bar{1}$00] axis at 300 K. The black line shows the position of the prismatic orientation and the red lines are the pyramidal orientations.

core structures.

Another opportunity created by development of the parameter υ is to study other crystal systems. Traditionally, dislocation core structures in bcc metals have been given the greatest amount of attention due to the importance of steels for commercial applications and the complicated extended structures of dislocations in bcc metals. In this case, a new type of fit (i.e. replacing Equation 5.2) would likely be required, because typically it is the size rather than the orientation of the core that is more interesting. In fact, it was in an effort to characterize the size of dislocation cores in a titanium-niobium alloy that Ian and I first began exploring development of the parameter υ. Certainly this remains a direction worth exploring.

Chapter 6:

⟨a⟩-Type Screw Dislocation – Interstitial Interactions

6.1 Introduction

Titanium alloys possess a number of highly desirable properties, including excellent corrosion resistance and high specific strength, which make them attractive structural materials for a wide range of commercial applications. Titanium alloys find widespread use as structural materials in aerospace and marine applications, as well as in biomedical implants. Despite these many attractive properties and the abundance of titanium in the crust of the Earth (it is the 4th most common metal[15]) the uses of titanium are limited by high costs. While the cost of metals is usually determined by scarcity, in this case

> *"The root cause of the high cost of titanium is its very strong affinity for oxygen."*
>
> - Fang, Middlemas, Guo, and Fan [88]

Naturally occurring titanium ores contain large amounts of oxygen. Of known reserves, approximately 93% are ilmenite ($FeTiO_3$) and the remaining 7% are rutile (TiO_2)[15]. The Kroll process, developed in the first half of the twentieth century, remains by far the most popular commercial method by which titanium ore is converted into high purity titanium alloy[89]. This process includes a number of energy intensive steps such as high-temperature carbo-chlorination of the ore to produce titanium tetrachloride ($TiCl_4$), followed by reduction with molten magnesium at over 1000 K for several days[88]. The energy input required during these steps is so high that raw titanium ore represents only 4% of the total cost of a commercial purity titanium alloy[89]. Efforts to reduce the cost of processing titanium are ongoing and have resulted in several new techniques. Among these are the Armstrong process in which boiled titanium tetrachloride and boiled sodium are combined continuously to produce high purity titanium powder, the FFC electrochemical process in which titanium oxide is reduced by calcium[90], and the DRTS process in which titanium slag is ball milled with magnesium hydride to form titanium hydride (TiH_2) which is then dehydrogenated[88]. However, none of these new methods have yet made a significant commercial impact.

Oxygen alters the mechanical properties of titanium alloys significantly and in ways that are not desirable for most applications. Specifically, in the hexagonal-close-packed (hcp) α phase of titanium, small variations in the content of interstitial impurities are observed to have deleterious effect on fracture toughness. For example, comparing CP α-Ti grades 1 and 3, a difference in oxygen content of 0.17 wt. % leads to nearly a factor of 7 decrease in impact toughness[91]. In addition, interstitial solutes are known to lead to increased planarity of slip (see below) which may contribute to many fatigue initiation modes. Because of such

embrittlement effects, in the processing of titanium, and manufacturing of components using this material, significant precautions must be taken to constrain variations in the content of interstitial solutes such as oxygen. The consequence is significant increase in cost, and challenges to the application of titanium in modern additive-manufacturing processes.

Despite the fact that the embrittling effects of interstitial impurities in α-Ti have been well documented for more than four decades[92], consensus on the microscopic origins of these effects has remained elusive. This situation inhibits the use of modern alloy-design strategies to develop alternative compositions and processing strategies to mitigate the detrimental effects of impurity content, with an ultimate goal of lowering cost and expanding usage of this Ti more broadly for applications requiring lighter-weight structural materials. In this chapter I propose an atomic-scale mechanism underlying the macroscopic embrittling effect of oxygen in hcp titanium alloys, referred to as an interstitial shuffling mechanism (ISM). This mechanism is identified through consideration of observed effects of oxygen concentration and temperature on deformation microstructures in α-Ti, coupled with first-principles calculations of generalized stacking-fault energies and atomistic simulations of dislocation glide in the presence of oxygen solute (see Figure 6.1). The identification of this ISM mechanism provides a framework for fundamental understanding of experimental observations, and it offers a path forward in the design of titanium alloys that make use of deliberate additions of interstitial solutes, but which display increased tolerance to small variations in the content of these alloying elements.

6.2 Methods

6.2.1 Modified Generalized Stacking Fault Calculations

In generalized stacking fault energy calculations[66] a continuum of possible stacking faults are considered, and an energy surface representing these is formed. The method presented here is modified to accommodate investigation of interstitial effects by performing calculations in series (with each input configuration depending on previous output) and by searching along a path in the direction of the Burgers vector through the stacking fault energy surface with relaxations permitted perpendicular to the Burgers vector. This approach allows for examination of steric interactions between oxygen interstitials and dislocation slip, isolated from dislocation core effects and without the need for expensive dislocation quadrupole configurations. It also solves the issue of where to place the oxygen interstitial that would arise if the entire stacking fault energy surface was calculated with each configuration independently initiated. In the generalized stacking fault construction a slip plane of interest is selected, and supercell constructed that is long (at least 30 Å) in the direction normal to this plane, with the perpendicular directions generally shorter. The supercell has periodic boundaries in the directions contained in the slip plane, but is non-periodic (using a vacuum layer of at least 15 Å in plane-wave based DFT calculations) perpendicular to the slip plane. A single oxygen atom is placed in an octahedral site on the slip plane, which is chosen to be midway up the supercell.

The calculation proceeds as follows:

(1) atom positions are fully relaxed,
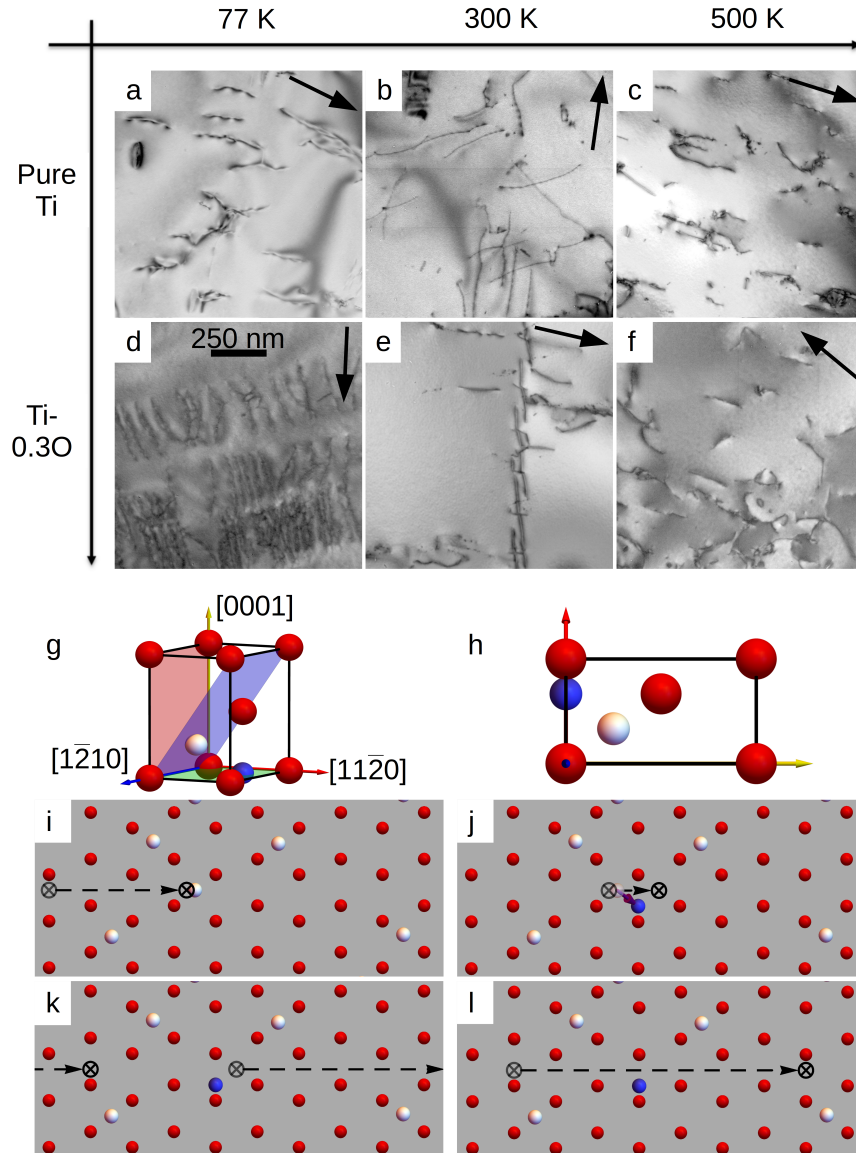
Figure 6.1: (a-f): Microstructures observed on the $[2\bar{1}\bar{1}0]$ orientation of temperature-controlled deformation tests. The scale bar applies to all (a-f), and the arrows indicate the $[01\bar{1}0]$ direction in each panel. Only wavy slip was observed in pure Ti samples (a-c). Conversely, Ti-0.3O deformation microstructures were very sensitive to temperature. At 77K, planar slip dominates (d). At 300K, both wavy and planar slip modes are present (e). At 500K, only wavy slip was observed (f). The hcp lattice with octahedral (white) and hexahedral (blue) sites, and prism, pyramidal, and basal planes (red, blue, green) is shown in (g). (h) shows the orientation of (i-l). (i-l) demonstrate the key steps in ISM. In (i), the first dislocation (cross symbol) on a prism slip plane encounters an octahedral oxygen and slip is resisted. It eventually (j) overcomes this obstacle, and in the process shuffles the oxygen to a hexahedral site. The dislocation continues slipping, and subsequent dislocations follow behind (k). These dislocations see a reduced barrier from the hexahedral oxygen, and thus easily slip on this plane (l).

(2) atoms above the slip plane are displaced by a fraction of the Burgers vector relative to those below,

(3) constrained relaxation of atomic positions,

(4) repeat (2)-(3) until slip is complete.

As the oxygen atom is on the slip plane, it is displaced by half the step size to avoid biasing its relaxation. During constrained relaxation titanium atoms are allowed to relax within the plane normal to the Burgers vector. The reasoning behind this is allowing as much relaxation as possible most closely reflects realistic conditions. However, if atoms are allowed to relax along the Burgers vector they will simply always undo the applied slip. The oxygen atom is always permitted to relax without constraint. Lattice parameters are kept fixed with the justification that in a bulk crystal the large undeformed volume would constrain the dimensions of the area around the dislocation or stacking fault. The modification introduced here to allow planar relaxation of the titanium atoms is an important one, as the novel findings presented below only occur if this relaxation is allowed.

The energy (E) is output after each relaxation, and the generalized stacking fault energy at each step is calculated as follows:

$$GSF(\lambda) = \frac{E(\lambda) - E(\lambda = 0)}{A} \tag{6.1}$$

where λ is the fraction of slip along the Burgers vector and A is the slip plane area per supercell.

6.2.2 Dislocation Calculations

Calculations on quadrupolar dislocation configurations were initialized by introducing two ⟨a⟩-type screw dislocations with Burgers vector a$\frac{\langle 11\bar{2}0 \rangle}{3}$ (of opposite sign for the two dislocations) into a pure Ti supercell of the desired size using the method of Daw[62] and accounting for the distortion from the dislocations as prescribed by Lehto and Öberg[63].

To measure dislocation bowing angles, I constructed six configurations employing the method of Cai *et al.*[93], modified to include homogeneously strained layers at the surfaces to suppress the image forces on the dislocation[94]. The supercells contained 1,806,336, 3,612,672, and 5,419,008 titanium atoms and 1 oxygen atom placed in the slip plane of the dislocation (one case of octahedral and one of oxygen in basal-plane site was considered for each supercell size). The three supercell sizes differed only in the length along the dislocation line direction (which corresponded to the length between oxygen pinning sites), and were 281 Å, 563 Å, and 845 Å. I performed constant strain-rate MD simulations for each simulation cell at zero temperature, with a strain-rate of 8.17×10^6 s^{-1}.

6.2.3 Computational Settings

All DFT calculations were performed using the Vienna ab initio simulation package (VASP)[35, 36]. The projector-augmented wave (PAW)[26, 61] method was used, and the calculations were not spin-polarized. Use was made of the Perdew-Burke-Ernzerhof (PBE)[25] form of the general gradient approximation (GGA), and the PAW potential employed in the calculations included the $3d^2 4s^2 3p^6$ electrons as valence states for titanium. For oxygen, the

PBE potential with Wigner-Seitz radius 0.82 Å was employed. The second-order Methfessel-Paxton smearing scheme[28] was used in the Brillouin-zone integrations with a width of 0.2 eV. The cutoff energy for the plane wave basis was 400 eV for modified GSF calculations involving only titanium, 520 eV for modified GSF calculations which included oxygen atoms, and 600 eV for calculations including dislocations. Electronic structure self consistency loops were terminated at an energy tolerance of 10^{-5} eV, and ionic relaxation was terminated at an energy tolerance of 10^{-4} eV for modified GSF calculations and force tolerance 0.02 eV/Å for dislocation calculations. K-point meshes for modified GSF calculations were generated using the K-Point Grid Server[95] with minimum real-space grid distance of 37 Å, and for dislocation calculations a $1 \times 1 \times 5$ Γ-centered grid was used. These parameters have been demonstrated to be sufficient to capture the relevant information about these dislocation core structures[53].

Classical potential calculations were performed using the Large-scale Atomic/Molecular Massively Parallel Simulator (LAMMPS)[42]. The modified embedded atom method[41] (MEAM) potential of Hennig *et al.*[65] was used for pure Ti calculations, as well as the closely related potential for Ti-O systems by Zhang and Trinkle[96]. This Ti-O potential has been shown to represent the relative energies of the important interstitial sites for oxygen in titanium (octahedral, hexahedral, and crowdion) accurately, as well as the barriers between these sites[96]. Relaxation was performed at zero temperature and terminated when the norm of the forces on all atoms was less than 10^{-4} eV/Å.

6.2.4 Experimental Methods

The experiments described here were carried out entirely by Ruopeng Zhang. However, because they form a crucial part of this chapter I will briefly describe his methods and include the resulting images.

Pure Ti (with < 0.1 wt% O) and a binary Ti-0.3 wt%O alloy were obtained from TIMET and annealed at 900°C in vacuum for 24 hours to achieve similar grain size and evenly distributed orientations. Both materials were polished and cut into pieces with a thickness of 2 mm. These pieces were then ground down to a thickness of ∼150 μm. The samples were divided into three different temperature groups and temperature-controlled deformation was conducted to introduce dislocations. For the low temperature test, pure Ti and Ti-0.3O thin foils were first submerged in liquid nitrogen and then bent at center to 30° after thermal equilibrium had been established. For the room temperature test, pure Ti and Ti-0.3O thin foils were bent at center to 30° at room temperature. For the high temperature test, pure Ti and Ti-0.3O thin foils were first preheated to 150°C and then covered by Crystalbond 509 to prevent further oxidation and achieve a more stable temperature profile. The thin foils were continuously heated up to 230°C and then bent at the center to 30°. To validate the experimental setup, a deformation-free pure Ti sample was also prepared to investigate the amount of dislocations introduced by twin-jet polishing.

3 mm disks were cut from the regions near bend curves on the deformed thin foils. The final polishing was conducted with a twin-jet electropolisher using a solution of 6% perchloric acid and 94% methanol. The samples were polished at -40°C for ∼5 minutes.

Transmission electron microscopy analysis was performed using a JEOL 3010 microscope

with operating voltage of 300 kV.

Figure 6.2 shows the state of the pure titanium material without any applied deformation, demonstrating that the vast majority of dislocations observed in the deformed material were produced during the bending experiment.
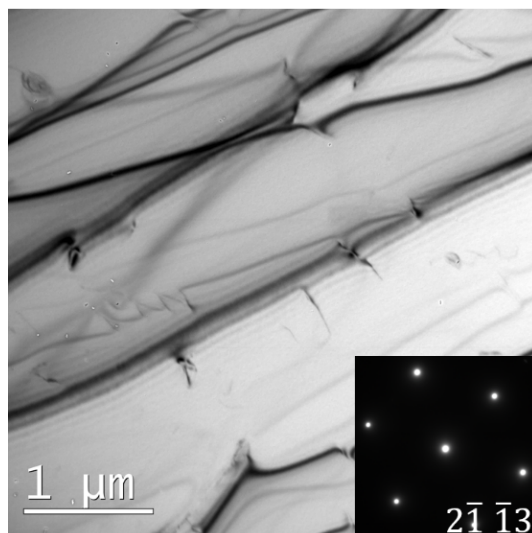
Figure 6.2: Bright field image from a $[2\bar{1}\bar{1}3]$ orientation of the non-deformed pure Ti control sample. The dislocation density is very low compared to the deformed samples.

6.3 Deformation microstructures in α-Ti: planar slip

Insights into the origin of the interstitial solute atoms on the mechanical behavior of α-Ti can be achieved by consideration of the dislocation microstructures that result from deformation of samples with varying oxygen content, and at varying temperatures. When the oxygen content is increased, and/or the deformation temperature of oxygen-containing samples is decreased, there is an increasing tendency for dislocations to exhibit planar slip, i.e., the motion of large collections of dislocations on a narrow band of slip planes, with infrequent cross-slip out of well-developed slip bands. The behavior is illustrated qualitatively in Figure 6.1, panels (a)-(f) which show microstructures of ⟨a⟩-type screw dislocations obtained by deforming single-phase α-Ti alloys with two different oxygen concentrations, at three different temperatures spanning 77 K to 500 K. Planar slip bands were only observed in samples with higher oxygen concentration deformed at lower temperatures (see in particular panels (d) and (e)). Similar observations have been reported previously in the literature (c.f., Williams et. al.[97]).

The formation of planar slip bands is known to be correlated with the degradation of a number of mechanical properties in α-Ti, including a reduction in formability[92], toughness[98, 99], and fatigue life[100], and an increase in susceptibility to stress-corrosion cracking[101]. Planar slip is associated with an observed decrease in work hardening[98] that contributes to reduction in toughness. Further, the formation of planar slip bands lead to pronounced stress concentrations at the edges of the associated dislocation pileups that can

assist crack nucleation in fatigue and stress-corrosion cracking. Accordingly, if one seeks to mitigate the effect of oxygen content on failure mechanisms in α-Ti, it is important to understand the intrinsic origin of their role in promoting planar slip.

Planar slip is also observed in α-Ti alloys that contain high concentrations of the substitutional solute element Al. In this case, planar slip is understood to originate from a phenomenon referred to as "short-range-order softening"[92, 102–104, 99]. This mechanism is associated with the propensity of Al atoms in the α-Ti-Al alloy to form pronounced short-range order (SRO). The lead dislocation in a pileup encounters increased resistance to glide, as its advance leads to the destruction of the SRO, with an associated energy cost that is quantified in terms of the magnitude of a so-called diffuse anti-phase boundary (DAPB). After the passage of the first few dislocations on a given slip plane, the SRO is destroyed (due to the finite correlation length associated with the ordering) and it is "softened" to the motion of subsequent dislocations on the same plane. This softening mechanism thus promotes the formation of planar slip bands.

While the SRO slip-plane softening mechanism is accepted for α-Ti-Al alloys, it is unclear whether the same mechanism is operative in Ti-O alloys, due to the much lower concentration of solute atoms in this latter case. To investigate this possibility, David Olmsted undertook a detailed computational study of equilibrium SRO and the associated magnitudes of DAPB energies in the α-Ti-O system, employing the framework of first-principles cluster-expansion methods and Monte-Carlo simulations[105]. These calculations establish that the DAPB energies in samples with the highest oxygen concentrations representative of CP α-Ti are two orders of magnitude smaller than those computed in Ref.[104] for α-Ti-Al alloys. The magnitudes of DAPB energies in α-Ti-O alloys calculated by David are even smaller than those computed in Ref.[104] for high-temperature processed and rapidly quenched α-Ti-Al alloys where planar slip was not observed experimentally[106]. Therefore SRO softening is not the mechanism underlying planar slip for α-Ti-O alloys. In the following section, I present results of first-principles generalized-stacking-fault energy calculations and atomistic simulations of dislocation slip in α-Ti-O that lead to the identification an alternative interstitial shuffling mechanism underlying planar-slip behavior.

6.4 Interstitial shuffling mechanism identified through computational simulations

I begin by considering the results of calculations of generalized stacking fault (GSF) energies, obtained by first-principles DFT calculations. In these calculations I used a modified GSF method in which steps along the direction of the Burgers vector through the stacking fault energy surface were simulated, with relaxations permitted perpendicular to the Burgers vector. The lowest-energy path across the associated γ-surface in the direction of a dislocation Burgers vector is related to the energy barrier for slip of that dislocation. The GSF energy on the {1100} prism plane for pure Ti and Ti with $\frac{1}{8}$ of the octahedral sites on the slip plane occupied by oxygen impurities are shown in Figure 6.3a. The prism plane is of interest because slip of $\langle a \rangle$-type screw dislocations on this plane represents the most active dislocation slip system in CP-Ti[16].

For pure Ti the GSF energy increases rapidly up to a shift of $\lambda = 0.35$ (i.e., 0.35 of the a
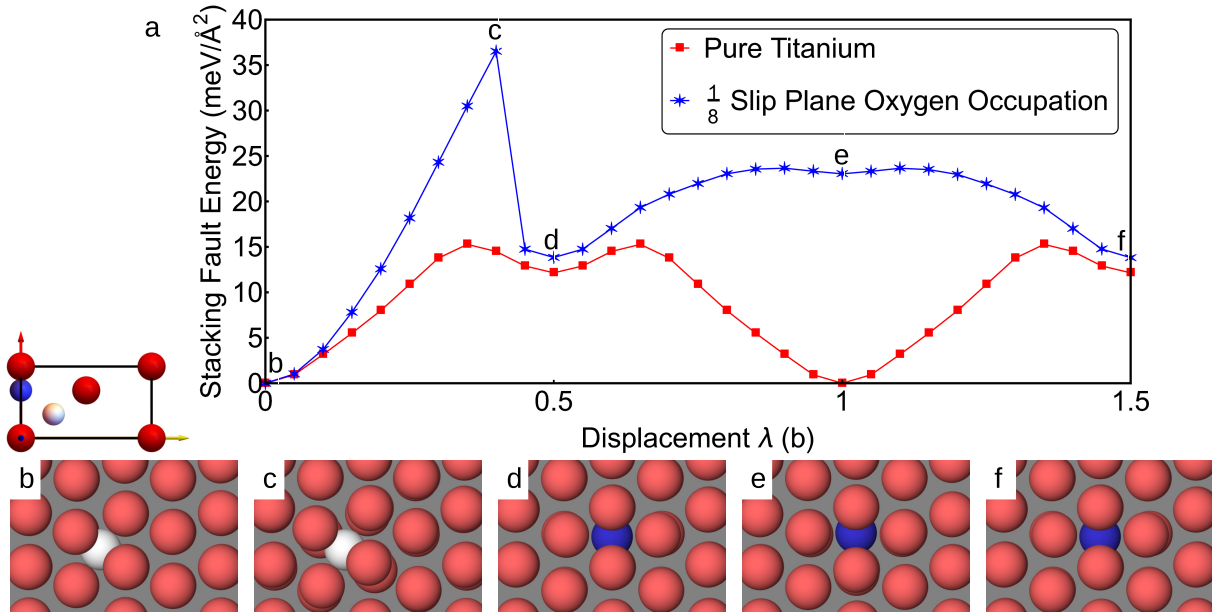
Figure 6.3: (a) Modified generalized stacking fault energy on the prismatic plane calculated with DFT. (b-f) show oxygen position for selected steps, starting from octahedral (b). (c) shows the distorted octahedral site at the maximum in energy. In steps (d) and (f) the oxygen is in a octahedral site formed at the stacking fault. (e) shows the hexahedral site. For directions, see Figure 6.1.

lattice spacing), then decreases to a local minimum at $\lambda = 0.5$. The barrier to complete the slip (i.e., from $\lambda = 0.5$ to 1) is symmetric. In comparison, for the results along the same slip path in the system containing oxygen, the GSF energy is seen to increase more sharply during the early stages of slip, until $\lambda = 0.45$ when a sharp drop in energy occurs. This energy drop is associated with the shuffling of the oxygen interstitial out of the low-energy octahedral site, to a site within the basal plane that is associated with the so-called hexahedral[107] position in the undeformed hcp structure. In the hcp structure the oxygen atom has a much higher energy in this hexahedral site than it does in the more open octahedral interstitial position. However, the octahedral site becomes increasingly compressed during slip, while the basal-plane site becomes more "open" along the shear path.

The oxygen shuffle and associated drop in energy in GSF calculations was reported previously in Refs.[58, 108, 109]. In the context of the present study, however, the most interesting finding, not reported in earlier calculations, is that when slip is completed ($\lambda = 1$) the oxygen interstitial remains in the basal-plane site (the barrier to return to the octahedral site is 890 meV), and the barrier to further slip is reduced significantly. Specifically, consider two complete slip paths for the oxygen-containing system shown in Figure 6.3a: $\lambda = 0 \to 1$, and $\lambda = 0.5 \to 1.5$. For both the energy barrier to slip corresponds to the difference between the lowest and highest GSF energies along the path. In the first slip event the barrier is 36.5 meV/$\mathring{A}^2$, and in the second it is reduced to 9.8 meV/$\mathring{A}^2$. Because the basal-plane site is part-way out of the slip plane, the steric hindrance to slip is significantly reduced by the shuffle of the oxygen atom into this site.

As discussed above, the effect of the density of oxygen on the slip plane is examined

by changing the supercell size in MEAM calculations. In Figure 6.3a it appears that the shape and magnitude of the barrier to slip depend strongly on the oxygen density. However, Figure 6.4 illustrates that the additional energy per oxygen atom is roughly independent of density over the range considered. There is also good agreement between DFT and MEAM calculations based on this measure. The low energy associated with the oxygen atoms at λ = 0.5 and 1.5 illustrate that the octahedral site in the basal plane at these slip values is very similar to the octahedral site between basal planes at $\lambda = 0$.
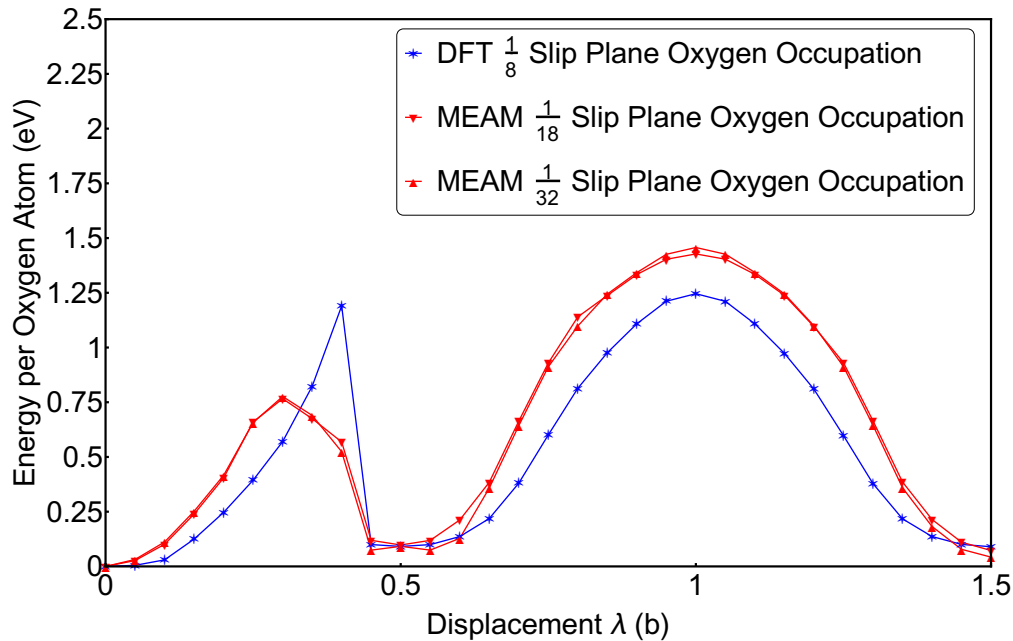
Figure 6.4: Additional energy per oxygen atom in modified generalized stacking fault energy calculation on the prismatic plane calculated with DFT (blue) and MEAM (red) potentials. Square symbols indicate no oxygen atoms in unit cell, and circles, diamonds and triangles 1 oxygen per 8, 18 and 32 sites on slip plane.

After prismatic slip the next most active dislocation mode in CP titanium alloys is associated with glide of $\langle a \rangle$-type screw dislocations on the $\{1\bar{1}01\}$ first-order pyramidal plane[16]. For this reason the procedure described above was used to examine the effect of pyramidal slip. The results of these calculations are shown in Figure 6.5. Similar to what was found for prism slip, a sharp drop in energy occurs near $\lambda = 0.5$ corresponding to the oxygen atom moving from a site between basal planes to a site directly in a basal plane. Again this shuffle is not reversed when slip is completed and the oxygen comes to be in a hexahedral site at $\lambda = 1$. This results in a reduction to the barrier for slip after the first dislocation similar to that on the prism plane. Using DFT energies, in the first slip event the barrier to slip is GSF(0.45) - GSF(0) = 46.9 meV/$\mathring{A}^2$, and in the latter the barrier is GSF(0.8) - GSF(0.5) = 11.3 meV/$\mathring{A}^2$.

The GSF calculations thus suggest the following interstitial shuffling mechanism (ISM) for slip-plane softening, illustrated in Figure 6.1i-l. The first slip event on a given slip plane leads to displacement of oxygen impurities to the basal-plane site (Figure 6.1i-j). The
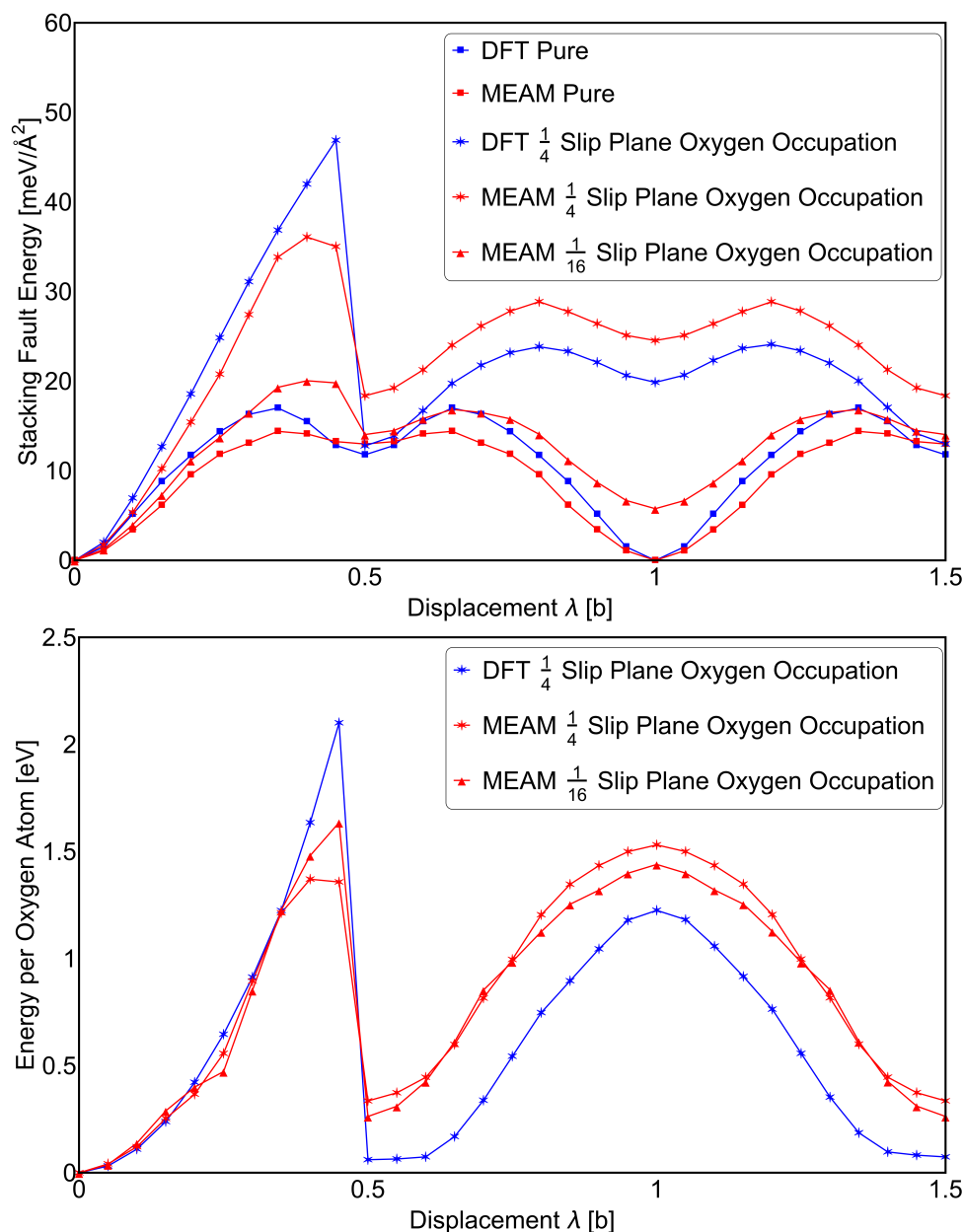
Figure 6.5: (Top) Generalized stacking fault energy on the pyramidal plane calculated with DFT (blue) and MEAM (red) potentials. Square symbols indicate no oxygen atoms in unit cell, and circles and triangles 1 oxygen per 4 and 16 sites on slip plane. (Bottom) Additional energy per oxygen atom.

displaced oxygen atoms remain in these positions, which leaves the barrier to further slip reduced (Figure 6.1k-l).

One potential criticism of this method is that the relaxation of the titanium atoms is over-constrained. Restricting their relaxation parallel to the Burgers vector direction is necessary to some extent within the GSF model, because if they are allowed to relax in this direction the stacking fault will never be formed. However, this restriction almost certainly influences

the calculated energy barriers for slip, and it is possible that it also changes the behavior of the interstitial atom. This second possibility would be a serious problem for this work. To check this, there are at least two available options. One is to constrain only the titanium atoms that are not near the interstitial oxygen, and hope to thereby reduce the effect of this constraint on both the calculated energies and the behavior of the oxygen. I have done this, but will not present the data because it falls almost exactly in line with that presented already. Another option is to use the NEB method which has been employed throughout this dissertation. Originally in undertaking this work, the NEB method was deliberately avoided because to use it I would have to choose which interstitial site the oxygen will end in. Had I done this, the ISM likely would not have been uncovered. In fact, calculations along these lines have been done by Kwasniak *et al.*[110] for the titanium-oxygen system in DFT. However, because they assumed the oxygen returns to the octahedral site their NEB calculations force it to do so, and thus while they see it shift to the basal-plane site they do not see that it would tend to remain there when this site becomes the hexahedral site.

However, once one is aware of the possibility of a permanent shuffling of the interstitial, NEB calculations starting and ending with oxygen in the different interstitial sites can be performed and compared. To demonstrate that NEB calculations are in agreement with the modified GSF calculations, I performed three NEB calculations in the MEAM potential. These are shown in Figure 6.6. In the first (reaction coordinate $0 \rightarrow 1$) the oxygen begins and ends in the octahedral site. In the second (reaction coordinate $1 \rightarrow 2$) it begins in the octahedral site and ends in the hexahedral site, as occurs in the modified GSF calculations for the first slip event. In the third (reaction coordinate $2 \rightarrow 3$) the oxygen begins and ends in hexahedral site, as the modified GSF calculations suggest is that case for subsequent slip events. I have put the energies in the same units as GSF calculations, and it can be seen that they are on the same order but slightly lower than those from the modified GSF calculations, which makes sense given the greater degree of relaxation permitted. The key point, however, is that forcing the oxygen to return to the octahedral site is unfavorable relative to permitting it to switch to the hexahedral site. Furthermore, the slip event in reaction coordinate $2 \rightarrow 3$ requires the least increase in energy, again agreeing with the modified GSF calculations and the ISM formulation.

Given the limitations inherent in the GSF model, which does not explicitly consider the geometry of a localized dislocation core, it is important to verify the key findings using models that involve explicit consideration of realistic dislocation structures. This was done in the present work employing both DFT calculations and classical atomistic simulations based on a modified embedded-atom-method (MEAM) potential[41]. This proceeds in the following sections.

6.5 Oxygen - Dislocation Interaction Energy Calculations

I began this verification by comparing DFT and MEAM results for dislocation-oxygen interaction energies. In these calculations I considered a periodic quadrupolar arrangement of dislocations, with oxygen atoms introduced either far from the dislocation or within the dislocation core, and in both the octahedral and basal-plane sites. Taking an octahedral oxygen atom placed as far from the dislocation as possible to be the reference state in both
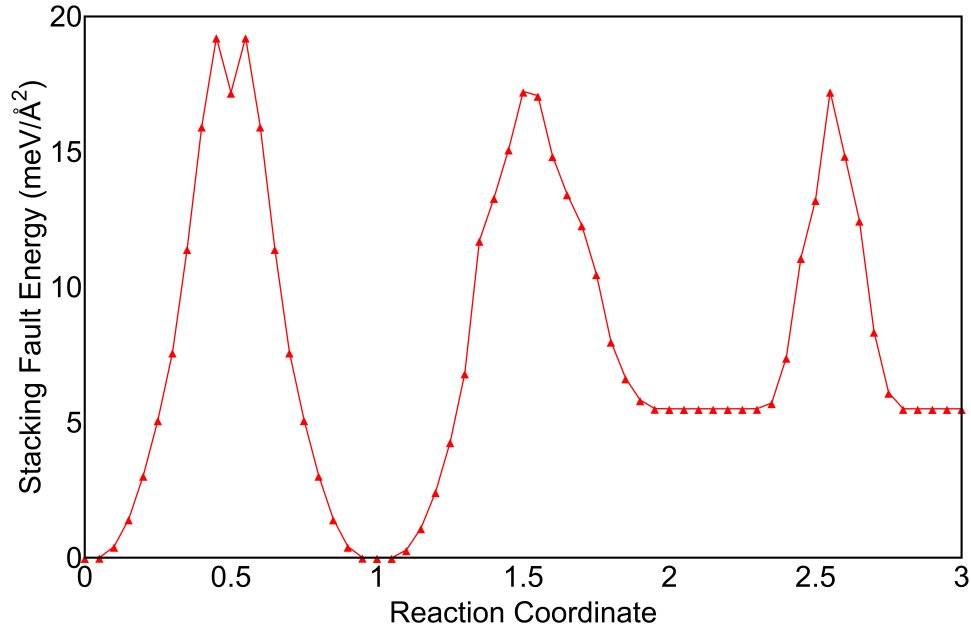
Figure 6.6: NEB calculations for GSF-type model in MEAM with 1 oxygen per 32 slip plane octahedral sites. For step $0 \to 1$ one Burgers vector of slip is simulated, with the oxygen starting and ending in the octahedral site. The local minimum at reaction coordinate 0.5 corresponds to the oxygen briefly switching to the basal-plane site. In step $1 \to 2$ the oxygen begins in the octahedral site and ends in the hexahedral site, or in other words is shuffled. In step $2 \to 3$ the oxygen begins and ends in the hexahedral site. This step presents the smallest barrier to slip, indicating the same softening effect observed in the modified GSF calculations.

the DFT and classical atomistic calculations, I find that the MEAM potential well reproduces the dislocation - oxygen interaction energies for several different configurations, as presented in Table 6.1. The MEAM potential also well reproduces the DFT results for GSF energies shown in Figure 6.3. Given this finding, I proceeded by focusing on use of the MEAM potential as the basis for direct molecular-dynamics (MD) simulations of dislocation glide.

Both DFT and MEAM calculations used supercells that were three Burgers vectors deep and contained one oxygen atom, which ensures that oxygen atoms do not sit in directly neighboring sites. The DFT (MEAM) calculation supercells contained 576 (9216) titanium atoms. The MEAM calculations involving the hexahedral site underestimate the DFT energy by approximately 30 meV/atom, which is less than the 100 meV underestimate for the hexahedral oxygen energy found by Zhang and Trinkle without a dislocation[96]. The larger overestimate of the energy of an octahedral oxygen inside the dislocation core is likely an effect of the small size of the DFT simulation cell: introducing an oxygen atom into one of the dislocation cores changes the structure of that core, and in the case of our DFT calculation this induces a small reconfiguration of the other core.

This data reveals an important difference between the interactions of octahedral and hexahedral oxygen atoms with $\langle a \rangle$-type screw dislocations in titanium: while the ground state of the entire system is an octahedral oxygen far from the dislocation core, the energy of a hexahedral oxygen atom within a dislocation core is lower than that of a hexahedral oxygen

Table 6.1: Dislocation - oxygen interaction energies from DFT and MEAM calculations with oxygen in octahedral and hexahedral interstitial sites far from and within dislocation cores.

Oxygen Position	DFT Octahedral Energy	MEAM Octahedral Energy	DFT Hexahedral Energy	MEAM Hexahedral Energy
Outside Core	0 (reference)	0 (reference)	1.158 eV/atom	1.128 eV/atom
Inside Core	0.204 eV/atom	0.266 eV/atom	0.135 eV/atom	0.108 eV/atom

far from a dislocation core. Thus there is an attraction between hexahedral oxygens and $\langle a \rangle$-type screw dislocation core. This is true in both DFT and MEAM, and is in agreement with the local minima of the additional energy per oxygen atom shown in the Figure 6.4 at $\lambda = 0.5$ and $\lambda = 1.5$ and the maximum at $\lambda = 1.0$.

While the short-range repulsive interaction between octahedral oxygen atoms and screw dislocation cores has previously been discussed[58], the attraction between hexahedral oxygen and screw dislocation cores is a new finding warranting further investigation. To verify this interaction and determine its range, a series of MEAM calculations was performed, each with the oxygen in a different position relative to the dislocation. Some of these interaction energies are shown in Figure 6.7. This plot verifies that there is zero long-range interaction between the oxygen octahedral and the dislocation. For the hexahedral oxygen, however, there is an attraction that extends some tens of Å, depending on the direction of the separation.

One possibility is that the attraction is due to a long-range elastic interaction between the strain field of the dislocation and the stress induced by the interstitial on the surrounding titanium lattice. This can be checked by calculating the eigenstrain $\boldsymbol{\eta}_{hex}$ for the hexahedral oxygen and calculating the interaction energy following Hanlumyuang *et al.*[111]. For the purposes of comparison, I also computed $\boldsymbol{\eta}_{oct}$. For both interstitials I used a supercell containing 13824 titanium atoms and 1 oxygen atom to calculate the eigenstrain within the MEAM potential. The resulting eigenstrains were:

$$\boldsymbol{\eta}_{oct} = \begin{bmatrix} 0.07 & 0 & 0 \\ 0 & 0.07 & 0 \\ 0 & 0 & 0.25 \end{bmatrix} \tag{6.2}$$

$$\boldsymbol{\eta}_{hex} = \begin{bmatrix} 0.64 & 0 & 0 \\ 0 & 0.64 & 0 \\ 0 & 0 & -0.38 \end{bmatrix} \tag{6.3}$$

which both only contain diagonal strain components. The interaction energy (E_{int}) for a
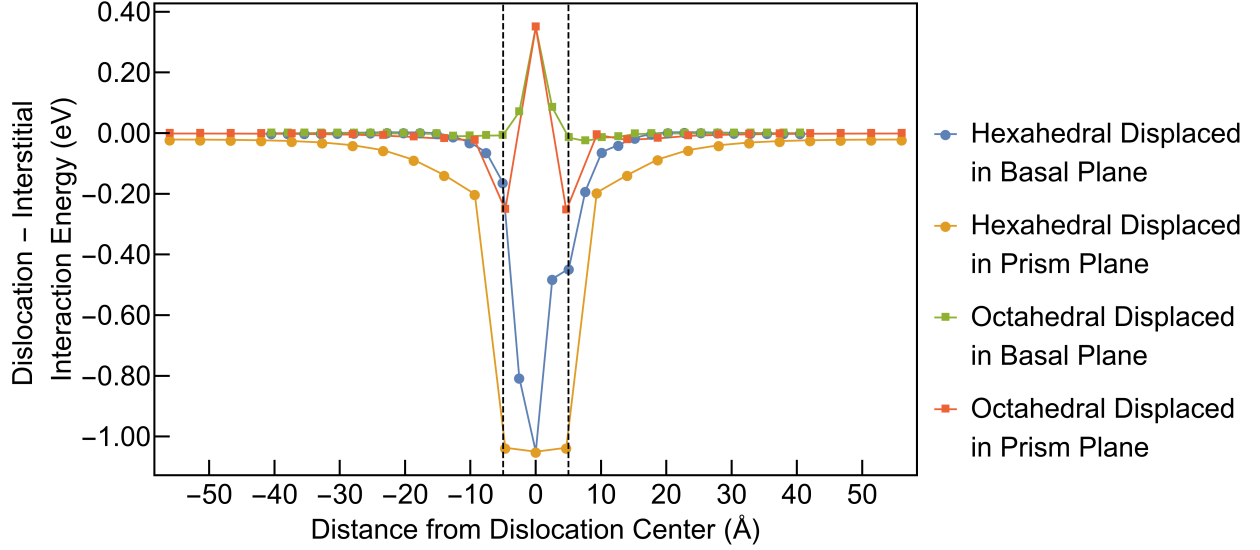
Figure 6.7: Dislocation – interstitial interaction energies for various positions of the oxygen interstitials relative to the dislocation core. Each interstitial type was placed in a series of positions within the same prism plane as the dislocation, and within the same basal plane as the dislocation. The dashed lines show the approximate extent of the dislocation core region. The interaction energies within the core reflect both slip and rearrangement of the core, along with any elastic interaction that might be present.

point defect with eigenstrain $\boldsymbol{\eta}$ at position $\boldsymbol{r}$ relative to a dislocation with strain field $\boldsymbol{\Delta}$ is[111]:

$$E_{int} = -\frac{v_0}{2} c_{ijkl} \eta_{kl} \Delta_{ij}(\boldsymbol{r}) \tag{6.4}$$

where v_0 is the volume of the primitive unit cell. The method of Stroh[112] for anisotropic elasticity theory was used to determine the strain field due to the dislocation. Using this in conjunction with the interstitial eigenstrains and Equation 6.4 I find that there is no elastic interaction with screw dislocations, as these have chiefly shear strain fields.

Similarly, the elastic dipole tensor ($\boldsymbol{P}$) can be calculated to determine the elastic interactions. One convenient method for calculating the elastic dipole tensor is to use the forces on atoms calculated by LAMMPS to calculate the Kanzaki force[113] ($\boldsymbol{F}$). This can be done by relaxing the atomic positions with the interstitial, then removing it and finding the resulting force: this force is the negative of the Kanzaki force. The elastic dipole tensor is then:

$$P_{ij} = \sum_{k=1}^{N} (r_i^k - r_i^{interstitial}) F_j^k \tag{6.5}$$

where the sum is over non-interstitial atoms and the positions are those relaxed with the interstitial in place. Using Equation 6.5, the elastic dipole tensors for octahedral and hexahedral interstitial oxygen atoms in titanium were calculated for the same supercells as used

for the eigenstrain calculations:

$$\boldsymbol{P}_{oct} = \begin{bmatrix} 2.71 & 0 & 0 \\ 0 & 2.71 & 0 \\ 0 & 0 & 5.72 \end{bmatrix} \tag{6.6}$$

$$\boldsymbol{P}_{hex} = \begin{bmatrix} 12.48 & 0 & 0 \\ 0 & 12.48 & 0 \\ 0 & 0 & 4.19 \end{bmatrix} \tag{6.7}$$

in eV units. Similar to Equation 6.4, the expression for the elastic interaction energy between the strain field from a dislocation and the elastic dipole tensor due to an interstitial is[114, 115]:

$$E_{int} = -P_{ij}\Delta_{ij}(\boldsymbol{r}) \tag{6.8}$$

However, this calculation still indicates no coupling with strain field calculated via Stroh theory for ⟨a⟩-type screw dislocations.

So, it appears the unexpected elastic interaction does not arise from any unusual strain field about the hexahedral interstitial. The other option is that the strain field around the dislocation differs from that predicted by my linear elasticity model, and in a way that causes it to couple to hexahedral oxygen but not octahedral oxygen. This additional field has been examined before, and is referred to as the dislocation core field[116–118]. This field results from terms in the displacement field resulting from elasticity theory that are dropped from the expansion[119, 117]. Rather than compute the total strain induced on box by the dislocation to investigate this possibility as done by other groups[117, 118], however, I use OVITO to compute the elastic strain at each atom[120] in the supercell containing the dislocations but no oxygen interstitials. This reveals substantial diagonal components of the strain due to the dislocations, whereas Stroh theory predicted these to be near zero.

Equation 6.8 is then employed with these strains in place of $\boldsymbol{\Delta}$. This allows for a mapping of predicted elastic interaction energies at every titanium atomic position in the supercell. Of course the interstitials would sit between these atoms rather than directly on them, but this still provides a reasonable prediction of the interaction. These maps are presented in Figure 6.8.

Figure 6.8 reveals the relatively long-range interaction between hexahedral oxygen and the dislocation core field, while there is minimal interaction with the octahedral oxygen except within the dislocation core itself, in good agreement with the direct interaction energy calculations shown in Figure 6.7. A few useful points of comparison between the direct interaction energy calculation and the calculation using Equation 6.8:

1. the difference in interaction energy between the octahedral site midway between dislocations on the basal plane and the octahedral site midway between dislocations on the prism plane is calculated directly to be 1 meV, and predicted to be 3 meV,
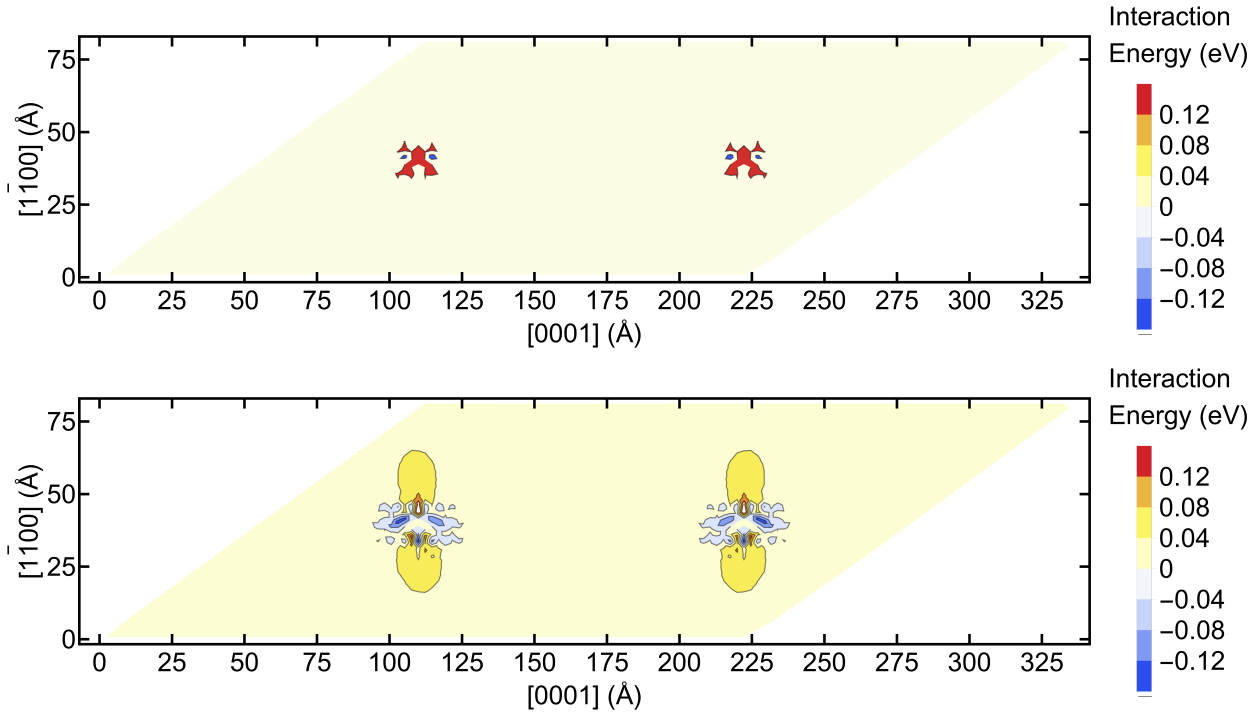
Figure 6.8: Elastic interaction energy (calculated with Equation 6.8) for the eigenstrains due to oxygen interstitials in the atomic strain field due to a dislocation quadrupole calculated from relaxed MEAM simulation. (Top) Interaction between octahedral oxygen and the dislocation strain field. (Bottom) Interaction between hexahedral oxygen and the dislocation strain field.

2. the difference in interaction energy between the hexahedral site midway between dislocations on the basal plane and the hexahedral site midway between dislocations on the prism plane is calculated directly to be 21 meV, and predicted to be 16 meV,

3. the difference in interaction energy between the lowest-energy octahedral site in the prism plane containing the dislocations and the octahedral site midway between dislocations on the prism plane is calculated directly to be -5 meV, and predicted to be -20 meV,

4. the difference in interaction energy between the lowest-energy hexahedral site in the prism plane containing the dislocations and the hexahedral site midway between dislocations on the prism plane is calculated directly to be -175 meV, and predicted to be -154 meV.

These points illustrate that the predictions based on the core strain field are in good agreement with the direct calculations, and predict a medium-range attraction between hexahedral oxygen and the dislocation core, but negligible interaction between octahedral oxygen and dislocation. The predictions become less accurate very near to the core, but this is not surprising because the interactions are predicted at titanium rather than interstitial sites and the strain varies more rapidly nearer to the core.

6.6 Molecular Dynamics Simulations

The MD simulations were designed to investigate whether the two main features of the DFT-based GSF energy calculations, related to the proposed interstitial softening mechanism, namely: (1) that interstitial octahedral oxygen atoms on a slip plane are shifted to basal-plane sites and remain in these sites when a dislocation passes, and (2) that the barrier for subsequent dislocation slip when the oxygen atom is displaced to the basal-plane site is significantly reduced. These effects were explored in separate MD simulations using different dislocation configurations.

To investigate the first effect, i.e., interstitial shuffling induced by dislocation glide, I constructed a quadrupolar configuration of ⟨a⟩-type screw dislocations in a simulation cell containing 491520 titanium atoms and 4915 oxygen atoms (initialized in octahedral sites), 30 Burgers vectors (88 Å) in depth along the dislocation line direction. Use of a sufficiently deep supercell is critical, as insufficient dislocation line length in the supercell results in oxygen-promoted changes of the dislocation core structure, involving a spreading on the basal plane, followed by rapid cross-slip to avoid oxygen interstitials.

Molecular dynamics simulations were performed at room temperature (300 K), imposing a shear strain rate of 8×10^7 s^{-1}. The strain was oriented to induce prismatic slip of the dislocations. This process was continued until the dislocations slipped through the oxygen interstitials, crossed the periodic boundary and returned to the original positions. During this process, more than half of oxygen atoms encountered by a dislocation are observed to shuffle from octahedral sites to hexahedral sites and they remained in those positions for the duration of the simulation. The results thus support the first key finding from the GSF calculations.

The second type of MD simulation was designed to investigate the magnitude of slip-plane softening resulting from the shuffle of oxygen impurities from octahedral to hexahedral sites. In these simulations I investigated the maximum bowing angles of dislocations pinned at hexahedral and octahedral oxygen for three different spacings of the solute atoms along the dislocation line. The bowing angle θ is measured as the angular displacement of the dislocation line from the ideal straight screw dislocation line direction. Following Foreman and Makin[121], I assume this maximum bowing angle depends only on the strength of the obstacle and the dislocation line tension T (with the latter assumed constant). When dislocation bows around an obstacle, the component of its line tension that is exerted on the obstacle is $2T\sin(\theta)$[121]. The use of isolated interstitials in this way allowed for more accurate measurement of the obstacle strength than obtainable from calculations involving many interstitials. Additionally, the previously-discussed high strain-rate calculations resulted in some debris trailed behind the dislocation, which hindered second passes through the same slip plane.

The bowing angle is most readily observed in a simulation supercell that contains only one dislocation. Therefore, I constructed three supercells containing one dislocation, differing in the length along the dislocation line direction. For each supercell I performed two strain-rate controlled MD simulations, one each with a single octahedral or hexahedral oxygen in the dislocation slip plane. I then used the Dislocation Extraction Algorithm (DXA)[84] in OVITO[85] visualization software to determine the position and shape of the dislocation at

each step of the simulation. The maximum angle of the dislocation at the oxygen interstitial position (θ_o for octahedral and θ_h for hexahedral) was thus determined.

I find the maximum dislocation bowing angles to be approximately constant with respect to the interstitial spacing. For octahedral oxygen the maximum angle is between 11.4° and 11.8°, and for hexahedral it is between 7.1° and 7.8°. Table 6.2 shows all calculated values.

Table 6.2: Maximum bowing angle of dislocations pinned at octahedral and hexahedral oxygen atoms with three different spacings. The relative strength of the obstacles is given by the ratio of the sines of their bowing angles.

Interstitial Spacing	θ_o	θ_h	$\frac{\sin(\theta_o)}{\sin(\theta_h)}$
281 Å	11.8°	7.8°	1.51
563 Å	11.4°	7.1°	1.59
845 Å	11.8°	7.6°	1.55

Figure 6.9 shows corresponding images of the dislocation lines, with the adaptive Common Neighbor Analysis (a-CNA)[122] used to color the titanium atoms. Because the stress on the simulation box was very similar under each of the conditions shown (in all cases $\sim$240 MPa), the ratio of the pinning strengths of the octahedral and hexahedral oxygen is equal to the ratio of the sine of the maximum bowing angles. This ratio is consistent when the interstitial spacing is varied, and indicates that octahedral oxygen presents a barrier to prismatic $\langle a \rangle$-type screw dislocation slip that is 155% of that presented by hexahedral oxygen. The MD results thus confirm the second feature of the ISM, namely that shuffle of the oxygen from octahedral to hexahedral sites leads to slip-plane softening, since the impurities in the latter sites provide a lower pinning strength.

To put the results from the simulations that led to Figure 6.9 in further context, the ratio of pinning strengths for the obstacles is $\frac{\sin(\theta_o)}{\sin(\theta_h)}$. The ratio of critical stresses scales as $\left(\frac{\sin(\theta_o)}{\sin(\theta_h)}\right)^{3/2}$[123]. Thus, the 1.55 times higher pinning strength of the octahedral site requires 1.93 times higher stress to overcome for equal obstacle concentrations. For an oxygen concentration of 0.3 wt% (as in the samples used to obtain the images in Figure 6.1), I find that $\tau_c = 175$ MPa for octahedral oxygen and 91 MPa for hexahedral oxygen, following the analysis of Hanson and Morris[123]. These stresses (and the difference between them) are similar to the yield stresses for CP-Ti alloys[92], supporting the validity of the atomistic calculations presented here.

Along with the increased bowing angle associated with the oxygen impurities in an octahedral relative to basal-plane hexahedral site, another difference between the configurations shown in Figure 6.9 is the location of the oxygen relative to the dislocation when maximum bowing occurs. For the octahedral site (Figure 6.9a and c) the oxygen is at the front of the dislocation line, resisting slip of the line through the site. For the hexahedral site (Figure 6.9b and d) the oxygen trails the dislocation, preventing it from breaking free of the interstitial. This is related to the attractive interaction between the hexahedral site and an $\langle a \rangle$-type screw dislocation. I observe that this attraction leads to negative dislocation curvature early in the simulation, with the dislocation segment near the hexahedral oxygen atom advancing
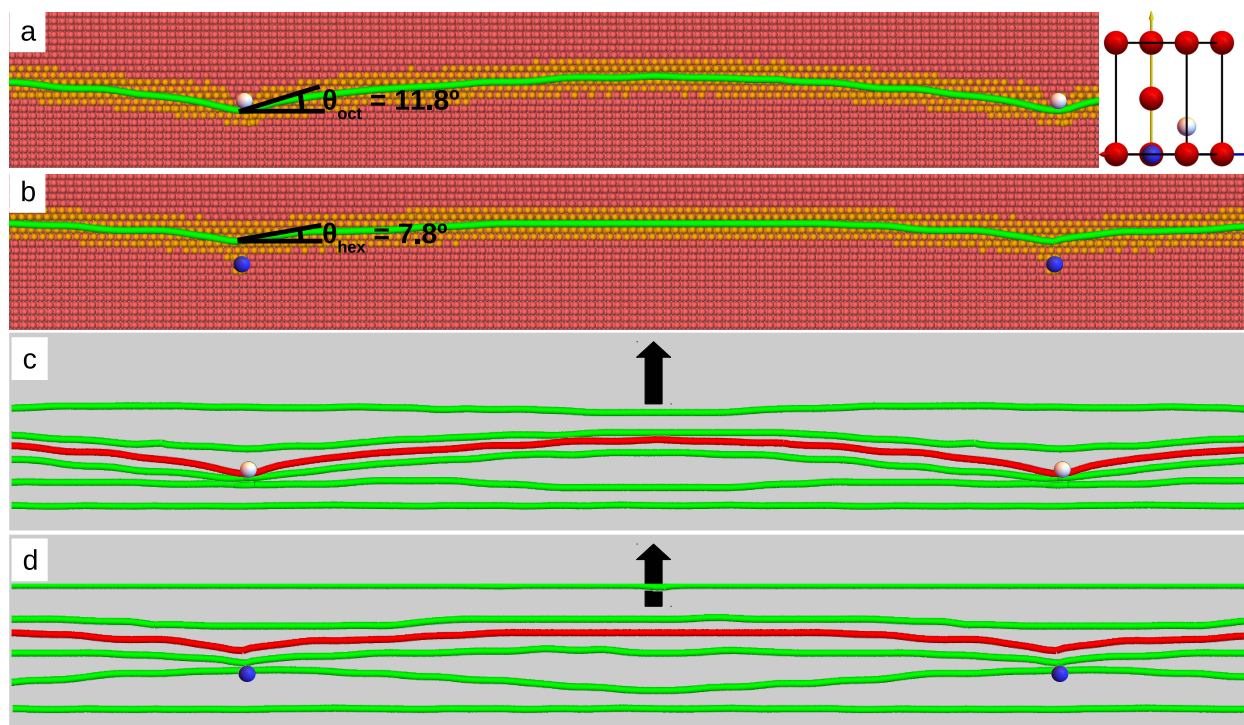
Figure 6.9: Dislocation position as determined by DXA for octahedral (a) and hexahedral (b) interstitials with spacing 281 Å at the critical bowing angle. The coloring of titanium atoms is by a-CNA, with hcp lattice red and defect region orange. (c) and (d) show a series of timesteps, with the red dislocation lines represent the critical configuration for either case. The large arrows indicate the slip direction.

more rapidly than the rest of the line. This negative curvature reaches comparable values to the maximum positive curvature, as shown in Figure 6.9b. By contrast, oxygen in the octahedral site displays a repulsive interaction with ⟨a⟩-type screw dislocations, as discussed previously in the literature[58].

6.7 Discussion in context of experimental observations

The Interstitial Shuffling Mechanism for slip-plane softening provides a framework to understand a number of observations related to the effect of oxygen interstitials on the mechanical behavior of Ti, as illustrated in Figure 6.11.

Many experimental observations[16, 97, 92, 102, 103, 124] indicate that increasing oxygen content and/or decreasing temperature lead to an enhanced tendency towards planar slip in α-Ti alloys. Consider first the oxygen concentration effect. Dislocations in a slip plane that has already been softened through the ISM will experience an increased preference to continue slipping in that plane with increasing oxygen concentration, because the barrier to dislocation motion in alternative slip planes increases with increasing density of strong octahedral pinning sites.

Turning next to the effect of temperature, thermal fluctuations will cause some of the

oxygen atoms that have been shuffled by dislocations into the high-energy hexahedral sites to hop back into the stable octahedral position. This hexahedral to octahedral hopping will increase the resistance to slip in a given slip band, and therefore decrease the tendency to planar slip. The extent to which these oxygen-atom hops are effective will depend strongly on the temperature, through the normal Arrhenius dependence of the hopping rate, and will be increasingly effective at mitigating the slip-plane softening effect with increasing temperature. The characteristic time (t_{hop}) for a hexahedral oxygen to diffuse back to an octahedral site at temperature T can be estimated given the attempt frequency (ν) and energy barrier (E):

$$t_{hop} = \left(\nu e^{\frac{E}{K_b T}} \right)^{-1}. \tag{6.9}$$

I compute t_{hop} using values for ν and E calculated by Wu and Trinkle[125], and compare to the typical time between dislocations passing an interstitial, t_{slip}. Consider the representative element containing one dislocation shown in Figure 6.10. The element height (L) is the average spacing between active slip planes, and its width (d) is the average spacing between dislocations on one of these slip planes. The dislocations are assumed to slip at velocity v. Thus, one passes a given point on the slip plane once every $t_{slip} = \frac{d}{v}$ seconds.
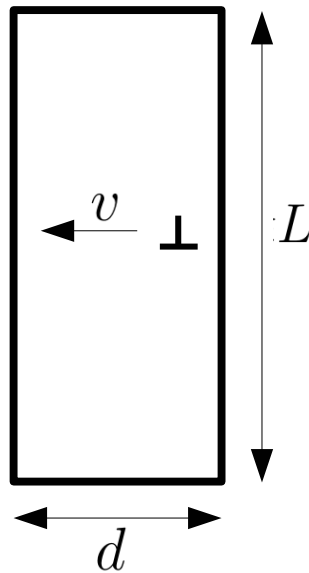
Figure 6.10: Representative element used to estimate slip event rate. L is the average distance between active slip planes in the system, and d is the average distance between dislocations on an active slip plane. These dislocations move at velocity v.

The picture described above suggests an interplay between the athermal slip-induced shuffling of oxygen to hexahedral sites, which leads to slip-plane softening, and thermal recovery assisted by hopping of oxygen back to octahedral positions. Deformation microstructures featuring planar slip are anticipated when $t_{slip} < t_{hop}$.

Previously reported calculated energy barriers and attempt frequencies[125] associated with oxygen hopping from hexahedral to octahedral sites in α-Ti suggest that at room

temperature t_{hop} is on the order of tens of seconds. For material undergoing planar slip, this is much slower than t_{slip}, which I estimate to be on the order of 10^{-5} seconds under typical conditions (i.e strain rate of ~ 10 s^{-1} and ~ 1 μm between active slip planes). Thus, at these modest strain rates at room temperature the tendency for planar slip can be understood. By contrast, due to the rapid decrease in t_{hop} with increasing temperature, the tendency for planar slip will be reduced at higher temperatures. For example, at 500K, t_{hop} is on order of 10^{-5} seconds, similar to t_{slip} and thus no planar slip is predicted or observed. The inverse interplay between temperature and composition on the tendency for planar slip, suggested by the ISM picture, is illustrated in Figure 6.11 and is qualitatively consistent with reported experimental observations[97].
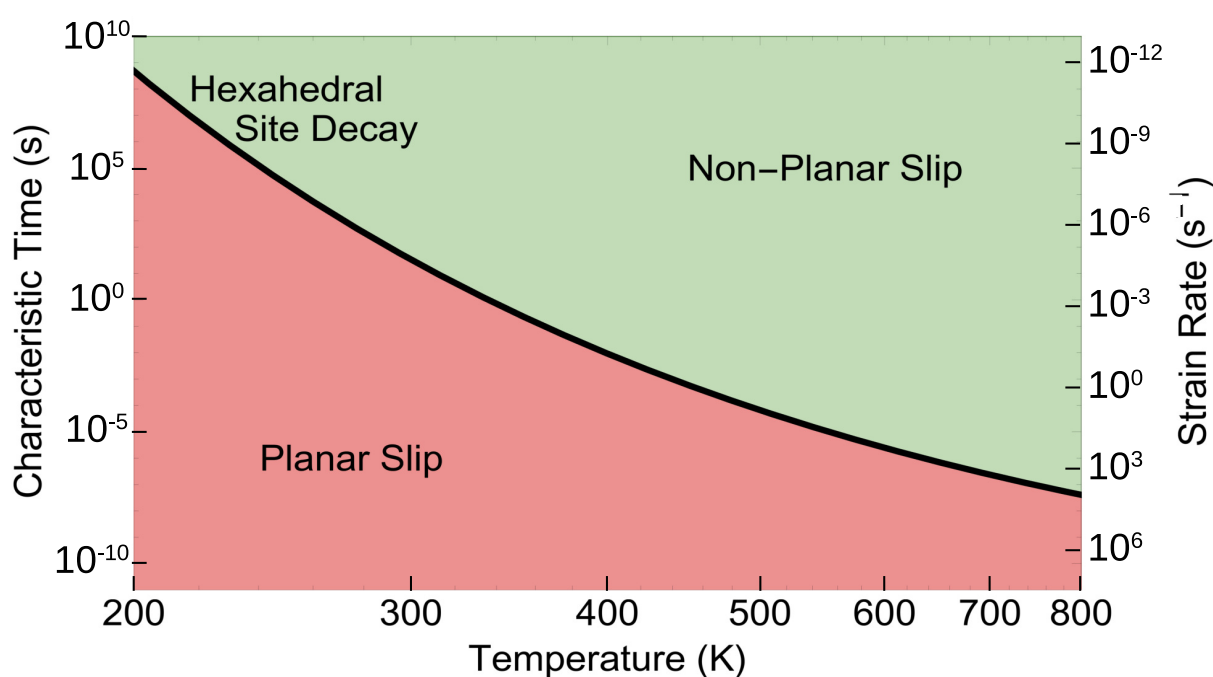
Figure 6.11: Comparison between characteristic time (left axis) for oxygen diffusion from the hexahedral site to the octahedral with typical time (left axis) between dislocations on a slip plane under different strain-rates (right axis), assuming 1 μm spacing between active slip planes. For temperature and strain rate conditions below the curve I predict planar slip to occur, provided the system contains sufficient oxygen.

The ISM picture also suggests that the tendencies for planar slip will be strongly dependent on strain rate. In Figure 6.11, I compare t_{hop} with t_{slip} to estimate what strain-rate and temperature combinations are likely to result in planar slip based on ISM, provided there is sufficient oxygen in the alloy. Combinations that fall into the lower region are likely to exhibit planar slip because the dislocation velocity required to accommodate the strain rate outpaces the diffusion of oxygen atoms from the hexahedral site to the octahedral. In the upper region the temperature is high enough and strain rate low enough that oxygen atoms tend to move back to the octahedral site between passing dislocations, and therefore planar

slip is not predicted by ISM.

6.8 Outlook for alloy design

The ISM identifies that a key factor in mechanical response is the timescale for an oxygen interstitial solute to hop out of the hexahedral back into the octahedral site (t_{hop}). If this time scale is fast relative to the rate of dislocation passage during deformation (t_{slip}), planar slip can be mitigated. The ISM thus presents a principle for the design of α-Ti alloys with decreased tendencies for embrittlement due to increasing oxygen content. Specifically, if through alloying t_{hop} can be decreased, the temperatures above which planar slip is avoided can be reduced (i.e., the black line in Figure 6.11 moved to lower temperatures). Work by Wu and Trinkle[126] suggests that these possibilities might be realized by alloying. In their study of substitutional solute effects on hopping rates they calculated the effect of many metals on the relative stability of the octahedral and hexahedral interstitial sites for oxygen in titanium. Their study also found that Al solutes increase the barrier to oxygen motion from the hexahedral to octahedral site, while Sc solutes lower this barrier, based on DFT calculations. This strategy thus suggests a framework for designing Ti alloys that are more tolerant to increasing interstitial content, and which may behave in a more ductile manner even under higher strain rates.

More generally, the ISM identified here may apply to other alloy systems containing interstitial solutes that interact strongly with the relevant dislocations. The basic requirements for the ISM to be operative are only two interstitial sites differing in dislocation pinning strength, and the possibility for dislocations to shuffle interstitials from one of these sites to the other. Due to the significant deleterious effects of planar slip on toughness, it is valuable to identify mechanisms underlying this phenomenon and associated pathways to control them. In this context, the ISM identified here contributes generally to the fundamental knowledge of possible origins for embrittlement due to interstitial solutes, and provides a framework for the design of improved Ti alloys in particular.

Chapter 7:
β to α Transition at Screw Dislocations

This chapter is something of a change in pace from those that have preceded it. While the focus remains on atomistic simulations of titanium, here I discuss phase transformation rather than plasticity. Some constants remain: the same MEAM potential for titanium is used, and the simulations involve quadrupolar arrangements of screw dislocations. Others have changed: the dislocations are in the bcc phase rather than hcp, they are of interest as heterogeneous nucleation sites rather than carriers of plasticity, and the temperature range of the simulations is much higher.

This chapter involves work that was performed in collaboration with other students in the Chrzan research group, which has been submitted for publication with *Physical Review Materials* and is reproduced here with the permission of coauthors. Ian Winter assisted with the elastic interaction calculation in Equation 7.5, which was the most important tool used to make the predictions about nucleation to compare to my simulations. Henry Geerlings and Daryl Chrzan worked through the elasticity theory required to construct the coexistence supercells used for simulations in one of the checks on the calculation of the transition temperature. Joseph Lin performed the preliminary simulations that lead to the interesting observations reported here.

7.1 Introduction

Titanium alloys are of obvious technological importance due to their often superior mechanical properties. These properties are engineered into the material through a variety of alloying additions and processing routes. A key aspect of this engineering is that Ti alloys have multiple phases accessible at room temperature - the α-phase (hexagonal close packed - hcp), the β-phase (body centered cubic - bcc) and the ω-phase (simple hexagonal). Alloy engineering often exploits these phase transitions (or seeks to suppress them) to improve alloy properties, and consequently the mechanisms by which the phase transformations occur are of interest.

Nucleated phase transitions offer the opportunity to influence the kinetics of the phase transformation. More specifically, first-order transitions can nucleate homogeneously within a (nominally) translationally invariant system and they can nucleate heterogeneously upon some defect within the transforming system, the latter of which is often overwhelmingly preferred. For example, suppression of heterogeneous nucleation sites for solidification can lead to substantial supercooling of liquids. Thus, understanding the heterogeneous nucleation paths available to the system can allow for control of a first-order phase transformation of interest. In pure Ti, the β to α phase transition is expected to proceed via the well-known Burgers path[127]. The Burgers path consists of both a strain and shuffling of atoms,

described in more detail in Section 7.4. This path, however, involves overcoming an energy barrier, and hence the transition is first-order.

Due to the technological importance of α/β-Ti alloys, the α to β and β to α transitions in Ti have been studied extensively in experiment[128–137] as well as in phase field simulations[138–140]. The consensus among these previous studies is that the orientations of post-transformation α Ti grains are selected by the Burgers relation. Several of the studies which employed electron backscattering diffraction (EBSD) or X-ray diffraction further concluded that there is selection among the possible orientation variants resulting from the Burgers path[128–131]. In particular, Gey *et al.* have shown that increasing the degree of hot rolling in the β phase increases the degree of variant selection, and that the α variants preferentially selected are linked to the most active slip systems in the parent β grain[129]. Qiu *et al.* used anisotropic elasticity theory as well as phase field simulations to show that the stress fields around dislocations in the β phase interact with α nuclei, and that this elastic interaction dominates the variant selection during nucleation[138].

Atomistic simulations of the β to α transition around dislocations are presented, with findings that are in good agreement with the preceding experimental and phase field work. In this paper, the influence of $\langle 1\ 1\ 1 \rangle_\beta$-type screw dislocations on the β to α transition in pure Ti is studied using molecular dynamics (MD) employing an empirical potential. Specifically, dislocations are introduced into the β-phase at high temperatures. The system is then cooled to temperatures below the β to α phase transition temperature, and allowed to evolve. Given sufficient time, the system transforms to the α-phase. The simulations thus enable the dynamics of the transition to be studied in detail. Simulations are performed at several temperatures and the nucleation and growth rates calculated across the temperature range 1050 K to 1250 K[1].

In the simulations, the α phase initially nucleates from the β phase as plates which have an edge terminated at a dislocation core. In the very initial stages of nucleation, the habit planes of these plates are determined by the stress field of the dislocations. However, as the nuclei grow, their habit plane shifts. Further, evidence of tent-like structures and 3-variant clusters as previously reported in experiment and phase field simulations[132, 137, 138] is found. These atomic scale simulations show that existing dislocation microstructures have the potential to alter dramatically the β to α transition kinetics and morphologies.

In the following, these results are presented in more detail. Section 7.2 introduces the various methods employed, including calculation of the β to α transition temperature by non-equilibrium thermodynamic integration. Section 7.3 illustrates the predictions of Ian Winter's elasticity theory modeling and compares to the results of my MD simulations of the β to α phase transition. Next I discuss the findings for transformation rates, habit planes, and final microstructures in Section 7.4. Finally, the conclusions are presented.

---

[1]Below I show that the equilibrium $\alpha \to \beta$ transition temperature is approximately 1700 K. Hence these temperatures represent a substantial undercooling.

7.2 Methods

7.2.1 MEAM Potential Validation

Molecular dynamics calculations are performed using the Large-scale Atomic/Molecular Massively Parallel Simulator (LAMMPS)[42]. For our simulations of titanium, the modified embedded atom method (MEAM) potential for titanium of Hennig *et al.*[65] is used. The titanium potential is analyzed to determine its β to α phase transition boundary. Using a non-equilibrium thermodynamic integration technique[141], the free energies of β- and α-phases can be calculated with small errors for a range of relevant temperatures at which the phases are at least metastable. The free energies of both phases are determined from 1200 K to 2000 K at zero pressure. All simulations employ 1 fs timesteps.

Determining the free energies by non-equilibrium thermodynamic integration requires three steps. First, the spring constants for harmonic approximations to the β- and α-phases are calculated within an NPT ensemble with a Nosé-Hoover barostat and Langevin thermostat at zero pressure and 1200 K, averaged over 10 ps. For an equiaxed cell with $\sim$40,000 atoms the spring constants are 1.36 eV/$\mathring{\mathrm{A}}^2$ for β and 2.17 eV/$\mathring{\mathrm{A}}^2$ for α.

The second step is integration along the Frenkel-Ladd path[142] to find the free energy of each phase at the lower limit of the temperature range of interest, with a NVT ensemble and a Langevin thermostat set to 1200 K. The switching procedure took 20 ps and equilibrated for 4 ps. From this, the free energies at 1200 K for β- and α-phases are determined to be -5.368 eV/atom and -5.379 eV/atom, indicating that α is stable at this temperature.

Using these values as reference points, the remainder of the non-equilibrium free energy curves are determined using reversible scaling[143, 144] of the MEAM potential in the third step. Reversible scaling is done with a NPT ensemble with a Nose-Hoover barostat and a Langevin thermostat from 1200 K to 2000 K. The forward and backward simulations last 100 ps. To ensure that a sufficiently large supercell is used, the transition temperature is calculated for multiple supercell sizes. β supercells with side lengths which are multiples of 3 conventional bcc unit cells in the range $9 \times 9 \times 9$ (1458 atoms) to $30 \times 30 \times 30$ (54000 atoms) are used. For each size, a corresponding α supercell is chosen to be approximately equiaxed and have a similar number of atoms to the β supercells. The free energy curves calculated for the largest supercells are shown in Figure 7.1a, and yield a transition temperature of 1694 K. The β to α transition temperature is found to vary with supercell size, as shown in Figure 7.1, but our largest simulations indicate a value of $\sim$1700 K.

This value differs significantly from that given by Hennig *et al.* (1250 K), the creators of this MEAM potential[65], which was calculated only from homogeneous transformation from β ot α in very small supercells. Due to this discrepancy, additional coexistence calculations were undertaken to verify accuracy of the reversible scaling method calculation. In these the interface between the two phases was designed to be coherent and to reflect the elastic constants of both phases at high temperature, such that it would minimally influence phase evolution. These calculations begin with a supercell containing half α and half β titanium, meeting at an interface that satisfies the Burgers orientation relation. The elastic energy of the combined system can be expressed as

$$E = \frac{V_\alpha}{2} C^\alpha_{ijkl} \eta^\alpha_{ij} \eta^\alpha_{kl} + \frac{V_\beta}{2} C^\beta_{ijkl} \eta^\beta_{ij} \eta^\beta_{kl}, \tag{7.1}$$
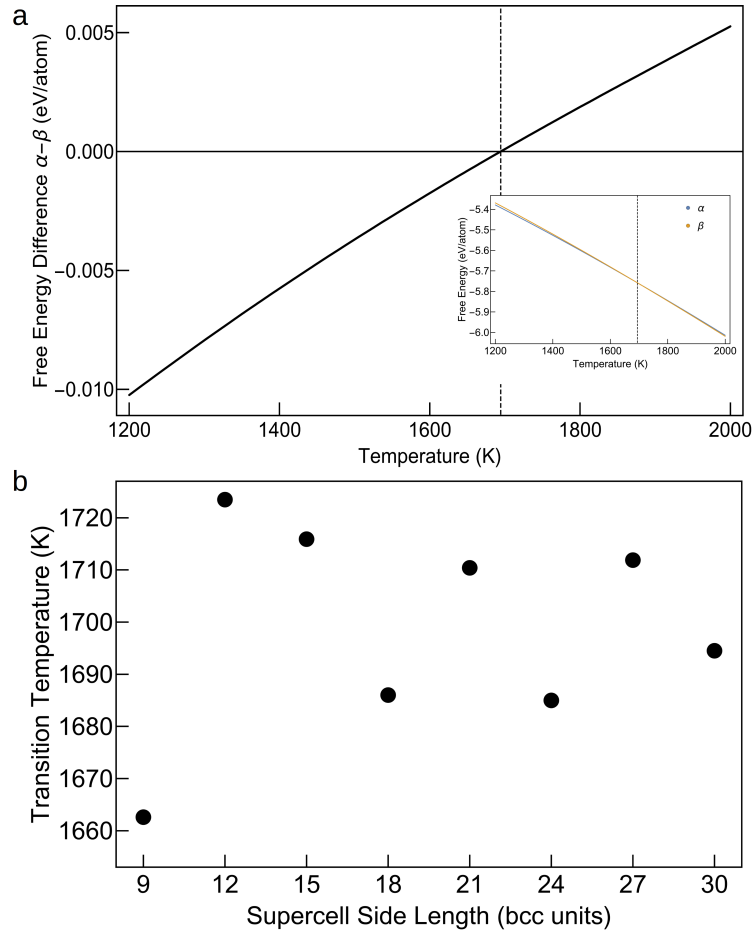
Figure 7.1: (a) Free energy difference (free energies of individual phases in inset) calculated using the reversible scaling method for the hcp and bcc phases for the $30 \times 30 \times 30$ bcc unit supercell size. (b) Variation of the transition temperature with supercell size.

where V_α (V_β) refers to the volume of the α (β) phase, $\boldsymbol{C}^\alpha$ ($\boldsymbol{C}^\beta$) corresponds to the elastic constants of the respective phases in the given frame of reference, and $\boldsymbol{\eta}_\alpha$ ($\boldsymbol{\eta}_\beta$) refers to the strain applied to the given phase. By applying the constraint that the lattice vectors parallel to the interface must match for both phases, the supercell can be constructed by solving for the strains $\boldsymbol{\eta}^\alpha$ and $\boldsymbol{\eta}^\beta$. This can be expressed as a system of equations of the following form:

$$a_0^\alpha(1 + \eta_{11}^\alpha) = a_0^\beta(1 + \eta_{11}^\beta), \tag{7.2a}$$

$$a_0^\alpha(1 + \eta_{22}^\alpha) = \sqrt{2}a_0^\beta(1 + \eta_{22}^\beta), \tag{7.2b}$$

$$\frac{\partial E}{\partial \eta_{33}^\alpha} = 0, \tag{7.2c}$$

$$\frac{\partial E}{\partial \eta_{33}^\beta} = 0, \tag{7.2d}$$

$$\frac{\partial E}{\partial \eta_{11}^\alpha} = 0, \tag{7.2e}$$

$$\frac{\partial E}{\partial \eta_{22}^\alpha} = 0, \tag{7.2f}$$

with a_0^α and a_0^β being the equilibrium lattice parameters of the α and β phases.

NPT-ensemble molecular dynamics simulations at temperatures ranging from 1200 K to 1800 K are performed using these coexistence supercells containing 17600 atoms. At temperatures 1700 K and below, the supercell transforms entirely to α. At temperatures 1712.5 K and above, the supercell transforms entirely to β. This indicates a transition temperature slightly above 1700 K, which is in excellent agreement the reversible scaling calculations.

The large difference between the temperature at which α becomes the more stable phase (1700 K) and the temperature at which β rapidly transforms to α homogeneously in very small (432 atom) supercells (1250 K) highlights the usefulness of non-equilibrium thermo-dynamic integration for potential validation. The following sections detail simulations of the β to α transition, which are performed at temperatures in the range 1050 K to 1400 K, well below the transition temperature for this potential. Unfortunately the large difference between the β to α transition temperature in this MEAM potential and that of actual titanium (1155 K[145]) means the behavior at a given temperature in our simulations cannot be directly compared to that in experiment at the same temperature. Nevertheless, one can reasonably expect that the qualitative properties of the transition will be well represented by the potential.

7.2.2 Dislocation Supercell Construction

All dislocation calculations use periodic screw dislocation arrays arranged such that each dislocation has four nearest neighbor dislocations, and is opposite in Burgers vector direction to its nearest neighbors. These arrangements are known as quadrupolar, and minimize the elastic energy of a periodic dislocation array due to cancellation of long-range stress fields[62]. The line direction of all dislocations is $[1\,1\,1]_\beta$, and therefore the Burgers vectors for the screw dislocations are $\pm\frac{a_0}{2}[1\,1\,1]_\beta$. Dislocation-containing supercells are oriented such that $[1\,1\,\bar{2}]_\beta$ is parallel to the x-axis, the line direction/Burgers vector $[1\,1\,1]_\beta$ is parallel to the y-axis, and $[\bar{1}\,1\,0]_\beta$ is parallel to the z-axis. Supercell lattice vectors are tilted to account for the distortion from the dislocations as prescribed by Lehto and Öberg[63]. Initial displacements

are determined using the method of Daw[62], which yields good starting points that account for elastic anisotropy while only requiring lattice parameters and elastic constants as inputs.

The quadrupolar arrangement used in this paper had dislocations of alternating sign on the $\left(\bar{1}\,1\,0\right)_\beta$ and $\left(1\,1\,\bar{2}\right)_\beta$ planes (i.e. along the x and z directions). The superlattice vectors in these directions are 244 Å and 141 Å. For the majority of the calculations presented the superlattice vector along the dislocation line direction is 46 Å and the supercell contained 86,400 atoms.

Stabilization of the dislocations within the supercell proved to be challenging. The positions produced from our linear elasticity method resulted in nearly immediate annihilation of the dislocations at any simulated temperature. Relaxation of the positions at 0 K can often solve this type of issue, but β-Ti is not stable at 0 K. To get around these issues, I scaled the lattice vectors and atomic coordinates to those of tungsten, and relaxed the supercell to a force tolerance of 10^{-4} eV/Å within a tungsten Finnis-Sinclair EAM potential[146] for which bcc is the stable phase from 0 K to at least 1350 K. With the relaxed cell and still within the tungsten potential, an NPT ensemble with a Nose-Hoover barostat and Langevin thermostat set at 0 pressure and 1350 K is used to achieve an equilibrated state over 100 ps. This equilibrated configuration is then scaled to the lattice parameters of titanium (estimated via molecular dynamics without dislocations) and the atoms converted to Ti.

Structural analysis of the dislocation cells before and after transformation is performed using the OVITO software package[85]. Chiefly the polyhedral template matching (PTM)[18] tool is used to identify the local structure as well as orientation at each atomic site. Averaging of the atomic coordinates over 100 fs is performed within LAMMPS to smooth thermal vibrations and allow for PTM calculation.

7.3 Results

7.3.1 Elasticity Theory Analysis

This subsection contains work that was chiefly performed by Ian Winter, though the current formulation and results are my own. I am presenting this elasticity theory model because it forms a key point of comparison with my MD simulations in this chapter.

The prediction of variant selection from elasticity theory is not a new idea. Cahn used isotropic elasticity theory to analyze the nucleation of second phases on dislocations[147], while Thomas and Nutting proposed that the preferred variants to nucleate from a dislocation are those that best accommodate the strain field of a dislocation[148]. More recently, Qiu *et al.* considered the variant selection of α precipitates nucleating from both edge and screw dislocations in β-Ti using both anisotropic elasticity theory and phase field modeling[138]. They found that during nucleation the preferred variants are those with the most negative elastic interaction energy associated with the strain field of the dislocation. However, they saw that the most dominant variants in growth were those for which the habit plane was oriented nearly parallel with the dislocation line, an idea first proposed by Kelly and Nicholson[149].

Here, only the preferential nucleation of variants on the dislocation are considered. These variants will have the geometry imposed by our few-layer supercells, and therefore make for a

good point of comparison. This geometry also represents the observations in the early stages of nucleation in our many-layer supercells. As a result, an approach similar to Thomas and Nutting's proposed mechanism of variant selection is used in an anisotropic elasticity model to identify the variants most likely to nucleate from a screw dislocation in β-Ti, with the strain field of the straight $\langle 1\ 1\ 1 \rangle_\beta$-type dislocation generated from continuum anisotropic linear elasticity theory[150].

Burgers Transformation Path

The Burgers path consists of both a strain and shuffling of atoms[127]. The shuffling of atomic $\{1\ 1\ 0\}_\beta$ planes is associated with the N-point phonon while the transformation strain can be represented as eigenstrains for the orientations $\boldsymbol{a} = \langle 1\ 1\ 0 \rangle_\beta$, $\boldsymbol{b} = \langle 0\ 0\ 1 \rangle_\beta$, and $\boldsymbol{c} = \langle 1\ \bar{1}\ 0 \rangle_\beta$. The eigenstrains consist of a compressive strain along $\langle 0\ 0\ 1 \rangle_\beta$ and a tensile strain along $\langle 1\ 1\ 0 \rangle_\beta$. The Burgers transformation results in the α/β orientation relation $\{1\ 1\ 0\}_\beta || (0\ 0\ 0\ 1)_\alpha$ (see Table 7.1 for all variants).

The lattice parameter of β-Ti is found to be $a_\beta = 3.32$ Å at 1200 K, while the lattice parameters for the α phase are estimated to be $a_\alpha = 2.97$ Å and $c_\alpha = 4.77$ Å. The Lagrangian strain is written in Einstein summation notation as

$$\varepsilon_{jk} = \frac{1}{2}\left(F_{mj}F_{mk} - \delta_{jk}\right). \tag{7.3}$$

Here $\boldsymbol{F}$ is the deformation gradient, defined as $F_{mj} = \frac{\partial x_m}{\partial X_j}$ ($\boldsymbol{x}$ corresponds to the current configuration and $\boldsymbol{X}$ the reference configuration), and δ_{jk} is the Kronecker Delta. Setting the lattice vectors of the reference frame to be those defined above, the transformation strain is

$$\boldsymbol{\varepsilon}^T = \begin{pmatrix} 0.101 & 0 & 0 \\ 0 & -0.099 & 0 \\ 0 & 0 & 0.016 \end{pmatrix}. \tag{7.4}$$

Dislocation Induced Nucleation

To predict the variants that will nucleate on the dislocation and the orientations along which they will grow, a comparison was made between the strain associated with the Burgers transformation path and the stress field resulting from a single $\langle 1\ 1\ 1 \rangle_\beta$-type dislocation a distance r_{core} away from the center of the dislocation, with r_{core} being an estimate for the dislocation core radius using elasticity theory[151]. This was done by calculating the elastic energy density, taking into consideration the orientation of the α nucleus to the dislocation as well as the orientation relationship between the β and α phases. As shown in Table 7.1, there exist 12 unique variants associated with the Burgers transformation between the β and α phases[127, 152]. With respect to the nucleation of a general α precipitate, there are six unique habit planes in the β phase for which there are two unique variants. These two variants are related by a $\frac{\pi}{2}$ rotation perpendicular to the habit plane. The elastic interaction between an Eshelby inclusion with strain equal to the Burgers transformation strain for

variant n (Equation 7.4) and the stress induced by a $[1\ 1\ 1]_\beta$-type screw dislocation as a function of angle θ around the dislocation ($\theta = 0$ corresponds to the direction $[1\ 1\ \bar{2}]_\beta$ and $\theta = \frac{\pi}{2}$ to the direction $[1\ \bar{1}\ 0]_\beta$) can be assessed by computing the energy density $e_n^{int}(\theta)$, following Qiu *et al.*[138]:

$$e_n^{int}(\theta) = -\sigma_{ij}(\theta)\epsilon_{ij}^0(V_n) \tag{7.5}$$

here $\boldsymbol{\sigma}(\theta)$ is the strain induced by the screw dislocation at radius $r_{core} = 5.90$ Å from the dislocation origin and $\epsilon_{ij}^0(V_n)$ is the Burgers transformation strain associated with the nth variant.

Table 7.1: List of the 12 unique variants for the Burgers orientation between the α and β precipitates[127, 152].

Variant	Plane Relation	Direction Relations	
V1	$(1\ 1\ 0)_\beta \parallel (0\ 0\ 0\ 1)_\alpha$	$[\bar{1}\ 1\ \bar{1}]_\beta \parallel [1\ 1\ \bar{2}\ 0]_\alpha$	$[\bar{1}\ 1\ 2]_\beta \parallel [\bar{1}\ 1\ 0\ 0]_\alpha$
V2	$(1\ 1\ 0)_\beta \parallel (0\ 0\ 0\ 1)_\alpha$	$[\bar{1}\ 1\ 1]_\beta \parallel [1\ 1\ \bar{2}\ 0]_\alpha$	$[\bar{1}\ 1\ \bar{2}]_\beta \parallel [\bar{1}\ 1\ 0\ 0]_\alpha$
V3	$(\bar{1}\ 1\ 0)_\beta \parallel (0\ 0\ 0\ 1)_\alpha$	$[1\ 1\ \bar{1}]_\beta \parallel [1\ 1\ \bar{2}\ 0]_\alpha$	$[1\ 1\ 2]_\beta \parallel [\bar{1}\ 1\ 0\ 0]_\alpha$
V4	$(\bar{1}\ 1\ 0)_\beta \parallel (0\ 0\ 0\ 1)_\alpha$	$[1\ 1\ 1]_\beta \parallel [1\ 1\ \bar{2}\ 0]_\alpha$	$[1\ 1\ \bar{2}]_\beta \parallel [\bar{1}\ 1\ 0\ 0]_\alpha$
V5	$(0\ 1\ 1)_\beta \parallel (0\ 0\ 0\ 1)_\alpha$	$[\bar{1}\ \bar{1}\ 1]_\beta \parallel [1\ 1\ \bar{2}\ 0]_\alpha$	$[\bar{2}\ 1\ \bar{1}]_\beta \parallel [\bar{1}\ 1\ 0\ 0]_\alpha$
V6	$(0\ 1\ 1)_\beta \parallel (0\ 0\ 0\ 1)_\alpha$	$[1\ \bar{1}\ 1]_\beta \parallel [1\ 1\ \bar{2}\ 0]_\alpha$	$[2\ 1\ \bar{1}]_\beta \parallel [\bar{1}\ 1\ 0\ 0]_\alpha$
V7	$(0\ \bar{1}\ 1)_\beta \parallel (0\ 0\ 0\ 1)_\alpha$	$[\bar{1}\ 1\ 1]_\beta \parallel [1\ 1\ \bar{2}\ 0]_\alpha$	$[2\ 1\ 1]_\beta \parallel [\bar{1}\ 1\ 0\ 0]_\alpha$
V8	$(0\ \bar{1}\ 1)_\beta \parallel (0\ 0\ 0\ 1)_\alpha$	$[1\ 1\ 1]_\beta \parallel [1\ 1\ \bar{2}\ 0]_\alpha$	$[\bar{2}\ 1\ 1]_\beta \parallel [\bar{1}\ 1\ 0\ 0]_\alpha$
V9	$(1\ 0\ 1)_\beta \parallel (0\ 0\ 0\ 1)_\alpha$	$[\bar{1}\ 1\ 1]_\beta \parallel [1\ 1\ \bar{2}\ 0]_\alpha$	$[1\ 2\ \bar{1}]_\beta \parallel [\bar{1}\ 1\ 0\ 0]_\alpha$
V10	$(1\ 0\ 1)_\beta \parallel (0\ 0\ 0\ 1)_\alpha$	$[\bar{1}\ \bar{1}\ 1]_\beta \parallel [1\ 1\ \bar{2}\ 0]_\alpha$	$[1\ \bar{2}\ \bar{1}]_\beta \parallel [\bar{1}\ 1\ 0\ 0]_\alpha$
V11	$(\bar{1}\ 0\ 1)_\beta \parallel (0\ 0\ 0\ 1)_\alpha$	$[1\ \bar{1}\ 1]_\beta \parallel [1\ 1\ \bar{2}\ 0]_\alpha$	$[1\ 2\ 1]_\beta \parallel [\bar{1}\ 1\ 0\ 0]_\alpha$
V12	$(\bar{1}\ 0\ 1)_\beta \parallel (0\ 0\ 0\ 1)_\alpha$	$[1\ 1\ 1]_\beta \parallel [1\ 1\ \bar{2}\ 0]_\alpha$	$[1\ \bar{2}\ 1]_\beta \parallel [\bar{1}\ 1\ 0\ 0]_\alpha$

Plotting all twelve unique variants (Figure 7.2) it is apparent that there is an absolute minimum value that is obtained by three variants. The orientations at which a variant displays an absolute minimum are: variant 4 at $\frac{\pi}{2}$, variant 8 at $\frac{7\pi}{6}$, and variant 12 at $\frac{11\pi}{6}$. These are also the three variants that satisfy the additional constraint proposed by Kelly and Nicholson[149] that the Burgers vector in the β phase is contained by the α habit plane (i.e. $[1\ 1\ 1]_\beta \parallel [1\ 1\ \bar{2}\ 0]_\alpha$). Therefore there are three potential variants favored to nucleate from the screw dislocation: V4 at $\frac{\pi}{2}$, V8 at $\frac{7\pi}{6}$, and V12 at $\frac{11\pi}{6}$. These three variant and orientation pairs are the same as those along which α precipitates are shown to nucleate in MD simulations. If the sign of the dislocation Burgers vector is reversed in

the calculation the same three variants are found to be favored, but with minima rotated by π, also in agreement with our MD simulations. All inputs used for the dislocation strain field calculation $(a_\beta, C_{11}, C_{12}, C_{44})$ were calculated for β-Ti at 1200 K. See the Section 7.2 for further details.
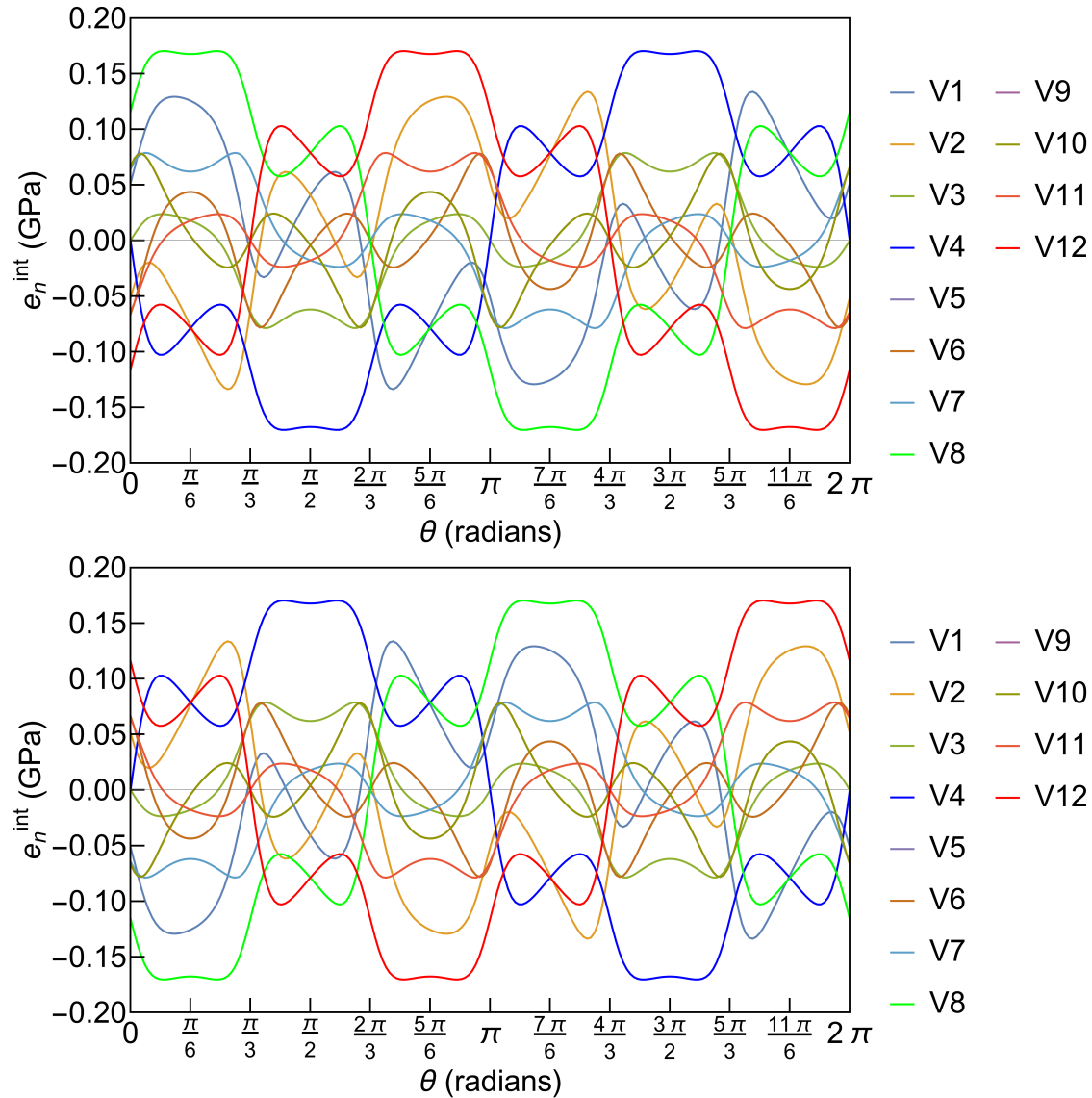
Figure 7.2: (Top) Plot of penalty function $\Pi_n(\theta)$ with respect to direction symbolized by the angle θ. The absolute minima occur at $\frac{\pi}{2}$, $\frac{7\pi}{6}$, and $\frac{11\pi}{6}$ in agreement with molecular dynamics simulations; the secondary minima are at $\frac{\pi}{6}$, $\frac{5\pi}{6}$, and $\frac{3\pi}{2}$. $\theta = 0$ corresponds to the direction $[1\,1\,\bar{2}]_\beta$ and $\theta = \frac{\pi}{2}$ to the direction $[1\,\bar{1}\,0]_\beta$. (Bottom) Same plot, but for opposite Burgers vector sign. The same variants are favored, but with a rotation by π.

7.3.2 Few-Layer Supercell Molecular Dynamics

Molecular dynamics simulations of the β to α phase transition begin with a β supercell with 16 layers along the dislocation line (86,400 atoms). Starting with both a reference undeformed supercell and a stabilized titanium supercell containing two dislocations, MD simulations are performed with an NPT ensemble using a Nosé-Hoover barostat and Langevin thermostat at zero pressure and temperatures of 1050 K, 1200 K, 1225 K, 1250 K, 1275 K, 1300 K, 1350 K, and 1400 K. For each cell at each temperature ten independently-seeded simulations 500 ps in length are performed, for a total of 160 simulations in this group.

A typical simulation result is shown in Figure 7.3. The visualization presented is from OVITO. PTM is used first to identify a local crystal structure at each atom, using a root-mean-squared deviation (RMSD) cutoff of 0.09 (i.e. atoms above this threshhold are identified as "other" and colored white). The atoms found to be bcc are then colored black. For the atoms identified as hcp, the coloring is by the y-component of the orientation identified by PTM. This is very useful for distinguishing the α variants. An undocumented bonus-feature of PTM exists for the hcp crystal structure. Because there are two basis atoms in hcp, two slightly different orientations are identified within the same grain, alternating on adjacent basal planes. This leads to a striped appearance in our visualizations that allows us to easily identify basal planes. In this color scheme variant 4 appears blue, variant 8 is yellow-green, and variant 12 is red.

Examining all trials, there are three dominant variants (V4, V8, and V12) of α grains, in agreement with our elasticity theory prediction. The angles at which these variants appear are also in agreement with our prediction. Examples of all orientations are shown in Figure 7.4. It is worth noting that because the two dislocations have oppositely signed Burgers vectors, the direction in which each variant nucleates is rotated by π when considering the right-hand dislocation (Burgers vector into page) vs. the left-hand dislocation (Burgers vector out of page).

Using PTM through OVITO, one can extract both phase and orientation information over time rapidly from all our simulations. Figure 7.5 shows the fraction of atoms identified as belonging to each variant type for the same simulation as shown in Figure 7.3. At approximately 50 ps the primary V8 nuclei form, followed quickly by secondary nuclei of the other two dominant variants. Transformation to α is complete at 100 ps. Following this, growth of V12 grains at the expense of V4 leads to the coarse structure seen in Figure 7.3f.

Taking the total fraction of hcp atoms I fit the growth to the following Avrami-type equation[153–155]:

$$
\begin{cases}
0 & t < t_{het} \\
\alpha_{max}(1 - \exp{-(\frac{t-t_{het}}{\tau})^3}) + N_0 & t \geq t_{het}
\end{cases}
\tag{7.6}
$$

to find the characteristic growth time (τ). This fit is shown for our example simulation in Figure 7.6. In the fit, I allow also fit the nucleation time before rapid growth begins, which yields a good estimate of the time to heterogeneous nucleation (t_{het}). α_{max} is the (known) maximum fraction of the supercell which is transformed to α (0.5% to 5% of the supercell is identified as having no phase or remaining β after transformation). N_0 is a small offset allowed in the fit, and is less than 10^{-5} in all samples.

In the simulations starting from the configuration containing dislocations, transformation

to α in all trials at temperatures 1250 K and below is observed. At 1275 K two trials transform, while the other eight remain in the β phase. At temperatures 1300 K and above all trials remain in the β phase. The results of fits for all simulations at 1050 K, 1200 K, 1225 K, and 1250 K are summarized in Table 7.2. When simulations are started from the configuration without dislocations, transformation is only observed at 1050 K, demonstrating the necessity of heterogeneous nucleation sites to induce transformation.

Table 7.2: Heterogeneous nucleation time t_{het} and transformation characteristic time τ from Avrami equation fits to data from simulations containing dislocations.

Temperature	1050 K	1200 K	1225 K	1250 K
t_{het} (ps)	1.95 ± 0.86	18.5 ± 3.7	36.4 ± 14.0	104.3 ± 30.0
τ (ps)	8.3 ± 1.0	16.2 ± 1.8	20.3 ± 2.3	22.5 ± 1.6

From the simulations of the supercell without dislocations I measure t_{hom}, the homogeneous equivalent to t_{het}. At 1050 K, t_{hom} is 91.8 ± 51.0 ps, which is both much longer and much more varied than the heterogeneous case at the same temperature. This demonstrates the potency of the dislocation lines as heterogeneous nucleation sites. In fact, the nucleation behavior without dislocations at 1050 K is similar to that with dislocations at 1250 K. In terms of growth rate, τ at 1050 K without dislocations is 9.1 ± 1.2 ps, which is similar to but a bit slower than the rate with dislocations. This indicates that the strain from the dislocation may provide a boost to the α phase growth rate.

7.3.3 Many-Layer Supercell Molecular Dynamics

Following the procedure detailed in Section 7.2 for stabilizing dislocations in high temperature β-Ti, I created a new supercell with 256 layers along the dislocation line direction and the same area on the face normal to this direction as used previously, with a total of 1,382,400 atoms. This supercell is much longer along the line direction (737 Å) than the separation between the dislocations (183 Å). Nucleation of the α phase in this supercell is observed in two molecular dynamics simulations at 1250 K with NPT ensemble configured as described previously. Early in this process it is apparent that various small proto-nuclei form, fail to reach critical radius, and disappear. These nucleate with the same orientations as observed in the shorter supercells, but do not span the entire length of the simulation cell. It is also noteworthy that while all three possible orientations are sometimes present on the same dislocation line, they are not observed at the same point along the line at the same time. This is likely due to the elastic field around a nucleus making formation of a nearby nucleus of differing orientation on the dislocation line less favorable.

While I was not able to conduct enough simulations to facilitate a detailed statistical analysis, it is clear that the nucleation rate (of supercritical nuclei) in the long supercells is lower than in the short supercell at the same temperature. Fitting to the Avrami equation yields nucleation times of 134 ps and 139 ps for the two samples, which are both approximately one standard deviation longer than for the few-layer supercell at the same temperature. The

characteristic growth times are 37.9 ps and 30.8 ps, which indicates much slower growth than in the short supercells. In the short supercell once a proto-nucleus is formed it need not grow very far before it runs into its own image through a periodic boundary and at this point its length becomes effectively infinite. When the superlattice vector along the line direction is larger than the critical nucleus size, the nuclei exist for much longer before this occurs. During this stage the surface energy due to the nucleus surfaces normal to the dislocation line direction increase the energy of the nucleus. Furthermore, as a nucleus grows along the dislocation line it must compete with nuclei of other orientations that it encounters, as it is unfavorable for two nuclei of differing orientations to exist in the same region of the dislocation line at the same time. This progression can be observed in Figure 7.7. [2]

7.4 Discussion

7.4.1 Nucleation Times and Transformation Rates

The increase in time to a successful α nucleation event with increasing temperature is significant. Over the range 1200 K to 1250 K the increase is 5×. On the other hand, the change in this time with respect to supercell length is small. In the many-layer supercells, the time to form a supercritical nucleus is slightly longer than in the few-layer supercells. Probably this is due to competition between two factors: (1) there is 16× more dislocation line length on which to form a nucleus, which ought to increase the rate and (2) the size of a supercritical nucleus is larger, because the nuclei do not immediately cross the periodic boundaries and contact themselves.

In the few-layer supercells, growth rates drop consistently as temperature increases due to the lower driving force to form α. The growth rate in the many-layer supercell is much slower. This results from competition between neighboring nuclei with different orientations on the same dislocation line, as well as the increase in surface area of the nuclei due to their curved edges before they completely fill the supercell. It also appears that there is little growth of the nuclei while they change in habit plane and pull away from parts of the dislocation. In fact, there is some local shrinkage of supercritical nuclei where they pull away from the dislocation line.

The success of Equation 7.6 in fitting the nucleation and growth data (as shown in Figure 7.6) is mildly surprising, as the model was derived to represent homogeneous nucleation and growth at a constant rate. In our simulations (other than that without dislocations at 1050 K) the observed nucleation is plainly heterogeneous on the dislocation lines. However, nucleation does not end there. Strain-induced nucleation of secondary grains adjacent to the primary grains allows the growth to continue at a greater rate than if only primary nucleation on the dislocation lines occurred. However, this is still not truly homogeneous nucleation because it is induced only within a range (approximately 30 Å) of existing nuclei. On the other hand, these secondary nuclei induce more secondary nuclei to form, and thus can spread the α phase rapidly. Therefore while primary nucleation is heterogeneous on dislocation lines only, secondary nucleation events occur throughout the supercell.

---

[2]The full trajectory data is available via the UC Berkeley Library Dash project at https://doi.org/10.6078/D1QS94.

7.4.2 Habit Plane Analysis

In the few-layer geometry the length of the supercell along the dislocation line direction is as short as possible (without altering the transition temperature significantly, see Figure 7.1) so that the separation between the dislocations can be maximized within resource limitations. This effectively fixes the line direction of the dislocations, which is generally acceptable because the line direction has been chosen to be one known to be common in the material. In the case of phase nucleation along the dislocation in Ti this also imposes the undesirable condition that the habit plane of the nucleus contains the chosen line direction. However, there is no *a priori* reason to expect the elastically preferred habit plane to be perpendicular to the $\langle 1\,1\,1 \rangle_\beta$ family of directions, and in fact there is evidence to suggest that it is not. Kashchenko and Chashchina predicted from elasticity theory that for pure Ti this habit plane should be $\{\bar{1}\,1.5356\,\bar{1}\}_\beta$[156], and Morris *et al.* made a similar prediction in a titanium alloy[157]. This habit plane normal is clearly not perpendicular to the dislocation line direction $[1\,1\,1]_\beta$, unlike the $\{\bar{1}\,2\,\bar{1}\}_\beta$ habit plane observed in the few-layer simulations.

In the many-layer supercells, as in the few-layer supercells, the precipitates are plate-like and begin with $\{\bar{1}\,2\,\bar{1}\}_\beta$ type habit planes (see Figure 7.7a). However, in the longer cells most of these plates change growth direction to alter the habit plane during growth of the supercritical nuclei, gliding portions of the dislocations with them (as done by one of the plates in Figure 7.8). This shifts the habit plane from $\{\bar{1}\,2\,\bar{1}\}_\beta$ to approximately $\{\bar{1}\,1.61\,\bar{1}\}_\beta$ before the transformation proceeds too far to allow habit plane identification. This rotation is towards the direction predicted by elasticity theory calculations[156, 157], but still limited by the periodic boundary conditions. Because the dislocation line must be periodic, a section of it glides to connect the twisted line to its image (see Figure 7.8b), and the energy associated with this increase in line length resists the rotation caused by the precipitate. At the slipped segment the precipitate detaches from the dislocation line, forming a curved edge. I anticipate that if the supercell was infinitely long the precipitate would rotate all the way into the habit plane predicted by elasticity theory.

7.4.3 Post-Transformation Microstructure

After the transformation is complete the resulting microstructure is necessarily nano-grained, due to the supercell size. In our few-layer simulations all primary α grains have the orientation relationship $[1\,1\,1]_\beta \parallel [1\,1\,\bar{2}\,0]_\alpha$ maintained along the short axis of the supercell parallel to the dislocation line. Initially many secondary α grains are nucleated, and a very small fraction of these do not share this orientation relation (see "Other" data in Figure 7.5). However, during growth all of those without this relationship eventually are consumed by grains of the three dominant variants (V4, V8, V12). Further, many grains of these dominant variants are also consumed by others during coarsening after the transformation to α is complete.

I characterize boundaries between different grains by the angle between c-axes ($[0\,0\,0\,1]_\alpha$ directions) in the adjacent grains and the angle the grain boundary makes with both c-axes. Due to the constrained supercell geometry, all rotations are about the $[1\,1\,\bar{2}\,0]_\alpha$ axis. I find only three distinguishable orientations of the basal plane and five grain boundary types, which I will describe in descending order of occurrence.

The most common boundary (type 1) has $[0\ 0\ 0\ 1]_\alpha$ directions at an angle of $\frac{\pi}{3}$, with the boundary at $\frac{\pi}{6}$ to each, and the boundary is a plane of mirror symmetry. This finding is consistent with previous experiment[132, 137] and phase field simulations[138]. Type 2 is a boundary (stacking fault) at which the hcp stacking changes (ABA|B|CBC). In this type there is no difference in angle between the $[0\ 0\ 0\ 1]_\alpha$ directions, and both $[0\ 0\ 0\ 1]_\alpha$ directions make an angle of $\frac{\pi}{2}$ with the grain boundary. These appear as green lines in the PTM images due to the local structure in the boundary layer being identified as fcc. Type 3 boundaries have c-axes at $\frac{\pi}{3}$ as in type 1, but the boundary itself is perpendicular with the c-axis on one side of the boundary. Type 3 boundaries are asymmetric and tend to be shorter and broader (i.e. more atoms are identified as in the boundary rather than either of the neighboring grains), indicating that its energy is somewhat higher than the previous two types. The last two observed grain boundaries are much less common than the first three. In type 4 the c-axes meet at a $\frac{2\pi}{3}$ angle, with the grain boundary at $\frac{\pi}{3}$ to each. In type 5, the adjacent grains differ by stacking rather than angle as in type 2, but both c-axes meet the grain boundary at a $\frac{\pi}{6}$ angle.

Examining the simulation trajectories during the grain growth stage, the commonly-observed type 1 grain boundaries often form when a new grain nucleates only a few atomic spacings from an existing α grain (see Figure 7.3b,c). This nucleation is apparently accommodated by the stress in the β grain resulting from the nearby α-β interface. Further, it is common to see two nearby α grains with $\frac{\pi}{3}$ difference in orientation induce the nucleation of a grain oriented to form $\frac{\pi}{3}$ angles with both (see Figure 7.3d). This results in structures similar to the tents seen by Balachandran *et al.* in EBSD[137] as well as Qiu *et al.* in in phase field simulations[138].

After coarsening is complete typically only type 1 boundaries between distinguishable orientations, type 2 boundaries (stacking faults) within grains, and some geometrically-necessary type 5 boundaries which connect the type 2 stacking faults. In many cases coarsening results in only two large grains surviving (see Figure 7.3f), while as many as 30 grains might exist at some point during a simulation.

In the many-layer supercells when the transformation is near completion the same types of grain boundaries are observed as in the few-layer supercells (see Figure 7.7b), with a similar columnar structure. Again the dominant boundary is the symmetric type 1 and the type 2 is the next most common. A large triple junction of symmetric $\frac{\pi}{3}$ boundaries has been observed to form when two grains grow into each other and induce a third grain to nucleate, as similarly observed in the short supercells. This in some cases creates tent-like structures formed when these three grains grow inwards toward the triple junction, a process shown in Figure 7.9. Nearly all grain boundaries are parallel to the original dislocation line direction, though type 2 boundaries are formed at a $\frac{\pi}{3}$ angle to the dominant grain boundary direction towards the end of the grain growth process.

7.5 Conclusion

Nucleation of the β to α phase transition at $\langle 1\ 1\ 1 \rangle_\beta$-type screw dislocations in pure titanium was examined through a combination of molecular dynamics simulation using a modified embedded atom method potential and elasticity theory analysis. Both methods

predict the same three α variants and preferential directions for α nucleus growth in the early stages of transformation, corresponding to orientations spaced uniformly about the $\langle 1\ 1\ 1 \rangle_\beta$ axis at angles $\theta = \frac{\pi}{2}$, $\theta = \frac{7\pi}{6}$, and $\theta = \frac{11\pi}{6}$ from the $\langle \bar{2}\ 1\ 1 \rangle_\beta$ axis perpendicular to the dislocation. These directions are preferred because the strain field resulting from the dislocation aligns best with the transformation strain required for the Burgers path that takes the β phase to the α phase and result in habit planes that contain the dislocation line.

The tendency of the α precipitate to rotate towards the elastically preferred habit plane has been demonstrated when the simulation supercell is large enough to accommodate such a rotation. This rotation is still apparently resisted by lengthening of the remaining dislocation, to which the α precipitate remains bound by a favorable surface energy term. Finally, the post-transformation α microstructure is dominated by three orientation relationships between neighboring grains.

This work demonstrates the role of the strain field around $\langle 1\ 1\ 1 \rangle_\beta$-type screw dislocations in providing heterogeneous nucleation sites for the α phase, and thus provides a link between initial dislocation density in the β phase and post-transformation microstructure that could prove useful to the engineering of titanium alloys. These findings match those from experimental and phase-field simulation literature on the same system. In addition, these findings extend those deduced from phase-field simulations by enabling the time scales associated with nucleation to be explored directly. Within molecular dynamics simulations, the processes determining nucleation rates are allowed to evolve at the atomic scale. Moreover, the molecular dynamics simulations allow for the motion of the dislocation that accommodates the habit plane shift after nucleation. This demonstrates the potential of molecular dynamics simulations for studying variant selection in solid/solid phase transitions.
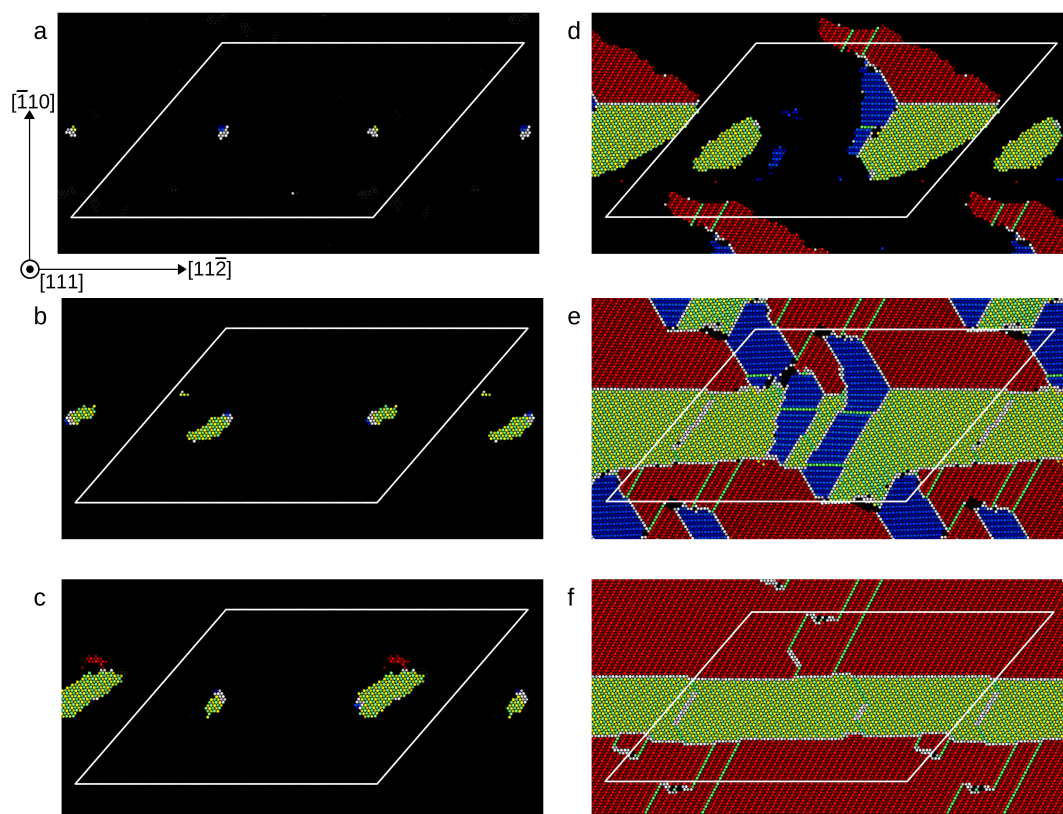
Figure 7.3: Nucleation and growth of the α phase (colored atoms) from the β phase (black) at 1225 K viewed in the plane perpendicular to the dislocation line direction. Coloring is by PTM as described above. White atoms have no identified structure in PTM within the RMSD cutoff of 0.09, and correspond to dislocations, grain boundaries, or point defects. (a) 0 ps: initial dislocation cell, (b) 20 ps: initial nucleation of α phase at each dislocation, (c) 40 ps: growth of primary nuclei and formation of a secondary nucleus adjacent to the right-hand nucleus, (d) 60 ps: continued growth and formation of secondary nucleus complementary to the primary and previous secondary nuclei, (e) 80 ps: completed growth of fine-grained α, (f) 500 ps: coarsening has occured and removed all high-energy grain boundaries.
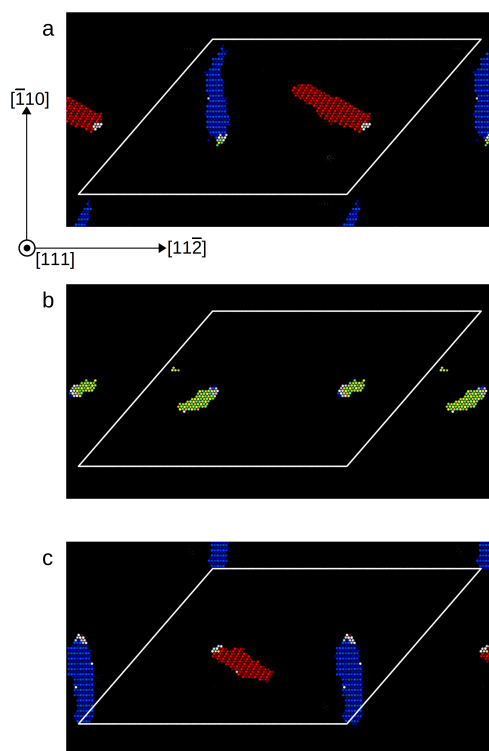
Figure 7.4: Examples of all three dominant orientations nucleating on both the left-hand and right-hand dislocations. Coloring is by PTM as described above.

Figure 7.5: Atom fraction of α V4, V8, V12, and other (i.e. hcp atoms not matching any of the three dominant variants) for the simulation at 1225 K shown in Figure 7.3.

Figure 7.6: Avrami equation fit (black line) to α phase nucleation and growth data (blue points) for the simulation at 1225 K shown in Figure 7.3.

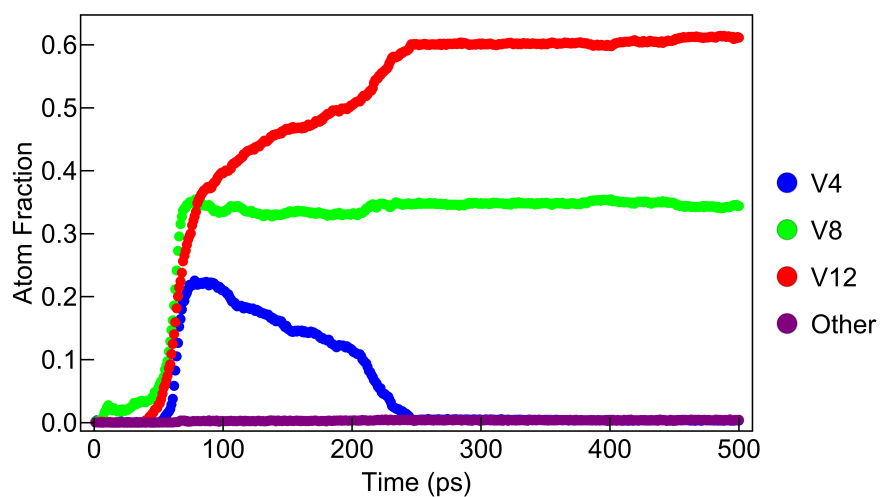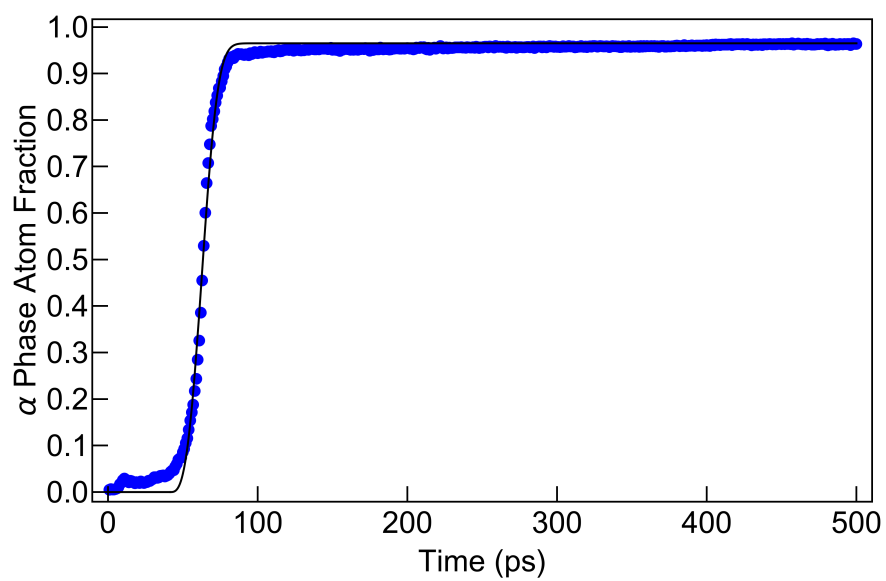**Figure 7.7:** Front view of nucleation and growth of the α-phase from β (atoms removed) at 1250 K along the $[111]_\beta$ screw dislocation lines in the supercell which is 737 Å in length. Atom coloring is by PTM as described previously. (a) Configuration 40 ps into simulation, shows single nucleus on left-hand dislocation and a number of smaller nuclei on the right-hand dislocation. These occupy different segments of the line in the direction into the page. (b) Post-transformation microstructure 210 ps into simulation. The somewhat columnar structure is similar to that found in the few-layer supercells, though not all grains completely fill the length of the supercell.

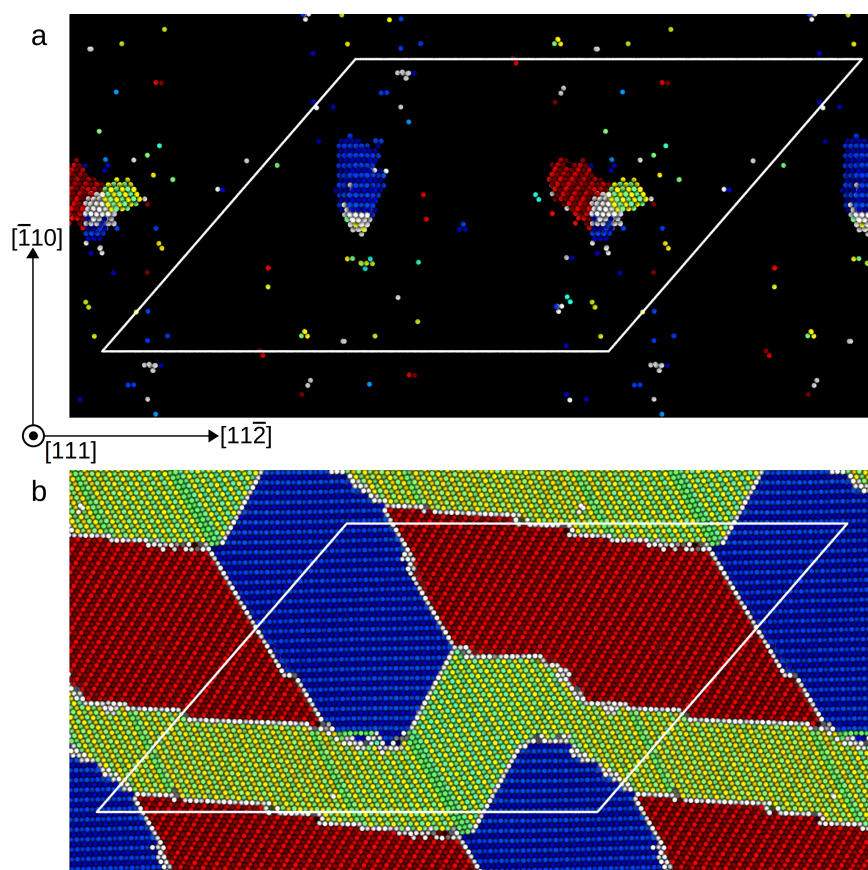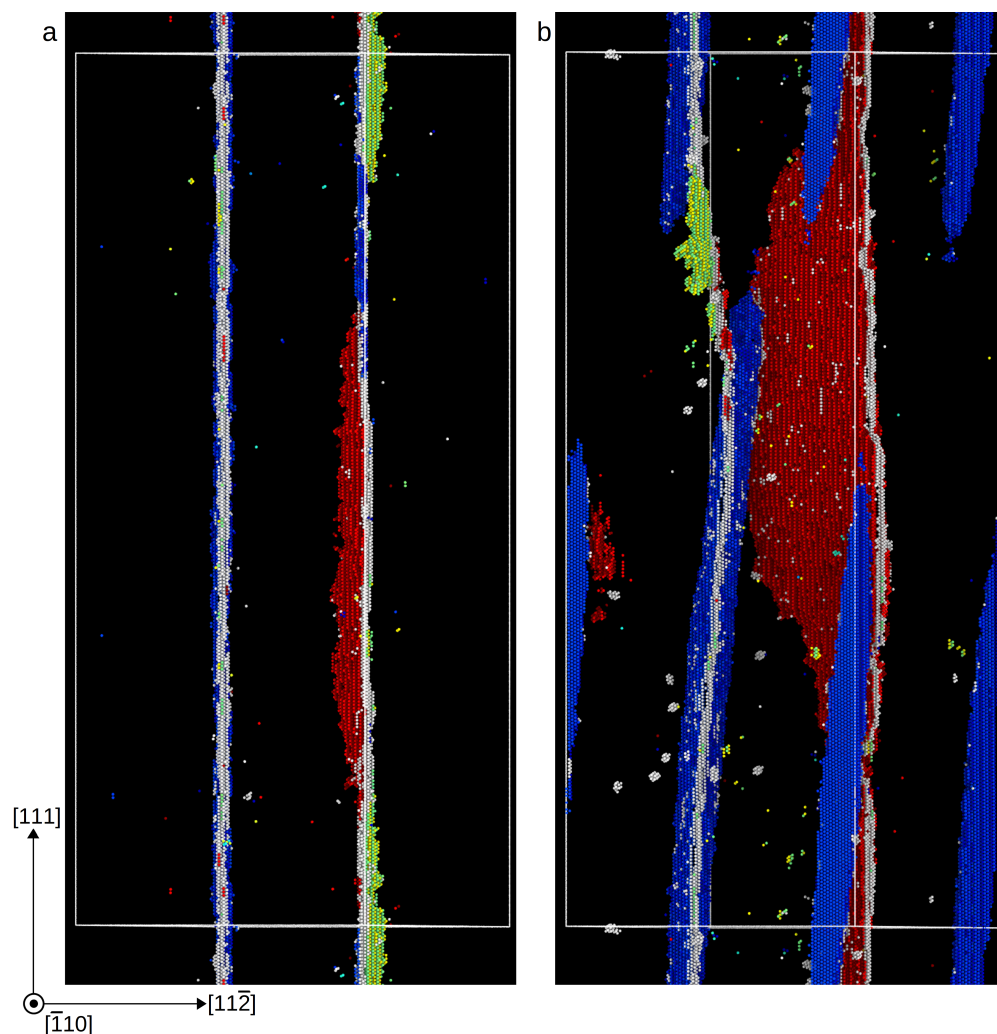**Figure 7.8:** Bottom view of nucleation and growth of the α-phase from β (atoms removed) at 1250 K along the $[111]_\beta$ screw dislocation lines in the supercell which is 737 Å in length. Atom coloring is by PTM as described previously. (a) Configuration 40 ps into simulation, shows single nucleus on left-hand dislocation and a number of smaller nuclei on the right-hand dislocation. (b) 150 ps into simulation. This view most clearly shows the change of habit plane by the left-hand nucleus, and how this leads to detachment of part of the nucleus from the dislocation line.
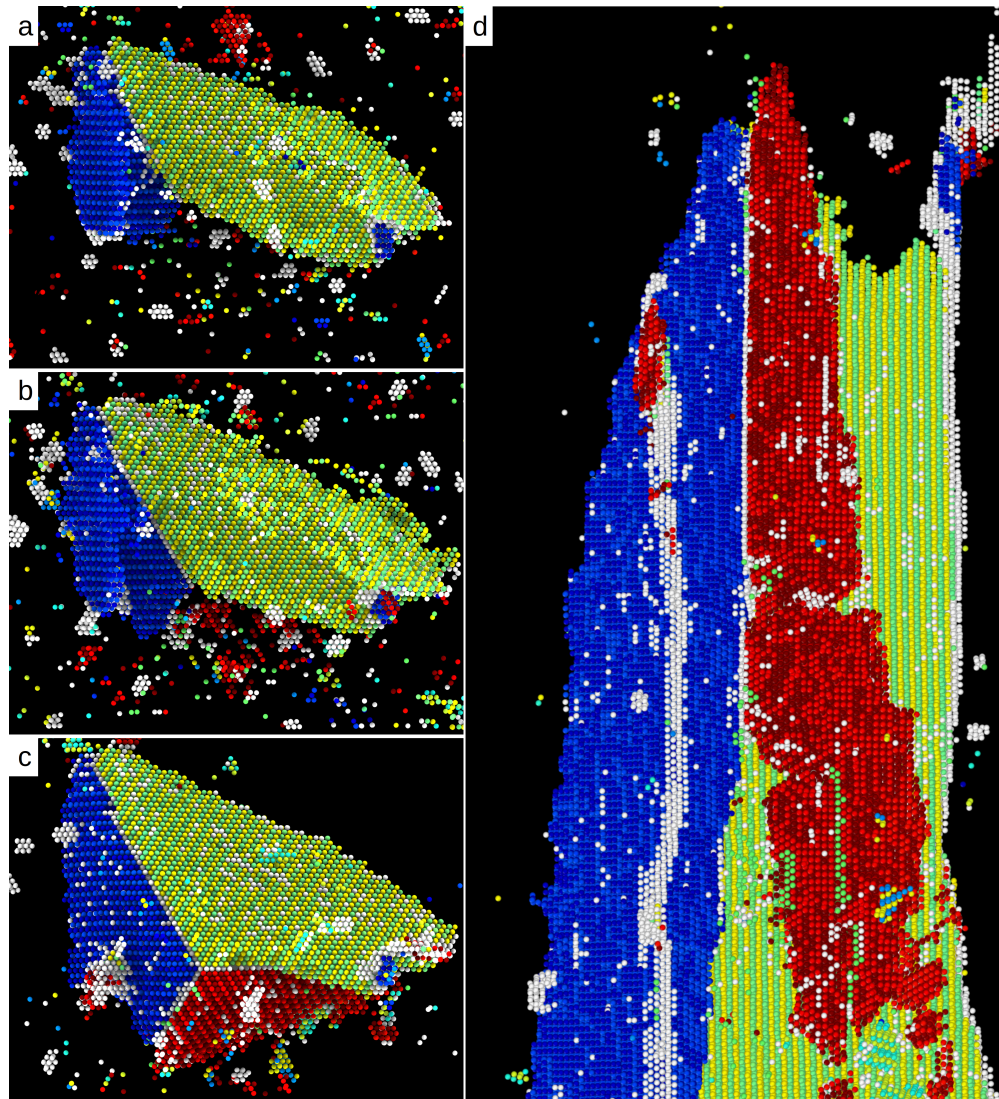
Figure 7.9: Sections showing growth of two grains of the α-phase from β (atoms removed) which nucleated on dislocation lines in the supercell which is 737 Å in length. In each grain the $[0\ 0\ 0\ 1]_\alpha$ direction is indicated by a line. Atom coloring is by PTM as described previously. (a) The two original grains growing from the dislocations with $\frac{2\pi}{3}$ orientation difference have intersected and formed a type 1 grain boundary. (b) The nucleation of a third grain with complementary orientation is induced by the strain around the original two grains. (c) The three grains have grown until they form a tent structure with three type 1 grain boundaries. (d) Side view of the same structure, without sectioning. This clearly shows the tent shape of the colony.

Chapter 8:

Summary and future work

Thank you for the sustained attention required to make it this far. In this final chapter, I will briefly summarize the preceding chapters, and then discuss any future work stemming from each that seems interesting.

8.1 $\langle$a$\rangle$-Type Screw Dislocation Core Structures at 0 K and 0 Applied Stress

In Chapter 3 I demonstrated the dependence of the calculated ground state dislocation core structure on a number of parameters and suggest minimum settings for converged calculations. I considered two arrangements of periodic arrays of dislocations and demonstrate the high sensitivity of the final core structures to choice of valence electronic states and k-point mesh density. Within each arrangement I also used two initial positions of the dislocations, one between basal planes and the other within basal planes. (Meta)stable pyramidal and prismatic dislocation core structures exist within both the DFT and MEAM potentials, and the relaxed structure resulting from my anisotropic elasticity theory solution depends only on the initial dislocation positions. The pyramidal configuration results when the dislocations are initially between basal planes, and the prismatic configuration results when the dislocations are initially within basal planes. In DFT I found the ground-state core structure to be purely pyramidal. I found it necessary to include the semi-core $3p$ electrons as valence states in order to converge the ground state dislocation core configuration in either arrangement, and in particular to correctly find the difference in energy between this state and other metastable core configurations. I demonstrated that a k-point mesh of at least $1 \times 1 \times 15$ is necessary to converge the dislocation core structure for a supercell one Burgers vector deep. Use of higher k-point densities or inclusion of additional semi-core electronic states as valence electrons results in the same core structure. MEAM calculations were undertaken to demonstrated the effects of supercell size, and these findings suggest that my DFT calculations were performed with large enough supercells to avoid significant finite-size effects associated with stress gradients near the dislocation core structures. With the MEAM potential considered in this work, I found the ground state core configuration to be spread predominantly on the prismatic plane, in contrast with the DFT results. For both methods the energy differences between core structures were found to be small (on the order of tens of meV), which suggests that at practical temperatures there will be occupation of more than one core structure configuration.

For this chapter I can recommend little future work. I have already undertaken the tasks stemming from the conclusions of this section that occurred to me. However, as DFT methodology as well as computational power continues to improve, it may be worth

revisiting the calculations performed here. In particular it would be useful to redo the DFT calculations with larger supercells, as this may improve the accuracy of the relative core structures energies calculated. Further, it might be worthwhile to perform these calculations with updated exchange-correlation functional such as meta-GGA as these become practical for calculations of this size.

8.2 Non-Schmid Effects on ⟨a⟩-Type Screw Dislocation Core Structures

Chapter 4 continued Chapter 3 with DFT and MEAM calculations of ⟨a⟩-type screw dislocation core structures in hcp titanium under a series of applied stresses with zero critical resolved shear stress were performed to investigate the origin of non-Schmid law slip behavior in α-titanium alloys. It was found that compression applied on the $[1\bar{1}00]$ direction perpendicular to the Burgers vector leads to more compact pyramidally-oriented cores, while tension applied on the same axis causes an extension of these cores along the prismatic plane. Nudged elastic band calculations of the barrier to slip of the dislocations on the prismatic plane showed that extension along this plane leads to reduced slip barriers. This suggests that non-Schmid stresses alter the critical resolved shear stress by inducing changes in the equilibrium core structure. These results corroborate earlier conjecture that the non-Schmid slip behavior of ⟨a⟩-type screw dislocations in α-titanium alloys was due to non-planar core structure.

One potentially worthwhile extension of this work would be to calculate the slip barrier for planes other than the prismatic plane. If an applied non-Schmid stress creates a more pyramidal core structure, then this work suggests that pyramidal slip would likely be easier under those conditions. This could perhaps be used to calculate the change in the probability (or rate) of cross-slip. Since cross-slip is important particularly in hcp alloys like the α-titanium alloys that have a tendency towards planar slip and the resulting loss of toughness (discussed in Chapter 6), understanding how core structure can effect cross-slip could be important for building more complete models of plasticity in these alloys. Studying non-Schmid effects is important for understanding the plastic asymmetry in materials, but it may also lead to alloy design or processing ideas (such as pre-stressing parts perhaps) that would improve performance.

8.3 Finite Temperature Analysis of ⟨a⟩-Type Screw Dislocation Core Structures

In Chapter 5 I described the development of a new parameter υ based on elasticity theory that can be used for dislocation core identification and classification. I applied this new parameter to the study of ⟨a⟩-type screw dislocation core structures in titanium, examining the dependence of the core orientation on temperature and applied non-Schmid stresses. It was found that increasing the temperature leads to a larger variation in the core orientations. It was also found that applied stress on the $[1\bar{1}00]$ axis normal to the dislocation line direction leads to a transition from the prismatic core structure to the pyramidal core structure in the MEAM potential. Further, this transition appears to shift to lower pres-

sure when the temperature is increased, which implies that pyramidal cores are favored at higher temperature, suggesting that they are higher-entropy structures than the prismatic cores. Simulations with applied shear stress oriented for prismatic slip were also performed, and it was demonstrated that temperature/non-Schmid stress conditions that permit easier access to the prismatic core orientation lead to higher strain rates for the same applied shear stress. The locking-unlocking mechanism[8] was observed quite clearly in a simulation with large compression on the $[1\bar{1}00]$ axis, as slip only occurred during the brief periods in which the dislocation core structure was oriented prismatically. It was shown that increasing the temperature allows for more unlocking of the cores when the non-Schmid stress causes the pyramidal orientation to be preferred, but if the prismatic core orientation is preferred then increasing the temperature can actually reduce the strain rate by promoting occupation of pyramidal core structures.

I believe that the work detailed in this chapter presents the greatest opportunity for future work. The new parameter υ can be applied to many scenarios other than the titanium dislocation core structures discussed here, and if this case is any indication then this type of study may lead to many interesting new ideas. One example for another study along these lines includes looking at other hcp metals which have different preferred slip systems and contrasting slip between these. Another idea is the application to bcc metals that was actually the genesis of this method. This would require only developing a parametrization of a fit υ that yields the information of interest (i.e. core size rather than orientation). One might be interested in computing the equilibrium core size of dislocations in these metals as a component of computational alloy design, because compact cores slip more readily. Another example is designing gum-metal like alloys by looking for compositions or temperature/pressure conditions that lead to extremely large dislocation cores like those observed in gum-metal.

Besides the parameter developed here, some of the ideas generated by this study also deserve further examination. For example the concept of dislocation core structure free energy certainly requires more thought. For metals like titanium in which there are competing core structures of similar potential energy, the role of the entropy of these states may be very important to plasticity at elevated temperatures. While I have observed implicit effects arising from differences in core free energy here, I have not developed a theory of dislocation core entropy. Perhaps it would be feasible to calculate a small number of dislocation core parameters at zero temperature – potential energy of states, energy of boundaries between states, entropy of states (likely involving configurational and vibrational components) – and use these as inputs to a model that would correctly predict the occupation of core structures over a range of temperatures. The results of such a model could then be compared to MD simulations similar to those presented in this dissertation. I would be surprised if this is not a project assigned to an incoming Chrzan group student...

8.4 $\langle a \rangle$-Type Screw Dislocation – Interstitial Interactions

Based on computational studies of oxygen solute effects on deformation in titanium as well as experimental evidence contributed by collaborators in Andrew Minor's group, I introduced a novel interstitial shuffling mechanism (ISM) explaining how dilute concentrations

of interstitial impurities can promote increased planarity of dislocation slip, and reduce work hardening. The ISM provides a framework to understand the dramatic effects on toughness of Ti alloys associated with very small variations in interstitial content. These insights open new avenues for the design of titanium alloys with increased tolerance to variations in interstitial impurity content, with significant implications for more widespread use of this high strength to weight material. More generally, the ISM identified here may apply to other alloy systems containing interstitial solutes that interact strongly with the relevant dislocations. The basic requirements for the ISM to be operative are only two interstitial sites differing in dislocation pinning strength, and the possibility for dislocations to shuffle interstitials from one of these sites to the other. Due to the significant deleterious effects of planar slip on toughness, it is valuable to identify mechanisms underlying this phenomenon and associated pathways to control them. In this context, the ISM identified here contributes generally to the fundamental knowledge of possible origins for embrittlement due to interstitial solutes, and provides a framework for the design of improved Ti alloys in particular.

One key feature lacking from this work is a broader model that incorporates the effects on cross-slip, temperature, composition, interstitial strengthening, and the ISM all together to present a complete picture of the strength, toughness, and degree of planar slip that can be expected for an alloy at operating conditions of interest. Such a model would be of great interest for both alloy design and component design, and would also serve as a useful point of reference to provide further confirmation of the ISM.

Another ongoing extension of this project is the examination of the behavior of carbon and nitrogen interstitial solutes in titanium. These solutes are the two next-most-important interstitials in titanium alloys after oxygen, and are commonly thought of as behaving equivalently to oxygen. However, preliminary investigation by myself and Jack Peterson suggests that both of these present lesser opportunities for slip-plane softening than oxygen, because they are larger atoms that do not fit as well in the intra-basal sites, leading to greater energy differences between the octahedral and hexahedral sites for these interstitials, and a greater interference with slip when sitting in the intra-basal site. However, full development of the equivalent ISM pictures for these two is still ongoing work.

Finally for future work on this topic, the purpose of developing a model such as ISM is to take advantage of it for alloy design. Now that this mechanism has been uncovered and its importance to plasticity demonstrated, further work is required to exploit this knowledge to develop tougher, more ductile, and more solute-resistant alloys. I have begun this work by approximating the effects of substitutional alloying by adjusting the number of electrons in DFT calculation, and this work suggests that slightly increasing the electron density of the alloy should reduce the difference in energy between the octahedral and hexahedral sites, and could also effect the energy barrier between these sites. This indicates that alloying with substitutional elements such as vanadium or niobium could improve alloy performance with respect to ISM, though considerably more work along these lines will be required to demonstrate this. One crucial issue will be the limited solubility of these elements in titanium, perhaps requiring the addition of multiple species with complementary effects. Another issue is that these elements are known stabilizers of the β phase of titanium, which potentially restricts processing routes if nucleation of β and segregation of these solutes to β grains is to be avoided.

8.5 β to α Transition at Screw Dislocations

In Chapter 7 heterogeneous nucleation of the α to β phase transition at $\langle 1\,1\,1 \rangle_\beta$-type screw dislocations in pure titanium was examined through a combination of elasticity theory and molecular dynamics simulation using a modified embedded atom method potential. These screw dislocations act as heterogeneous nucleation sites and increase the α phase growth rate, but also restrict the orientation of the α nuclei to certain directions along which the strain field of the dislocation aligns with the strain required to complete the Burgers transformation path. Simulations and elasticity theory predict the same three α phase variants along the same preferential directions for α nucleus growth in the early stages of transformation. Previous elasticity theory calculations indicate that this growth does not result in the elastically preferred habit plane for the α nucleus. Molecular dynamics simulations on many-layer supercells show that large α plates will change their growth direction towards the predicted habit plane, but this rotation is resisted by the line tension of the dislocation until the α precipitate detaches from the dislocation. These findings extend those previously deduced from phase-field simulations by enabling the time scales associated with nucleation to be explored directly.

Within the scope of this topic, a valuable future project would be the extension of these ideas to edge dislocations in the β phase. Phase-field modeling by other authors suggest that these are even more potent nucleation sites than the screw dislocations, and therefore a full understanding of α phase nucleation and variant selection will include these. Further extensions to planar defects such as twins, stacking faults, and grain boundaries in the β phase might also yield interesting results.

This work, as well as elements of Chapters 5 and 6, suggest another generally-important factor to consider in all future atomistic simulations of dislocations: the length of the supercell along the dislocation line direction. In Chapter 7 this is found to be a crucial factor to find the correct habit plane for α grains during growth. In Chapter 5 I found that unfortunately my simulations were shorter than the correlation length of dislocation core structures along the line direction, which appears to influence the transition between states based on preliminary modeling. In Chapter 6 it was commented that using insufficiently long supercells can lead to unrealistic dislocation behavior, specifically that cross-slip around interstitials appears to be much too easy in short supercells. All of these observations suggest that the length of dislocation lines in simulations have been too short to represent properly the dislocations in most atomistic simulations to date. However, the expense of simulations and post-processing has been the factor dictating these sizes. Future research with greater resource availability should make careful consideration of dislocation line lengths when possible. Allowances for transitions between core structures and non-straight dislocations (i.e. with screw, mixed, and edge components) will be crucial for atomistic simulations that will correctly predict plasticity in metals for practical applications.

References

[1] P. Hohenberg and W. Kohn. Inhomogeneous Electron Gas. *Physical Review*, 136(3B):B864–B871, 1964.

[2] Raffaele Guido Della Valle and Hans C. Andersen. Molecular dynamics simulation of silica liquid and glass. *The Journal of Chemical Physics*, 97(4):2682–2689, 1992.

[3] Erik Bitzek, Pekka Koskinen, Franz Gähler, Michael Moseler, and Peter Gumbsch. Structural relaxation made simple. *Phys. Rev. Lett.*, 97:170201, 2006.

[4] A.A. Griffith. VI. The phenomena of rupture and flow in solids. *Philosophical Transactions of the Royal Society of London A: Mathematical, Physical and Engineering Sciences*, 221(582-593):163–198, 1921.

[5] J.M. Burgers and W.G. Burgers. Chapter 6 - Dislocations in Crystal Lattices. In Frederick R. Eirich, editor, *Rheology*, pages 141 – 199. Academic Press, 1956.

[6] V. Vítek, R. C. Perrin, and D. K. Bowen. The core structure of 1/2⟨111⟩ screw dislocations in b.c.c. crystals. *Philosophical Magazine*, 21(173):1049–1073, 1970.

[7] Gang Lu, Nicholas Kioussis, Vasily V. Bulatov, and Efthimios Kaxiras. Generalized-stacking-fault energy surface and dislocation properties of aluminum. *Phys. Rev. B*, 62:3099–3108, 2000.

[8] S. Farenc, D. Caillard, and A. Couret. An in situ study of prismatic glide in α titanium at low temperatures. *Acta Metallurgica Et Materialia*, 41(9):2701–2709, 1993.

[9] Emmanuel Clouet. Screw dislocation in zirconium: An ab initio study. *Physical Review B*, 86(14):144104, 2012.

[10] Emmanuel Clouet, Daniel Caillard, Nermine Chaari, Fabien Onimus, and David Rodney. Dislocation locking versus easy glide in titanium and zirconium. *Nature Materials*, 14(9):931–936, 2015.

[11] T. Tsuru and D. C. Chrzan. Effect of solute atoms on dislocation motion in Mg: An electronic structure perspective. *Scientific Reports*, 5:8793, 2015.

[12] J.P. Hirth and J. Lothe. *Theory of Dislocations*. Krieger Publishing Company, 1982.

[13] R Peierls. The size of a dislocation. *Proceedings of the Physical Society*, 52:34–37, 1940.

[14] F R N Nabarro. Dislocations in a Simple Cubic Lattice. *Proc. Phys. Soc.*, 59(1940):256, 1947.

[15] U.S. Geological Survey. Mineral Commodities Summaries. *Mineral Commodity Summaries*, page 202, 2016.

[16] Hans Conrad. Effect of interstitial solutes on the strength and ductility of titanium. *Progress in Materials Science*, 26(2-4):123–403, 1981.

[17] Maarten de Jong, J. Kacher, M. H. F. Sluiter, L. Qi, D. L. Olmsted, A. van de Walle, J. W. Morris, A. M. Minor, and M. Asta. Electronic origins of anomalous twin boundary energies in hexagonal close packed transition metals. *Phys. Rev. Lett.*, 115:065501, 2015.

[18] Peter Mahler Larsen, SØren Schmidt, and Jakob SchiØtz. Robust structural identification via polyhedral template matching. *Modelling and Simulation in Materials Science and Engineering*, 24(5), 2016.

[19] Einstein A. Zur elektrodynamik bewegter körper. *Annalen der Physik*, 322(10):891–921.

[20] Einstein A. Über einen die erzeugung und verwandlung des lichtes betreffenden heuristischen gesichtspunkt. *Annalen der Physik*, 322(6):132–148.

[21] R. P. Feynman. Space-time approach to quantum electrodynamics. *Phys. Rev.*, 76:769–789, 1949.

[22] Born M. and Oppenheimer R. Zur quantentheorie der molekeln. *Annalen der Physik*, 389(20):457–484.

[23] W. Kohn and L. J. Sham. Self-consistent equations including exchange and correlation effects. *Phys. Rev.*, 140:A1133–A1138, 1965.

[24] Richard M. Martin. *Electronic Structure: Basic Theory and Practical Methods*. Cambridge University Press, 2004.

[25] John P. Perdew, Kieron Burke, and Matthias Ernzerhof. Generalized Gradient Approximation Made Simple. *Physical Review Letters*, 77(18):3865–3868, 1996.

[26] P. E. Blöchl. Projector augmented-wave method. *Physical Review B*, 50(24):17953–17979, 1994.

[27] Hendrik J. Monkhorst and James D. Pack. "Special points for Brillouin-zone integrations"—a reply. *Physical Review B*, 16(4):1748–1749, 1977.

[28] M. Methfessel and A. T. Paxton. High-precision sampling for Brillouin-zone integration in metals. *Physical Review B*, 40(6):3616–3621, 1989.

[29] P. Güttinger. Das verhalten von atomen im magnetischen drehfeld. *Zeitschrift für Physik*, 73(3):169–184, 1932.

[30] Wolfgang Pauli. *General principles of quantum mechanics*. Springer-Verlag, Berlin New York, 1980.

[31] D. Andrae and H. Hellmann. *Hans Hellmann: Einführung in die Quantenchemie: Mit biografischen Notizen von Hans Hellmann jr.* Springer Berlin Heidelberg, 2015.

[32] R. P. Feynman. Forces in molecules. *Phys. Rev.*, 56:340–343, 1939.

[33] O. H. Nielsen and Richard M. Martin. First-principles calculation of stress. *Phys. Rev. Lett.*, 50:697–700, 1983.

[34] O. H. Nielsen and Richard M. Martin. Quantum-mechanical theory of stress and force. *Phys. Rev. B*, 32:3780–3791, 1985.

[35] G. Kresse and J. Furthmüller. Efficiency of ab-initio total energy calculations for metals and semiconductors using a plane-wave basis set. *Computational Materials Science*, 6(1):15–50, 1996.

[36] G. Kresse and J. Furthmüller. Efficient iterative schemes for ab initio total-energy calculations using a plane-wave basis set. *Physical Review B*, 54(16):11169–11186, 1996.

[37] M. J. Stott and E. Zaremba. Quasiatoms: An approach to atoms in nonuniform electronic systems. *Physical Review B*, 22(4):1564–1583, 1980.

[38] Murray S. Daw and M. I. Baskes. Semiempirical, Quantum Mechanical Calculation of Hydrogen Embrittlement in Metals. 50(17):285–288, 1983.

[39] Murray s. Daw and M. I. Baskes. Embedded-atom method: Derivation and application to impurities, surfaces, and other defects in metals. *Physical Review B*, 29(12):6443–6453, 1984.

[40] M. I. Baskes, J. S. Nelson, and A. F. Wright. Semiempirical modified embedded-atom potentials for silicon and germanium. *Phys. Rev. B*, 40:6085–6100, 1989.

[41] M. I. Baskes. Modified embedded-atom potentials for cubic materials and impurities. *Physical Review B*, 46(5):2727–2742, 1992.

[42] Steve Plimpton. Fast Parallel Algorithms for Short-Range Molecular Dynamics. *Journal of Computational Physics*, 117(1):1–19, 1995.

[43] Jonathan R Shewchuk. An introduction to the conjugate gradient method without the agonizing pain. Technical report, Pittsburgh, PA, USA, 1994.

[44] Loup Verlet. Computer "experiments" on classical fluids. i. thermodynamical properties of lennard-jones molecules. *Phys. Rev.*, 159:98–103, 1967.

[45] M. Tuckerman, B. J. Berne, and G. J. Martyna. Reversible multiple time scale molecular dynamics. *The Journal of Chemical Physics*, 97(3):1990–2001, 1992.

[46] Tamar Schlick. *Molecular modeling and simulation : an interdisciplinary guide.* Springer Science+Business Media, LLC, New York, 2010.

[47] M. Parrinello and A. Rahman. Polymorphic transitions in single crystals: A new molecular dynamics method. *Journal of Applied Physics*, 52(12):7182–7190, 1981.

[48] William G. Hoover, Denis J. Evans, Richard B. Hickman, Anthony J. C. Ladd, William T. Ashurst, and Bill Moran. Lennard-jones triple-point bulk and shear viscosities. green-kubo theory, hamiltonian mechanics, and nonequilibrium molecular dynamics. *Phys. Rev. A*, 22:1690–1697, 1980.

[49] Hans C. Andersen. Molecular dynamics simulations at constant pressure and/or temperature. *The Journal of Chemical Physics*, 72(4):2384–2393, 1980.

[50] Greg Mills and Hannes Jónsson. Quantum and thermal effects in H2 dissociative adsorption: Evaluation of free energy barriers in multidimensional quantum systems. *Physical Review Letters*, 72(7):1124–1127, 1994.

[51] Graeme Henkelman and Hannes Jónsson. Improved tangent estimate in the nudged elastic band method for finding minimum energy paths and saddle points. *The Journal of Chemical Physics*, 113(22):9978, 2000.

[52] Graeme Henkelman, Blas P. Uberuaga, and Hannes Jónsson. Climbing image nudged elastic band method for finding saddle points and minimum energy paths. *Journal of Chemical Physics*, 113(22):9901–9904, 2000.

[53] Max Poschmann, Mark Asta, and D C Chrzan. Convergence of calculated dislocation core structures in hexagonal close packed titanium. *Modelling and Simulation in Materials Science and Engineering*, 26(1):014003, 2018.

[54] M. Ghazisaeidi and D. R. Trinkle. Core structure of a screw dislocation in Ti from density functional theory and classical potentials. *Acta Materialia*, 60(3):1287–1292, 2012.

[55] Liang Qi, Tomohito Tsuru, Mark Asta, and D C Chrzan. Interactions between Oxygen Interstitial and a -Type Screw Dislocations in α -Titanium. pages 1–29, 2015.

[56] Nathalie Tarrat, Magali Benoit, Daniel Caillard, Lisa Ventelon, Nicolas Combe, and Joseph Morillo. Screw dislocation in hcp Ti : DFT dislocation excess energies and metastable core structures. *Modelling and Simulation in Materials Science and Engineering*, 22(5):055016, 2014.

[57] S.I. Rao, A. Venkateswaran, and M.D. Letherwood. Molecular statics and molecular dynamics simulations of the critical stress for motion of a/3 screw dislocations in α-Ti at low temperatures using a modified embedded atom method potential. *Acta Materialia*, 61(6):1904–1912, 2013.

[58] Qian Yu, Liang Qi, Tomohito Tsuru, Rachel Traylor, David Rugg, J. W. Morris, M. Asta, D. C. Chrzan, and A. M. Minor. Origin of dramatic oxygen solute strengthening effect in titanium. *Science*, 347(6222):635–639, 2015.

[59] C Woodward and S I Rao. Flexible Ab initio boundary conditions: simulating isolated dislocations in bcc Mo and Ta. *Physical review letters*, 88(21):216402, 2002.

[60] Yi Zhao and Gang Lu. QM/MM study of dislocation—hydrogen/helium interactions in α-Fe. *Modelling and Simulation in Materials Science and Engineering*, 19(6):065004, 2011.

[61] G. Kresse and D. Joubert. From ultrasoft pseudopotentials to the projector augmented-wave method. *Physical Review B*, 59(3):1758–1775, 1999.

[62] Murray S. Daw. Elasticity effects in electronic structure calculations with periodic boundary conditions. *Computational Materials Science*, 38(2):293–297, 2006.

[63] Niklas Lehto and Sven Öberg. Effects of Dislocation Interactions: Application to the Period-Doubled Core of the 90° Partial in Silicon. *Physical Review Letters*, 80(25):5568–5571, 1998.

[64] C. S. Hartley and Y. Mishin. Characterization and visualization of the lattice misfit associated with dislocation cores. *Acta Materialia*, 53(5):1313–1321, 2005.

[65] R. G. Hennig, T. J. Lenosky, D. R. Trinkle, S. P. Rudin, and J. W. Wilkins. Classical potential describes martensitic phase transformations between the α, β, and ω titanium phases. *Physical Review B*, 78(5):054121, 2008.

[66] Gang Lu, Nicholas Kioussis, Vasily V. Bulatov, and Efthimios Kaxiras. Generalized-stacking-fault energy surface and dislocation properties of aluminum. *Physical Review B*, 62(5):3099–3108, 2000.

[67] S Rao, C. Hernandez, J. P. Simmons, T. A. Parthasarathy, and C. Woodward. Green's function boundary conditions in two-dimensional and three-dimensional atomistic simulations of dislocations. *Philosophical Magazine A*, 77(1):231–256, 1998.

[68] Xu Zhang, Qing Peng, and Gang Lu. Self-consistent embedding quantum mechanics/molecular mechanics method with applications to metals. *Physical Review B - Condensed Matter and Materials Physics*, 82(13), 2010.

[69] R. Chait. The strength differential of steel and Ti alloys as influenced by test temperature and microstructure. *Scripta Metallurgica*, 7(4):351–354, 1973.

[70] T. Sakai and M. E. Fine. Failure of Schmid's law in TiAl alloys for prismatic slip. *Scripta Metallurgica*, 8(5):541–544, 1974.

[71] S. Naka, A. Lasalmonie, P. Costa, and L. P. Kubin. The low-temperature plastic deformation of α-titanium and the core structure of a-type screw dislocations. *Philosophical Magazine A*, 57(5):717–740, 1988.

[72] T. Neeraj †, M.F. Savage, J. Tatalovich, L. Kovarik, R.W. Hayes, and M.J. Mills. Observation of tension–compression asymmetry in α and titanium alloys. *Philosophical Magazine*, 85(2-3):279–295, jan 2005.

[73] Michael E. Nixon, Oana Cazacu, and Ricardo A. Lebensohn. Anisotropic response of high-purity α-titanium: Experimental characterization and constitutive modeling. *International Journal of Plasticity*, 26(4):516 – 532, 2010.

[74] B. Barkia, V. Doquet, J.P. Couzinié, I. Guillot, and E. Héripré. In situ monitoring of the deformation mechanisms in titanium with different oxygen contents. *Materials Science and Engineering: A*, 636:91–102, 2015.

[75] Maarten De Jong, Ian Winter, D. C. Chrzan, and Mark Asta. Ideal strength and ductility in metals from second- and third-order elastic constants. *Physical Review B*, 96(1), 2017.

[76] V VITEK. THEORY OF CORE STRUCTURES OF DISLOCATIONS IN BODY-CENTERED CUBIC METALS. *CRYSTAL LATTICE DEFECTS*, 5(1):1–34, 1974.

[77] Ernst Ising. Beitrag zur theorie des ferromagnetismus. *Zeitschrift für Physik*, 31(1):253–258, Feb 1925.

[78] Lars Onsager. Crystal statistics. i. a two-dimensional model with an order-disorder transition. *Phys. Rev.*, 65:117–149, Feb 1944.

[79] S.P. Beckman and D.C. Chrzan. Structures of glide-set 90° partial dislocation cores in diamond cubic semiconductors. *Physica B: Condensed Matter*, 340-342:990 – 995, 2003. Proceedings of the 22nd International Conference on Defects in Semiconductors.

[80] D. C. Chrzan, M. P. Sherburne, Y. Hanlumyuang, T. Li, and J. W. Morris. Spreading of dislocation cores in elastically anisotropic body-centered-cubic materials: The case of gum metal. *Phys. Rev. B*, 82:184202, Nov 2010.

[81] C. A. Sawyer, J. W. Morris, and D. C. Chrzan. Dislocation core radii near elastic stability limits. *Phys. Rev. B*, 87:134106, Apr 2013.

[82] I. S. Winter, M. Poschmann, T. Tsuru, and D. C. Chrzan. Dislocations near elastic instability in high-pressure body-centered-cubic magnesium. *Phys. Rev. B*, 95:064107, Feb 2017.

[83] D.C. Wallace. *Thermodynamics of Crystals*. Dover books on physics. Dover Publications, 1998.

[84] Alexander Stukowski and Karsten Albe. Extracting dislocations and non-dislocation crystal defects from atomistic simulation data. *Modelling and Simulation in Materials Science and Engineering*, 18(8):085001, dec 2010.

[85] Alexander Stukowski. Visualization and analysis of atomistic simulation data with OVITO–the Open Visualization Tool. *Modelling and Simulation in Materials Science and Engineering*, 18(1):015012, 2010.

[86] Caetano R. Miranda, R. W. Nunes, and A. Antonelli. Temperature effects on dislocation core energies in silicon and germanium. *Phys. Rev. B*, 67:235201, Jun 2003.

[87] Yingzhao Jiang, Rui Wang, and Shaofeng Wang. The temperature-dependent dislocation properties of aluminum from the improved peierls–nabarro model and first-principles. *Philosophical Magazine*, 96(27):2829–2852, 2016.

[88] Zhigang Zak Fang, Scott Middlemas, Jun Guo, and Peng Fan. A new, energy-efficient chemical pathway for extracting ti metal from ti minerals. *Journal of the American Chemical Society*, 135(49):18248–18251, 2013.

[89] A. D. Hartman, S. J. Gerdemann, and J. S. Hansen. Producing lower-cost titanium for automotive applications. *JOM*, 50(9):16–19, 1998.

[90] GZ Chen, DJ Fray, and TW Farthing. Direct electrochemical reduction of titanium dioxide to titanium in molten calcium chloride. *Nature*, 407(6802):361–4, 2000.

[91] P.A. Russo and S.R. Seagle. Properties of titanium for industrial applications with emphasis on ti-3al-2. 5v. *Am. Soc. Test. Mater., Spec. Tech. Publ.; (United States)*, STP-830, 9 1982.

[92] Gerd Lütjering and James C. Williams. *Titanium*. Engineering Materials, Processes. Springer Berlin Heidelberg, Berlin, Heidelberg, 2007.

[93] Wei Cai, Vasily V. VV Bulatob, Jinpeng Chang, Ju Li, and Sidney Yip. Periodic image effects in dislocation modelling. *Philosophical Magazine*, 83(December 2012):37–41, 2003.

[94] Rodrigo Freitas, Mark Asta, and Vasily V. Bulatov. Quantum effects on dislocation motion from ring-polymer molecular dynamics.

[95] Pandu Wisesa, Kyle A. McGill, and Tim Mueller. Efficient generation of generalized Monkhorst-Pack grids through the use of informatics. *Physical Review B*, 93(15):155109, 2016.

[96] Pinchao Zhang and Dallas R. Trinkle. A modified embedded atom method potential for interstitial oxygen in titanium. *Computational Materials Science*, 124:204–210, 2016.

[97] J. C. Williams, a. W. Sommer, and P. P. Tung. The influence of oxygen concentration on the internal stress and dislocation arrangements in α titanium. *Metallurgical Transactions*, 3(11):2979–2984, 1972.

[98] D.J. Truax and C.J. McMahon. Plastic behavior of titanium-aluminum alloys. *Materials Science and Engineering*, 13(2):125–139, feb 1974.

[99] G. T. Gray, G. Luetjering, and J. C. Williams. The influence of oxygen on the structure, fracture, and fatigue crack propagation behavior of Ti-8.6 Wt Pct Al. *Metallurgical Transactions A*, 21(1):95–105, 1990.

[100] M. C. Brandes, M. J. Mills, and J. C. Williams. The Influence of Slip Character on the Creep and Fatigue Fracture of an α Ti-Al Alloy. *Metallurgical and Materials Transactions A*, 41(13):3463–3472, dec 2010.

[101] J.C. Scully and D.T. Powell. The stress corrosion cracking mechanism of α-titanium alloys at room temperature. *Corrosion Science*, 10(10):719 – 733, 1970.

[102] T. Neeraj, D. H. Hou, G. S. Daehn, and M. J. Mills. Phenomenological and microstructural analysis of room temperature creep in titanium alloys. *Acta Materialia*, 48(6):1225–1238, 2000.

[103] M.J. Blackburn and J.C. Williams. Metallurgical aspects of the stress corrosion cracking of titanium alloys. *pp 620-37 of Proceedings of Conference on Fundamental Aspects of Stress Corrosion Cracking, Columbus, Ohio, September 11–15, 1967. Staehle, R. W. Forty, A. J. van Rooyen, D. (eds.). Houston, Te*, 1969.

[104] A Van de Walle and M Asta. First-principles investigation of perfect and diffuse antiphase boundaries in HCP based Ti-Al alloys. *Metallurgical and Materials Transactions a-Physical Metallurgy and Materials Science*, 33(3):735–741, 2002.

[105] David L. Olmsted, Maarten de Jong, Paul Erhart, and Mark Asta. Private communication.

[106] T. Neeraj and M.J Mills. Short-range order (SRO) and its effect on the primary creep behavior of a Ti–6wt.%Al alloy. *Materials Science and Engineering: A*, 319-321:415–419, dec 2001.

[107] Richard G Hennig, Dallas R Trinkle, Johann Bouchet, Srivilliputhur G Srinivasan, Robert C Albers, and John W Wilkins. Impurities block the α to ω martensitic transformation in titanium. *Nature Materials*, 4(2):129–133, feb 2005.

[108] M.A. Bhatia, X. Zhang, M. Azarnoush, G. Lu, and K.N. Solanki. Effects of oxygen on prismatic faults in α-Ti: a combined quantum mechanics/molecular mechanics study. *Scripta Materialia*, 98(January):32–35, 2015.

[109] M. Ghazisaeidi and D.R. Trinkle. Interaction of oxygen interstitials with lattice faults in Ti. *Acta Materialia*, 76:82–86, 2014.

[110] P. Kwasniak, H. Garbacz, and K. J. Kurzydlowski. Solid solution strengthening of hexagonal titanium alloys: Restoring forces and stacking faults calculated from first principles. *Acta Materialia*, 102:304–314, 2016.

[111] Y. Hanlumyuang, P.A. Gordon, T. Neeraj, and D.C. Chrzan. Interactions between carbon solutes and dislocations in bcc iron. *Acta Materialia*, 58(16):5481–5490, sep 2010.

[112] A. N. Stroh. Dislocations and cracks in anisotropic elasticity. *The Philosophical Magazine: A Journal of Theoretical Experimental and Applied Physics*, 3(30):625–646, 1958.

[113] Erin Hayward, Chaitanya Deo, Blas P. Uberuaga, and Carlos N. Tome. The interaction of a screw dislocation with point defects in bcc iron. *Philosophical Magazine*, 92(22):2759–2778, 2012.

[114] Siems R. Mechanical interactions of point defects. *physica status solidi (b)*, 30(2):645–658, 1968.

[115] Céline Varvenne and Emmanuel Clouet. Elastic dipoles of point defects from atomistic simulations. *Phys. Rev. B*, 96:224103, Dec 2017.

[116] P. C. Gehlen, J. P. Hirth, R. G. Hoagland, and M. F. Kanninen. A new representation of the strain field associated with the cube-edge dislocation in a model of a α-iron. *Journal of Applied Physics*, 43(10):3921–3933, 1972.

[117] Emmanuel Clouet, Lisa Ventelon, and F. Willaime. Dislocation core energies and core fields from first principles. *Phys. Rev. Lett.*, 102:055502, Feb 2009.

[118] Emmanuel Clouet, Lisa Ventelon, and F. Willaime. Dislocation core field.II. Screw dislocation in iron. *Physical Review B - Condensed Matter and Materials Physics*, 84(22):1–12, 2011.

[119] J.D. Eshelby, W.T. Read, and W. Shockley. Anisotropic elasticity with applications to dislocation theory. *Acta Metallurgica*, 1(3):251 – 259, 1953.

[120] A Stukowski and A Arsenlis. On the elastic–plastic decomposition of crystal deformation at the atomic scale. *Modelling and Simulation in Materials Science and Engineering*, 20(3):035012, 2012.

[121] A. J. E. Foreman and M. J. Makin. Dislocation movement through random arrays of obstacles. *Philosophical Magazine*, 14(131):911–924, oct 1966.

[122] Alexander Stukowski. Structure identification methods for atomistic simulations of crystalline materials. *Modelling and Simulation in Materials Science and Engineering*, 20(4):045021, jun 2012.

[123] Kenton Hanson and J. W. Morris. Limiting configuration in dislocation glide through a random array of point obstacles. *Journal of Applied Physics*, 46(3):983–990, 1975.

[124] J. Y Lim, C. J McMahon, D. P Pope, and J. C Williams. The Effect of Oxygen on the Structur and Mechanical Behaviour of Aged Ti-8 Wt Pct Al. *Metallurgical Review*, 7A(January):139–144, 1976.

[125] Henry H. Wu and Dallas R. Trinkle. Direct diffusion through interpenetrating networks: Oxygen in titanium. *Physical Review Letters*, 107(4):1–4, 2011.

[126] Henry H. Wu and Dallas R. Trinkle. Solute effect on oxygen diffusion in α -titanium. *Journal of Applied Physics*, 113(22):223504, 2013.

[127] W G Burgers. On the Process of Transition of the Cubic-Body-Centered Modification into the Hexagonal-Close-Packed Modification of Zirconium. 1933.

[128] N. Gey, M. Humbert, M.J. Philippe, and Y. Combres. Investigation of the α- and β-texture evolution of hot rolled Ti-64 products. *Materials Science and Engineering: A*, 219(1-2):80–88, 1996.

[129] N Gey, M Humbert, M.J. Philippe, and Y Combres. Modeling the transformation texture of Ti-64 sheets after rolling in the β-field. *Materials Science and Engineering: A*, 230(1-2):68–74, 1997.

[130] Z.S Zhu, J.L Gu, R.Y Liu, N.P Chen, and M.G Yan. Variant selection and its effect on phase transformation textures in cold rolled titanium sheet. *Materials Science and Engineering: A*, 280(1):199–203, 2000.

[131] N. Gey and M. Humbert. Characterization of the variant selection occurring during the $\alpha \rightarrow \beta \rightarrow \alpha$ phase transformations of a cold rolled titanium sheet. *Acta Materialia*, 50(2):277–287, 2002.

[132] S.C. Wang, M. Aindow, and M.J. Starink. Effect of self-accommodation on α/α boundary populations in pure titanium. *Acta Materialia*, 51(9):2485–2503, 2003.

[133] D. Bhattacharyya, G.B Viswanathan, Robb Denkenberger, D. Furrer, and Hamish L. Fraser. The role of crystallographic and geometrical relationships between α and β phases in an α/β titanium alloy. *Acta Materialia*, 51(16):4679–4691, 2003.

[134] I. Lonardelli, N. Gey, H.-R. Wenk, M. Humbert, S.C. Vogel, and L. Lutterotti. In situ observation of texture evolution during $\alpha \rightarrow \beta$ and $\beta \rightarrow \alpha$ phase transformations in titanium alloys investigated by neutron diffraction. *Acta Materialia*, 55(17):5718–5727, 2007.

[135] S.M.C. van Bohemen, A. Kamp, R.H. Petrov, L.A.I. Kestens, and J. Sietsma. Nucleation and variant selection of secondary α plates in a β Ti alloy. *Acta Materialia*, 56(20):5907–5914, 2008.

[136] M.R. Daymond, R.A. Holt, S. Cai, P. Mosbrucker, and S.C. Vogel. Texture inheritance and variant selection through an hcp–bcc–hcp phase transformation. *Acta Materialia*, 58(11):4053–4066, 2010.

[137] Shanoob Balachandran, Ankush Kashiwar, Abhik Choudhury, Dipankar Banerjee, Rongpei Shi, and Yunzhi Wang. On variant distribution and coarsening behavior of the α phase in a metastable β titanium alloy. *Acta Materialia*, 106:374–387, 2016.

[138] D. Qiu, R. Shi, D. Zhang, W. Lu, and Y. Wang. Variant selection by dislocations during α precipitation in α/β titanium alloys. *Acta Materialia*, 88:218–231, 2015.

[139] D. Qiu, R. Shi, P. Zhao, D. Zhang, W. Lu, and Y. Wang. Effect of low-angle grain boundaries on morphology and variant selection of grain boundary allotriomorphs and Widmanstätten side-plates. *Acta Materialia*, 112:347–360, 2016.

[140] R. Shi, N. Zhou, S.R. Niezgoda, and Y. Wang. Microstructure and transformation texture evolution during α precipitation in polycrystalline α/β titanium alloys – A simulation study. *Acta Materialia*, 94:224–243, 2015.

[141] Rodrigo Freitas, Mark Asta, and Maurice De Koning. Nonequilibrium free-energy calculation of solids using LAMMPS. *Computational Materials Science*, 112:333–341, 2016.

[142] Daan Frenkel and Anthony J. C. Ladd. New Monte Carlo method to compute the free energy of arbitrary solids. Application to the fcc and hcp phases of hard spheres. *The Journal of Chemical Physics*, 81(7):3188–3193, 1984.

[143] M. de Koning, A. Antonelli, and S. Yip. Optimized Free-Energy Evaluation Using a Single Reversible-Scaling Simulation Maurice. *Physical Review Letters*, 83(November):3973, 1999.

[144] Maurice de Koning, Alex Antonelli, and Sidney Yip. Single-simulation determination of phase boundaries: A dynamic Clausius–Clapeyron integration method. *The Journal of Chemical Physics*, 115(24):11025–11035, 2001.

[145] W. Petry, A. Heiming, J. Trampenau, M. Alba, C. Herzig, H. R. Schober, and G. Vogl. Phonon dispersion of the bcc phase of group-iv metals. i. bcc titanium. *Phys. Rev. B*, 43:10933–10947, 1991.

[146] Seungwu Han, Luis A. Zepeda-Ruiz, Graeme J. Ackland, Roberto Car, and David J. Srolovitz. Interatomic potential for vanadium suitable for radiation damage simulations. *Journal of Applied Physics*, 93(6):3328–3335, 2003.

[147] J. W. Cahn. Nucleation on dislocations. *Acta Metallurgica*, 5(3):169 – 172, 1957.

[148] G. Thomas and J. Nutting. The mechanism of phase transformations in metals. *Institute of Metals, London*, pages 57–66, 1956.

[149] A. Kelly and R. B. Nicholson. Precipitation hardening. *Progress in Materials Science*, 10:151 – 391, 1963.

[150] DJ Bacon, DM Barnett, and Ronald Otto Scattergood. Anisotropic continuum theory of lattice defects. *Progress in Materials Science*, 23:51–262, 1980.

[151] D. C. Chrzan, M. P. Sherburne, Y. Hanlumyuang, T. Li, and J. W. Morris. Spreading of dislocation cores in elastically anisotropic body-centered-cubic materials: The case of gum metal. *Phys. Rev. B*, 82:184202, 2010.

[152] T Furuhara, S Takagi, H Watanabe, and T Maki. Crystallography of grain boundary α precipitates in a β titanium alloy. *Metallurgical and Materials Transactions A*, 27(6):1635–1646, 1996.

[153] Melvin Avrami. Kinetics of phase change. i general theory. *The Journal of Chemical Physics*, 7(12):1103–1112, 1939.

[154] Melvin Avrami. Kinetics of phase change. ii transformation-time relations for random distribution of nuclei. *The Journal of Chemical Physics*, 8(2):212–224, 1940.

[155] Melvin Avrami. Granulation, phase change, and microstructure kinetics of phase change. iii. *The Journal of Chemical Physics*, 9(2):177–184, 1941.

[156] M. P. Kashchenko and V. G. Chashchina. Crystal dynamics of the BCC-HCP martensitic transformation: I. Controlling wave process. *The Physics of Metals and Metallography*, 105(6):537–543, 2008.

[157] J. W. Morris, Y. Hanlumyuang, M. Sherburne, E. Withey, D. C. Chrzan, S. Kuramoto, Y. Hayashi, and M. Hara. Anomalous transformation-induced deformation in ⟨1 1 0⟩ textured Gum Metal. *Acta Materialia*, 58(9):3271–3280, 2010.